Ecole Polytechnique Federale de Lausanne
School of Life Sciences

Master Thesis in Bioengineering

All-Optical Electrophysiology in Zebrafish

Amanda B. Klaeger
amanda.klaeger@alumni.epfl.ch

COHEN LAB
Harvard Department of Chemistry and Chemical Biology

EPFL Advisor: Prof. Dr. Carl C. H. Petersen
Harvard Advisor: Prof. Dr. Adam E. Cohen
Supervisor: Dr. Urs L. Böhm

Boston, August 2019

Acknowledgements

I would like to thank Professor Adam Cohen for radiating so much contagious enthusiasm toward science, for his valuable scientific insights and guidance that have shaped my path and for encouraging me to follow an empowering 'just do it' approach that has helped me tackle unfamiliar problems. I would also like to thank Adam for always making time for discussions despite his extremely busy schedule.

Furthermore, I would like to thank Professor Carl Petersen for creating an extremely well-structured MOOC on Neuroscience that sparked my interest in this field and for agreeing to supervise this project from afar.

I am deeply grateful to Dr. Urs Böhm for being a wonderful mentor in all respects. I would like to thank him for his scientific vision as well as for his advice and guidance that have enabled my scientific growth. I would also like to thank Urs for his infinite patience and kindness in countless situations – I still find it incredible that he did not so much as flinch after I broke the umpteenth glass needle during my first attempt at injections. I would like to thank him for many inspiring discussions and for always being available to help. Finally, I would like to thank him for trusting me to use his light sheet setup and various other equipment.

I would like to thank Dr. Hanan Dahche for sharing her vast knowledge about many different wetlab and molecular biology related topics and for helping me debug numerous cloning problems. Even more so, I would like to thank her for her positive spirit, her beautiful smile and for filling so many lunches with sunshine and laughter. I must also thank her for feeding me with her delicious home-made food on so many occasions where my blood sugar levels were critically low.

I would like to thank Dr. Shane Nichols for many great conversations at the setup that made long imaging sessions more fun. I would like to thank him for always being there to help with all kinds of hardware related problems. I would also like to thank him for encouraging me to get my dose of exercise.

Furthermore, I would like to thank Maggie Kenar for being an amazing human being and taking care of me on so many occasions!

I would like to thank the Bertarelli Foundation and Family for providing the funds that have enabled me to undertake this journey. I would also like to thank Professors John Assad and David Corey for their scientific advice and insights during Bertarelli lunches as well as Gail Townsend for taking care of all the administrative aspects of my stay. Many thanks also go to Pascale Zbinden and Dietrich Reinhard, who have made my trip possible on the EPFL side.

I would like to thank my family for their ceaseless support and Irina for always being there for me. Finally, I would like to thank Dorian for his love and trust and for coming to Boston to support me in person.

Summary

Voltage imaging is a powerful tool that can be used to record neuronal membrane potential dynamics with spike-time resolution and that allows the visualization of subthreshold membrane potential oscillations. Yet, on its own, it does not have the power to perturb neuronal activity - a highly desirable feature for studying the fundamental mechanisms of brain function and circuitry. Voltage imaging can be combined with optogenetics to yield all-optical electrophysiology. Zebrafish, a well-established model organism in neuroscience research, is a particularly attractive system for all-optical experiments, since its larvae are transparent. Although voltage imaging has been previously implemented in zebrafish, this study is the first to combine voltage imaging with optogenetics to establish all-optical electrophysiology in this organism. We expressed a voltage indicator and a channelrhodopsin – a light-gated ion channel - in neurons, and tested three different excitation techniques to actuate the channelrhodopsin: one-photon (1P) blue light sheet excitation, 1P blue widefield excitation and two-photon (2P) scanning excitation using infrared light. We found that 1P excitation was more efficient at activating neurons. Having established the system, we explored the application of all-optical electrophysiology to mapping functional connectivity in the zebrafish spinal cord, by optically stimulating a single cell and simultaneously recording voltage dynamics in many postsynaptic candidate cells to screen for synaptic connectivity. Secondly, we investigated whether an all-optical approach could be used to determine the ratio of excitatory and inhibitory synaptic inputs (E/I-Balance) to a neuron. Finally, we developed a transgenic zebrafish line expressing both a voltage indicator and a channelrhodopsin. This tool obviates the need for cumbersome expression methods, like zebrafish embryo injections for transient expression, yielding a robust system for investigation of fundamental questions in neuroscience.

Keywords: Neuroscience, All-Optical Electrophysiology, Voltage Imaging, Optogenetics, Zebrafish, Spinal Cord, Functional Connectivity, E/I-Balance, Transgenic Zebrafish.

Contents

List of Figures

Acronyms

1P one photon (excitation). 2, 8, 29, 31, 38–41, 43, 45, 57, 58, 62

2P Two-photon. 2, 8, 10, 29, 30, 38–41, 43, 57–59, 62

ACR anion channelrhodopsin. 15, 16

AP action potential. 9, 10, 14, 17, 22, 38–42, 46–48, 51, 53, 58–60

Arch Archaerhodopsin, a proton pump. 13, 15

ASAP accelerated sensor of action potentials. 10, 12

ChR2 Channelrhodopsin-2, a light-gated cation channel. 15

Ci Ciona intestinalis, an ascidian (sea squirt). 10, 11

CiD circumferential descending (glutamatergic zebrafish interneurons). 19, 20, 34

CoChR Chloromonas oogama channelrhodopsin. 5, 8, 17, 27, 29, 31, 32, 37, 38, 42–45, 54–56, 58–62

CPG central pattern generator. 19

cpGFP circularly permuted green fluorescent protein. 10

CRACM channelrhodopsin-2-assisted circuit mapping. 22

DC duty cycle. 31, 38, 40, 44, 48, 49

DNA deoxyribonucleic acid. 53

E/I excitation and inhibition. 2, 8, 9, 26, 30, 34, 57, 60–62

eFRET electrochromic Förster/fluorescence energy resonance transfer. 13

EM electron microscopy. 21

FlicR1 fluorescent indicator for voltage imgaging red. 11

fMRI functional magnetic resonance imaging. 22

FRET Förster/fluorescence energy resonance transfer. 10–13

GEVI genetically encoded voltage indicator. 5, 9–13, 18, 23

GFP green fluorescent protein. 10, 22, 29, 38

GPR green-absorbing proteorhodopsin. 13

GRASP GFP (green fluorescent protein) reconstitution across synaptic partners. 22

HEK human embryonic kidney (cells). 13

iChlOC improved chloride-conducting channelrhodopsin. 15

LM light microscopy. 21, 22

MCoD multipolar commissural descending (glutamatergic zebrafish interneurons). 19, 20, 34

mRNA messenger ribonucleic acid. 28, 31–33, 53, 61

OMR optomotor response. 48, 49

PCR polymerase chain reaction. 28, 54

PMT photomultiplier tube. 29, 30

PROPS proteorhodopsin optical proton sensor. 13

QuasAr 'quality superior to Arch' (Archaerhodopsin). 13

RFP red fluorescent protein. 11

ROI region of interest. 30, 34, 35, 45, 46

SEM standard error of the mean. 51

SEP super ecliptic pHluorin, a pH sensor. 10, 12

SFO step function opsin. 16

SNR signal to noise ratio. 9

SPIM single/selective plane illumination microscopy. 18

ssEM serial-section electron microscopy. 21

UAS upstream activating sequence. 21, 27

VARNAM (meaning 'color' in Sanskrit) voltage-activated red neuronal activity monitor. 13

VeMe ventral medial (glutamatergic zebrafish interneurons). 20, 31, 48, 51, 60, 61

VNR ventral nerve root. 5, 31, 48, 49

VSD voltage-sensing domain. 10–12

VSFP voltage-sensing fluorescent protein. 5, 10, 11

1 Introduction

1.1 Motivation and Overview

In order to shed more light on how the central nervous system performs computations, it is important to gain a deeper understanding of the underlying neural circuits. Ideally, one would study the brain and spinal cord in awake animals during behavior, with a technique that allows to probe and record from many neurons in parallel. Optical methods provide relatively non-invasive approaches for both actuating neurons and sensing neural activity [1], [2], [3]. Voltage imaging enables the recording of membrane potential with single spike-time resolution and also captures subthreshold oscillations [4], [5], [6], [7]. These are important advantages compared to other common methods to monitor neural activity such as calcium imaging, which is not fast enough to capture action potentials, cannot report membrane hyperpolarization and depends on calcium transients and is thus inherently a more indirect way of assessing neuronal activity than voltage imaging [3]. The latter also has advantages over conventional patch-clamp measurements since it enables the simultaneous imaging of many neurons at once, thereby offering higher throughput, and it is non-invasive [8]. Voltage imaging alone does not allow to perturb neural circuits, which would be helpful to identify their function; however it can be combined with optogenetics [9], [10], [11] to enable all-optical electrophysiology [1], [5], [6]. Excitatory [12] and inhibitory [13] optogenetic tools can be used to selectively activate or silence certain neurons.

Voltage imaging has been demonstrated previously in zebrafish [4], [14], however it has not yet been combined with optogenetics in this model system. In this study, we aim to combine voltage imaging and optogenetics to establish all-optical electrophysiology for the first time in zebrafish. Here, we first illuminate the path that led past a variety of different constructs and finally ended in a combination of a voltage indicator (zArchon [4]) and a channelrhodopsin (CoChR, [12]) that reliably enabled the simultaneous perturbation and read-out of zebrafish membrane potential. After ensuring the functionality of our all-optical electrophysiology system, we proceeded to testing different ways of stimulating the channelrhodopsin which included one photon (1P) light sheet excitation, 1P widefield excitation and two photon (2P) scanning excitation. 1P excitation was simpler to implement and exhibited a better stimulation efficiency; however 2P excitation eliminates out-of-focus illumination, which is crucial for precise single-cell excitation, and enables deeper penetration depths owing to the longer wavelengths used. Therefore, some efforts were directed to testing 2P excitation of the channelrhodopsin. While not being able to achieve equal stimulation efficiency using 2P excitation compared to 1P stimulation, we demonstrate here that single-cell targeting with 2P stimulation can be accomplished.

After establishing all-optical electrophysiology in zebrafish and showing that the channelrhodopsin can be stimulated in a number of different ways, we sought to apply this new tool to explore two interesting questions in the neuroscience field. Firstly, we directed our attention to the task of mapping functional connectivity in the zebrafish spinal cord. We stimulated a single cell and simultaneously recorded from many possible postsynaptic candidate cells with the aim of finding a postsynaptic response and thus identifying functional connectivity between the stimulated cell and downstream cells. While we were not able to unambiguously identify a functional connection between two neurons, this study provides a helpful illustration of how such a task could potentially be achieved. Secondly, we focused on the problem of identifying the relationship between excitatory and inhibitory synaptic inputs to a single cell and determining the balance of excitation and inhibition (E/I-balance). Here, we strive to implement an all-optical method to quantify E/I-balance. While this project is still work in progress and concrete results regarding E/I-balance have not yet been obtained, we demonstrate a valuable first step toward applying all-optical electrophysiology to this type of question.

Finally, we establish a transgenic zebrafish line that expresses the constructs necessary for all-optical electrophysiology. The experiments in this study were conducted using injection of constructs into zebrafish embryos to achieve transient expression. A transgenic line can exhibit higher expres-

sion levels and provides ease of manipulation by eliminating the need to cross zebrafish and inject embryos on a weekly basis. This transgenic line has the potential to benefit many future generations of all-optical electrophysiology experiments and to provide fundamental new insights into different neuroscience topics.

In the following introduction, an overview of voltage imaging, optogenetics, connectivity mapping and E/I-balance is provided.

1.2 Voltage Imaging

Membrane voltage plays a key signaling role in cells, especially neurons. While voltage sensitive dyes are one approach to measuring membrane potential [15], they are difficult to target to specific cells, are often phototoxic and are not suitable for long term imaging studies [3].The following will focus on genetically encoded voltage indicators (GEVIs) that have the advantage of allowing for genetic targeting to a specific subset of cells. GEVIs translate a change in voltage into a change in fluorescence. First some desirable properties are introduced, then different types of GEVIs are presented and finally some limitations are discussed.

1.2.1 Desirable Characteristics

In order to capture single action potentials, the GEVI needs to have fast response kinetics (on the order of a millisecond), exhibit a sufficiently large change in signal upon a change in membrane potential (sensitivity, $\frac{\Delta F}{F}$) and have a good baseline fluorescence (brightness). This last point is important since imaging rates need to be high to capture action potentials, so exposure time is low [4], [8], [1]. The change in fluorescence upon a change in membrane voltage should also be as linear as possible. Membrane trafficking is another important factor since badly trafficked proteins, which are not localized on the cell membrane and do not contribute to fluorescence changes in response to membrane voltage change, will contribute to the background signal. Furthermore, the GEVI must be non-toxic to cells, express well in mammalian cells and exhibit low photobleaching [3], [16]. High photostability is important since one would like to image for extended periods of time without drastic decreases in signal. Finally, the GEVI should ideally be compatible with optogenetics, meaning it needs to be spectrally orthogonal to the excitation wavelength used for the optogenetic actuator/inhibitor [2].

1.2.2 Advantages and Limitations

Voltage imaging with GEVIs has several advantages over other techniques that measure neural activity. Compared to calcium imaging, voltage imaging has much better temporal resolution and thus the advantage of being able to report single spikes and also has the capacity to measure subthreshold voltage oscillations [7]. Calcium imaging quantifies neuronal activity by reporting calcium transients associated with the firing of APs. The drawbacks of this are the fact that the relationship of calcium signal changes to AP firing can vary from cell to cell and the fact that baseline spiking activity is necessary to visualize inhibition using calcium imaging. Compared to classical patch-clamp electrophysiology, voltage imaging with GEVIs has the advantage of being able to report from many more cells in parallel and thus offers higher throughput. Targeting the GEVI to specific cell types as well as using spatial light patterns to image from a subset of cells provides a lot of flexibility unique to this tool. Furthermore, non-invasive imaging is possible with all-optical electrophysiology as well as carrying out long term imaging studies of the same cells. Electrode recordings also enable chronic studies, however they do not offer good spatial resolution or information about subthreshold dynamics.

Current GEVIs still suffer from low SNR, photobleaching and spectral incompatibility with optogenetic tools. Although many efforts have been made to solve these problems, a GEVI that combines

all the desirable characteristics listed in section 1.2.1 in great quality is still to be engineered. Parallel efforts on the instrumentation side are producing novel imaging techniques that are helping to avoid light scattering, achieving targeted stimulation and enabling faster readouts.

1.2.3 Types of Voltage Indicators

Flash was the first reported GEVI and was described in 1997. It reported changes in membrane potential with changes in fluorescence in Xenopus oocytes [17]. Since then, much effort has gone into improving GEVIs and many different types have been produced. GEVIs can be classified into two main groups: GEVIs based on voltage-sensing domains (VSD) found in phosphatases or ion channels (Fig. 1 and Fig. 2 a-c), and GEVIs based on microbial rhodopsins (Fig. 2 d-e) [3]. VSDs occur naturally and function in gating ion channels or controlling the activity of phosphatases. They usually consist of four transmembrane domains where the last one (S4) contains multiple residues of positive charge that are sensitive to voltage. When the membrane is hyperpolarized, S4 moves toward the intracellular side, whereas it moves toward the extracellular side during depolarization [16]. VSD-based GEVIs couple a fluorescent protein to a VSD. Changes in voltage cause conformational changes in the VSD which in turn alter the signal of the fluorescent protein. The second class of GEVIs uses microbial rhodopsins to sense voltage. These are light-sensitive ion pumps that were engineered to lose their pumping function and operate as voltage indicators.

1.2.3.1 VSD-Based GEVIs

The first GEVI Flash was created by fusing the potassium channel Shaker to a modified green fluorescent protein (GFP) [17]. However, localization to the plasma membrane in mammalian cells was very poor and kinetics were slow [8]. The first set of GEVIs that expressed well in mammalian cells was the VSFP2 (voltage sensing fluorescent protein) group described in 2007, which used the VSD of a phosphatase derived from the sea squirt *Ciona intestinalis* (Ci) [18], [3]. The VSFP are based on fluorescence resonance energy transfer (FRET) whereby the FRET efficiency between the two attached fluorescent proteins is modulated by voltage (Fig. 1). While membrane-trafficking was better in this group of GEVIs compared to previous ones, sensitivity and kinetics were still insufficient to detect action potentials (APs) [2].

A great increase in sensitivity came with the discovery of ArcLight that comprised the Ci-VSD fused to a mutated version of the pH-sensor super ecliptic pHluorin (SEP) [19]. The kinetics of ArcLight were too slow to resolve APs, however three mutations led to Bongwoori that had a rapid reponse and could resolve APs at 60 Hz [8] (Fig. 2a). Depolarization is reported by a reduction in fluorescence of the SEP in both ArcLight and Bongwoori.

In 2014, a novel series of GEVIs named "accelerated sensor of action potentials" (ASAP) was introduced. The indicator was created by inserting a circularly permuted GFP (cpGFP) into the extra-cellular loop of a chicken derived phosphatase VSD [20]. This means that the voltage reporting moiety is outside of the cell, as opposed to the previously discussed indicators (Fig. 2b). ASAP1 reports voltage with a decrease in fluorescence upon membrane depolarization. The kinetics of ASAP1 were on the order of 2 ms and so it was able to report APs at a frequency of up to 200 Hz [20]. Since ASAP1, further engineering efforts have produced ASAP2f, which has improved fluorescence [21] and ASAP2s, which has better sensitivity but slower kinetics [22]. Both of these new variants are theoretically compatible with two-photon (2P) imaging, however results were mediocre. Thus ASAP3 was engineered to have better 2P imaging compatibility, while retaining fast kinetics and good sensitivity (51 % $\frac{\Delta F}{F}$ per 100 mV) [23].

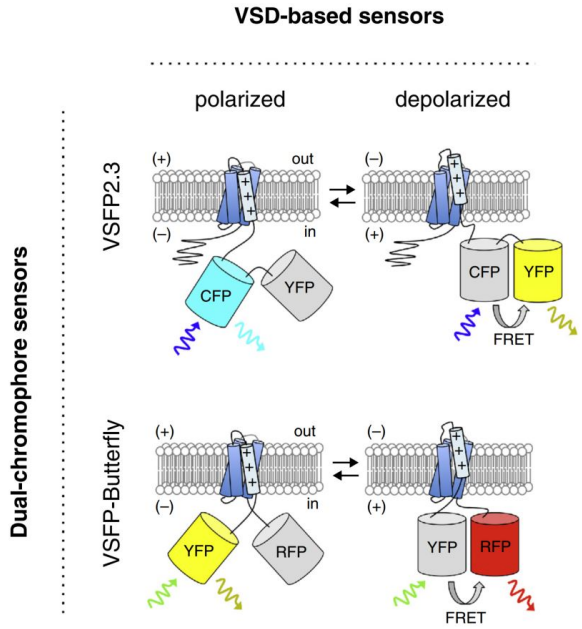

Figure 1: VSFP family of GEVIs. A change in voltage modulates the FRET efficiency between two fluorescent proteins. VSD: voltage-sensing domain, CFP: cyan fluorescent protein, YFP: yellow fluorescent protein, RFP: red fluorescent protein. Figure adapted from [16].

FlicR1 (fluorescent indicator for voltage imaging red) is another VSD-based GEVI using a fusion of the Ci-VSD to a circularly permuted RFP (Fig. 2c) and reports membrane depolarization with an increase in fluorescence [24]. It is very desirable to have red-shifted GEVIs since they are compatible with blue-excited optogenetic tools. They also require longer excitation wavelengths, which cause less photodamage, less background autofluorescence and enable imaging at greater depths. However, FlicR1 was not sufficiently spectrally separated to blue-excited actuation tools; thus excitation and imaging patterns still had to be spatially separated to prevent cross-talk [24].

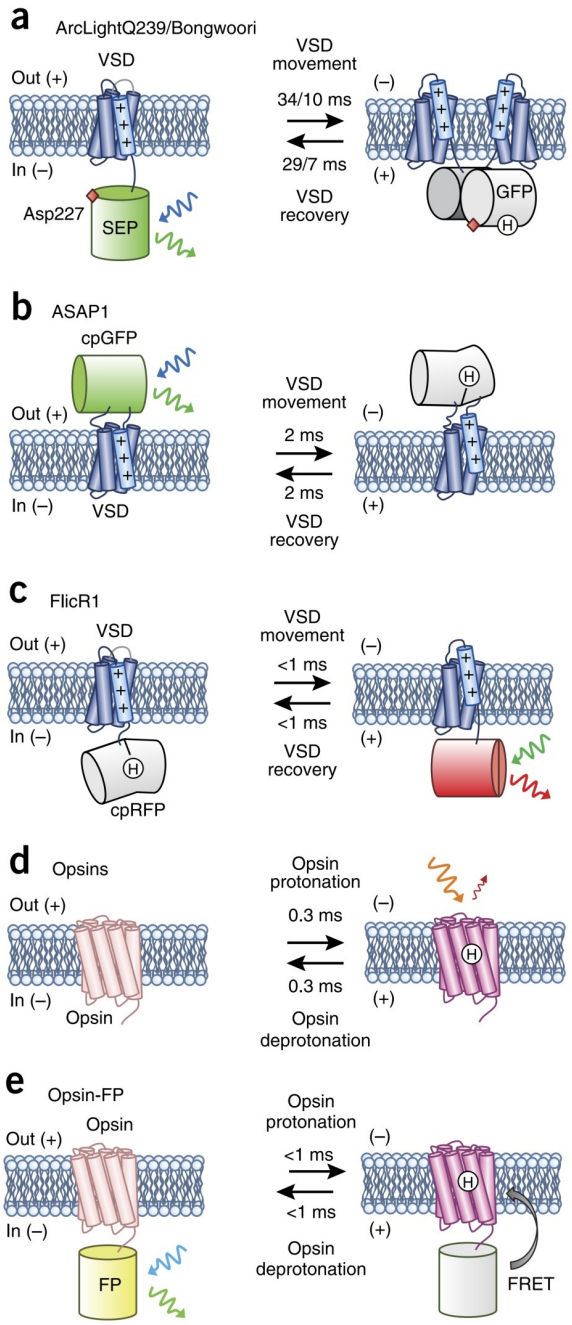

Figure 2: Overview of different types of GEVIs. Numbers above/below the arrows represent on- and off-time constants respectively. **(a)** ArcLight and Bongwoori exhibit decreased fluorescence upon membrane depolarization. The process is not fully understood but assumed to involve dimerization as a function of increasing voltage. This causes protonation of SEP and a decrease in fluorescence. **(b)** For the ASAP family, the voltage reporting fluorescent protein is outside of the cell and reports voltage increases with a decrease in fluorescence, like ArcLight. Displacement of the VSD likely causes protonation of the chromophore, which reduces fluorescence. **(c)** FlicR1 is a red-shifted GEVI and is excited with green light, rather than blue as for the first two. FlicR1 fluorescence increases upon depolarization. **(d)** Most opsins are excited with red light and increase fluorescence upon membrane depolarization. This is because increasing voltages cause protonation of the Schiff base which links the chromophore to the protein core. Signals are usually very dim. **(e)** Brightness can be improved by coupling opsins with fluorescent proteins. With increasing voltages, more energy is transferred to the opsin via FRET rather than emitted as fluorescence, so the overall fluorescence decreases with voltage. Figure adapted from [3].

1.2.3.2 Microbial Rhodopsin-Based GEVIs

The second class of GEVIs is based on microbial rhodopsins that were initially only associated with optogenetic tools. However, it was found that rhodopsins are weakly fluorescent and that their fluorescence is modulated by membrane potential changes. In 2011, Kralj et al. mutated the

light-modulated proton pump GPR (green-absorbing proteorhodopsin) to yield the voltage indicator PROPS (proteorhodopsin optical proton sensor) [25]. Microbial rhodopsins contain a retinal chromophore linked to the protein via a Schiff base [16]. The opsin emits fluorescence in the infared range when the Schiff base is protonated. Protonation of the Schiff base is voltage-sensitive, thereby linking membrane potential to opsin fluorescence [8] (Fig. 2d). The first microbial opsin PROPS had bad trafficking properties to the plasma membrane in eukaryotic cells, thus was not compatible with voltage imaging in mammalian cells [16].

Archaerhodopsin (Arch) turned out to have better membrane trafficking properties [26] and functioned as a GEVI that was able to capture individual action potentials [27]. However, the original Arch still had a pumping function and generated a photocurrent that biased membrane voltage. A mutated version of Arch lacked the pumping function, but also had considerably slower kinetics [27].

Arch was evolved to produce a non-pumping opsin-based GEVI QuasAr ('quality superior to Arch') with improved kinetics and membrane trafficking [1]. Two different QuasArs were produced. QuasAr1 was faster and brighter, but also photobleached faster while QuasAr2 had better sensitivity ($\frac{\Delta F}{F}$) and thus better SNR. The time constant following a step-response was around 0.05 ms for QuasAr1 and around 0.3 ms for QuasAr2 at 34°C [1]. QuasAr1 is still the fastest GEVI to date.

QuasAr2 was the template for a round of directed evolution which produced Archon1 and Archon2. These two voltage indicators also differed in their brightness and sensitivity with Archon1 having much higher $\frac{\Delta F}{F}$ (81% compared to only 20% for Archon2 in HEK cells, which was lower than the template) and Archon2 having better brightness [4]. Only Archon1 was used in subsequent studies.

A drawback of voltage imaging with microbial rhodopsin based GEVIs is their dimness. Their fluorescence is around 30-80 times lower than GFP and illumination intensities of 200-1000 $\frac{W}{cm^2}$ are needed so thermal damage becomes a non-negligible issue [8]. To approach this problem, microbial rhodopsins have been coupled to fluorescent proteins to make use of the electrochromic FRET (eFRET) effect. Changes in voltage cause changes in the opsin absorption spectrum which modify the extent of non-radiative quenching of the attached fluorescent protein [8] (Fig. 2e). Ace-mNeon is an example of a successful eFRET GEVI with very good brightness and kinetics [28]. However the excitation wavelength of 506 nm makes it incompatible with optogenetic tools that also require excitation wavelengths in the blue range.

A new red-shifted eFRET-based GEVI, VARNAM (voltage-activated red neuronal activity monitor) is spectrally compatible with blue-shifted optogenetic tools and thus can be used for all-optical electrophysiology. It consists of a combination of the opsin Ace and the bright red fluorescent protein mRuby3 and was validated *in vivo* in Drosophila [29].

Abdelfattah et al. have recently come up with a novel FRET-based GEVI design "Voltron" that fuses a rhodopsin domain to a HaloTag self-labeling domain, which can then associate with a chemical rhodamine dye ('JaneliaFluor') [30]. Upon membrane depolarization, FRET of the dye to the rhodopsin domain increases and thus dye fluorescence decreases. Voltron seems like a promising and versatile tool since a variety of different synthetic dyes can be coupled to the rhodopsin domain. Red-shifted dyes could be compatible with optogenetics, although the most red-shifted dyes unfortunately have the lowest $\frac{\Delta F}{F}$, since there is a trade-off between spectral overlap for FRET and red-shift (see Fig. S43 in [30]).

1.2.4 Choice of GEVI For This Study

The GEVI that was used in this study is zArchon1, the zebrafish codon-optimized version of Archon1 published by Piatkevich et al. in 2018 [4]. zArchon1 had the best combination of properties (sensitivity, brightness, kinetics, membrane localization, compatibility with optogenetic tools) at the time this project was started. Archon1's kinetics were tested by Piatkevich et al. in cultured mouse neurons (Fig. 3a), which revealed that the fast on-time constant (explaining 88% of the temporal on-dynamics) was 0.61 ms and the fast off-time constant (also accounting for 88%) was 1.1 ms.

Furthermore, Archon1 exhibits a relatively linear change in fluorescence upon change in voltage (Fig. 3b,c), minimal AP-broadening at a $\frac{\Delta F}{F}$ of 30% (Fig. 3d) as well as a reasonably low amount of photobleaching (Fig. 3e,f) [4].

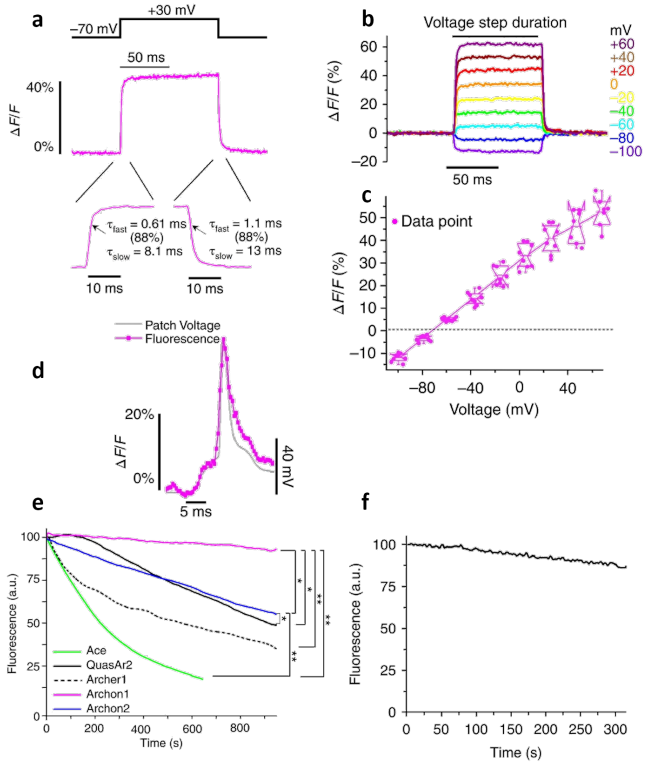

Figure 3: Characteristics of Archon1. **(a)** Kinetics of Archon1 tested in cultured mouse neurons in voltage-clamp after stepping the voltage up 100 mV. The cell was illuminated at 637 nm and 800 $\frac{mW}{mm^2}$. A bi-exponential decay was fit to the data ($\frac{\Delta F}{F} = Ae^{-t/\tau_{fast}} + Be^{-t/\tau_{slow}}$). The percentages indicate $A/(A+B)$. **(b)** Archon1 fluorescence during voltage clamp at different holding potentials. Illumination conditions were the same as in **a**. The data was normalized so that at a voltage of -70 mV, $\frac{\Delta F}{F} = 0$. **(c)** Aggregated data from 8 neurons indicating that the fluorescence change is very linear with voltage for the data in **b**. **(d)** Recording of an AP with Archon1 (magenta) and patch-clamp (grey) simultaneously. Archon1 follows the voltage well and AP-broadening is minimal. $\frac{\Delta F}{F}$ for the AP was 30%. **(e)** Photobleaching was determined in cultured mouse neurons during 900 s under the same illumination conditions as in **a** for Archon1 and adapted for the other sensors to have the same SNR at $t = 0$. Archon1 fluorescence was 95% after 900 s. **(f)** Photobleaching of zArchon1 (zebrafish codon-optimized version of Archon1) determined in a zebrafish larvae during 300 s. Fluorescence was 84% of the initial fluorescence after 300 s. Figure adapted from [4].

1.3 Optogenetics

Initial efforts towards optical control of cellular activity [31], [32], [33] along with the characterization of channelrhodopsin - a light-gated ion channel found in the green alga *Chlamydomonas reinhardtii* [34] - and its subsequent expression in neurons with the aim of controlling neural activity at the single spike level [9] were the onset of the era of optogenetics. Action potentials and membrane depolarization are key components of the electrical communication between neurons. Both can be elicited optically with light-gated ion channels that will let positive ions enter the neuron upon light stimulation. In algae, channelrhodopsins are involved in phototaxis by regulating the function of flagella to enable movement toward light [35].

The term "optogenetics" was first used in 2006 by Deisseroth et al. [36] to refer to the concept of using optical methods to manipulate specific genetically targeted subsets of cells, in particular neurons. This is an extremely powerful tool since it enables the precise and non-invasive control of neural activity in defined populations of cells and with this it opens the possibility to probe specific brain circuits, to study the relationship between neural activation and behavior and many more research avenues. A couple of key insights that optogenetics has made possible are listed by

Josselyn on the occasion of the 2018 Gairdner Award going to Peter Hegemann, Ed Boyden and Karl Deisseroth for their work on optogenetics [37].

The following will briefly present the structure and function of channelrhodopsin and give a non-comprehensive list of examples of optogenetic tools.

1.3.1 Structure of Channelrhodopsin

Microbial opsins are seven transmembrane proteins (Fig. 4) that contain a retinal chromophore in the all-trans configuration. Retinal is derived from vitamin A and isomerizes into the 13-cis configuration after absorbing a photon. The retinal acts as the light sensor within the opsin. Its isomerization causes a rapid conformational change in the core protein which opens the pore [10], [38].

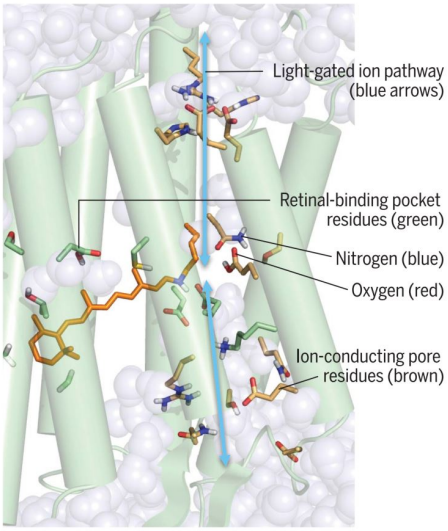

Figure 4: Structure of channelrhodopsin. The precise crystal structure of the cation-conducting channelrhodopsin C1C2 (a chimera between the original channelrhodopsin1 and channelrhdopsin2) was discovered in 2012 [39]. Microbial opsins are seven transmembrane proteins (green cylindrical transmembrane domains) that bind retinal (orange molecule containing ring). The retinal is covalently attached to the protein and photoisomerizes after absorption of a photon which causes a conformational change in the core protein and the opening of the pore (blue pathway for ions). Figure adapted from [35].

1.3.2 Examples of Optogenetic Tools

Optogenetic tools can be classified into different groups based on their form (pump or ion channel); their ion selectivity, which determines whether the tool is actuating or inhibiting; their kinetics, which set the maximum frequency at which cells can be stimulated; and their spectral properties, which determine the wavelengths needed to actuate the protein and thus dictate compatibility with other tools [40]. The channelrhodopsin used in the Boyden et al. seminal paper in 2005 was Channelrhodopsin-2 (ChR2), a light-gated cation channel that can be used to depolarize the neuronal membrane and thus has an actuating effect [9]. Various inhibitory optogenetic tools also exist and are valuable tools that can be used to silence neurons which can be helpful for the functional dissection of neural circuits. Archaerhodopsin-3 (Arch, which was also shown to work as a microbial opsin voltage indicator in section 1.2.3.2) is a light-activated proton pump [26] that pumps protons from the intracellular side to the extracellular side, thereby hyperpolarizing and inhibiting the cell. Beside proton pumps, there are chloride pumps such as halorhodopsin [11] that pump chloride ions into the cell, which also has a hyperpolarizing effect. Inhibitory light-gated ion channels are more efficient way of inhibiting neurons since they can transport ions more rapidly than pumps. They were elusive for a long time; however, the discovery of the cation-conducting C1C2 channelrhodopsin crystal structure in 2012 [39] laid the foundation for engineering solutions to this lack. Two separate engineering efforts led to the engineered anion channelrhodopsins (eACRs) iC++ [41] and iChlOC (improved chloride conducting

channelrhodopsin) [42]. Around the same time, a naturally occurring ACR was discovered in the cryptophyte alga *Guillardia theta* and was thus named "GtACR" [13].

Besides differing in ion selectivity, rhodopsins come in different kinetic flavors and modes of operation. Chronos is one of the fastest channelrhodopsins to date with an on-constant of 2.3 ms and an off-constant of 3.6 ms [12]. Most efforts had previously gone into reducing the off-time constant to accelerate the channelrhodopsin kinetics. However, slowing down the off-time constant turned out to be very useful since it led to the discovery of bistable channelrhodopsins termed step-function opsins (SFOs) that were photo-switchable between the active 'ON' state and the inactive 'OFF' state [35], [43] (Fig. 5c,d).

Finally, rhodopsins have different spectral properties. Most excitatory channelrhodopsins require activating wavelengths in the blue light spectrum (around 470 nm). However there is a lot of interest in having channelrhodopsins that are activated in the red light spectrum, in order to be able to achieve simultaneous control over two different neural populations with the combination of a blue-shifted and a red-shifted opsin; or to be able to combine neural activation with blue-light activated imaging techniques such as many types of calcium indicators. VChR1 was the first appreciably red-shifted opsin that could drive spiking at 589 nm [44], [35]. Since then, research efforts have produced Chrimson, which can reliably generate photocurrents at 625 nm [12]. Chrimson was shown to work together with Chronos (blue-light excited) to achieve simultaneous and independent optical actuation of different subsets of neurons [12].

An example of possible neural traces that can be achieved with different channelrhodopsins is illustrated in Fig. 5.

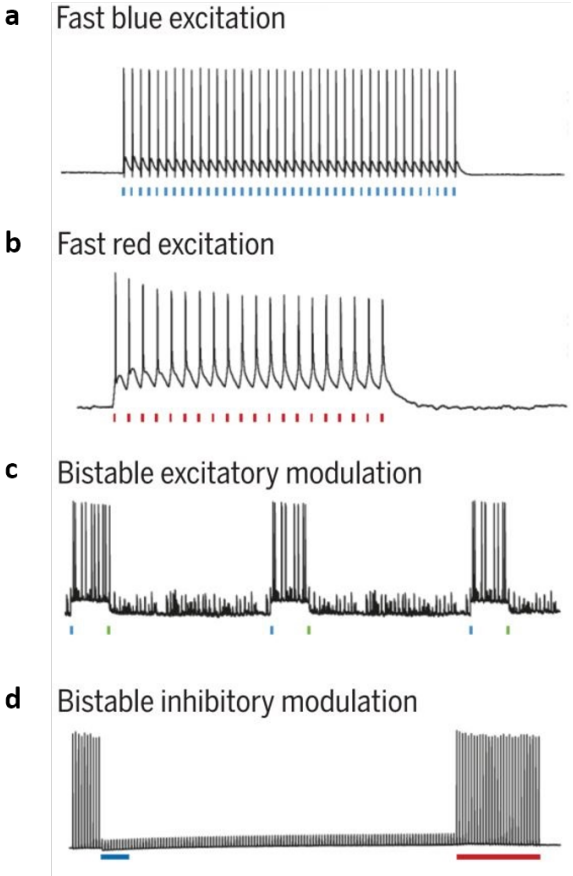

Figure 5: Examples of optogenetic modalities. **(a)** Fast excitatory channelrhodopsins such as Chronos can reliably drive spiking with blue-light excitation up to 60 Hz [12]. **(b)** Red-shifted channelrhodopsins such as ChrimsonR (a variant of Chrimson with improved off-kinetics) can mediate red-light driven spiking at frequencies up to 20 Hz. **(c)-(d)** Bistable step function opsins (SFOs) can be used to achieve photo-switchable activation (**c**) or inhibition (**d**) [35]. Figure adapted from [35].

1.3.3 Opsin Chosen For This Study

The actuating channelrhodopsin CoChR (for Chloromonas oogama channelrhodopsin, the former being the algal species in which it was discovered) was chosen for this study mainly due to its exceptionally high photocurrent in the blue wavelength range. Fig. 6a shows that the 470 nm photocurrent is around 3500 pA, which is well above that of the other opsins screened by Klapoetke et al. [12]. We prioritized the high photocurrent during the opsin selection since previous studies conducted in this lab suffered from low efficiency stimulation due to lower photocurrents. The kinetics of CoChR are on the slow side, especially compared to the ultrafast opsin Chronos. CoChR has a time to 90% peak of around 5 ms (Fig. 6b) and a τ_{off} of around 100 ms (Fig. 6c). These kinetics limit the frequency at which APs can be triggered in neurons to about 10 Hz, which was compatible with the applications in this study. CoChR is comparatively photostable (Fig. 6d).

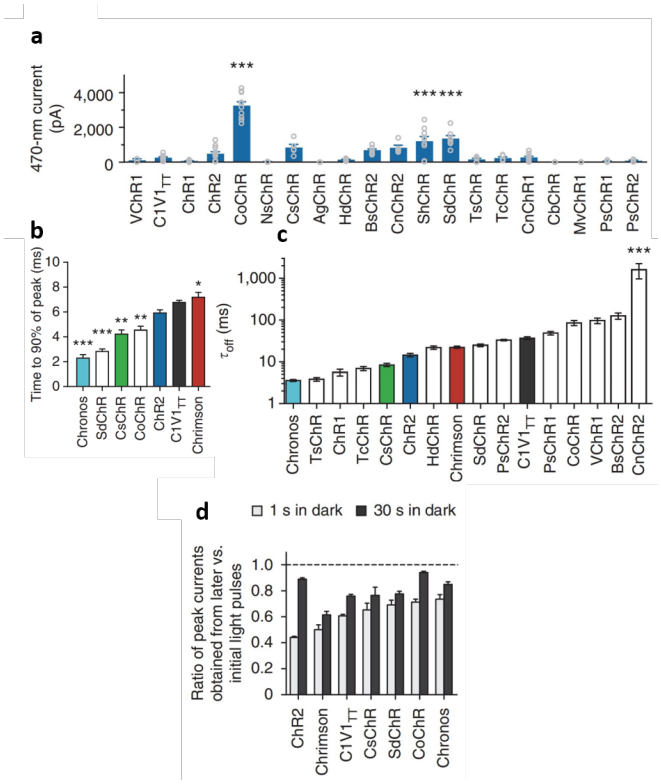

Figure 6: Characteristics of CoChR and other opsins. **(a)** Peak photocurrents measured in cultured neurons (murine) during 5 ms illumination at 470 nm and 4.23 $\frac{mW}{mm^2}$. **(b)** Time-to-peak was determined after illumination at 470 nm for 1 s at 5 $\frac{mW}{mm^2}$. **(c)** The off-time constant was determined under the same conditions as in **a**, using a monoexponential fit. **(d)** Recovery kinetics were measured with 3 subsequent pulses of 1 s duration, with the second one occurring after 1 s in the dark and the third one occurring after 30 s in the dark. The illumination conditions were the same as in **a**. Figure adapted from [12].

1.4 Excitation and Imaging Technique

The actuating channelrhodopsin was targeted either by wide-field light, by two-photon scanning or by a light-sheet, while the voltage reporter was always excited using a light-sheet. Two-photon excitation uses two lower energy photons (longer wavelength, e.g. infrared) that need to be absorbed almost at the same time to replace one higher-energy photon (shorter wavelength, e.g. blue). This greatly reduces out of focus excitation light since it is a non-linear process and the coincidence of two-photons depends on the square of the light intensity, thus excitation decays quadratically outside of the focal spot. The reduction in focal excitation volume that comes with this technique is excellent for precise single-cell excitation purposes as well as for limiting photodamage. Furthermore, longer wavelengths experience reduced scattering and can thus penetrate deeper into the tissue [45].

Light-sheet fluorescence microscopy or single plane illumination microscopy (SPIM) is a way to achieve optical sectioning (the detection of in-focus light only) by simply not generating any out-of-focus light while still being able to profit from the fast read-out speeds of a camera as in widefield microscopy. This technique also allows the simultaneous excitation of many GEVIs in parallel without loss of temporal resolution which enables the functional imaging of many neurons in parallel. A thin sheet of light is generated, typically using a cylindrical lens, that will excite only a very thin nearly two-dimensional fraction of the sample (Fig. 7). The excitation path is orthogonal to the imaging path. Using this technique, out-of-plane fluorescence is absent [46]. Zebrafish larvae are especially amenable to light-sheet imaging since they are completely transparent and therefore light from the side can easily pass through the skin and reach neurons. Examples of light-sheet imaging in zebrafish larvae can be found in refs. [47] and [48].

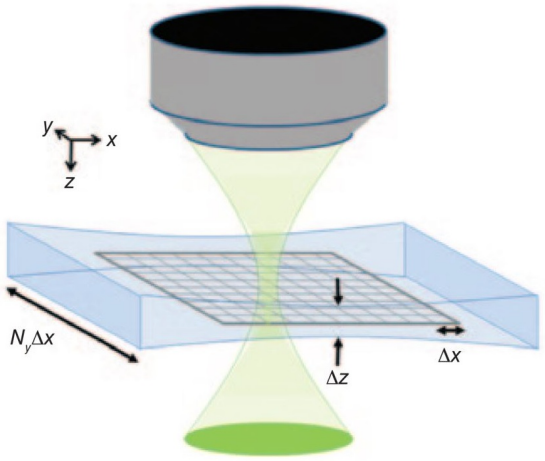

Figure 7: Single plane illumination microscopy. The excitation light (blue) comes from the side and is focused into a very thin sheet of light that traverses the sample and illuminates only a very thin, almost two-dimensional plane. The imaging path (green) is orthogonal to the excitation path and captures only fluorescence resulting from the single illuminated plane, thereby achieving optical sectioning. Figure adapted from [46].

1.5 Model System - Zebrafish

The zebrafish (*Danio rerio*) is a powerful model system since it is very well established and a large tool-kit exists for it, e.g. tools for genetic manipulation. Zebrafish are a vertebrate species, and thus more similar to humans than other well established model systems. The fact that zebrafish pigment mutants are available which are very transparent (and almost completely transparent as larvae) is especially beneficial for imaging. This allows for the use of techniques such as light-sheet imaging. In this study, nacre [49] and casper fish [50] were used (Fig. 8). Other advantages include the fact that zebrafish have a fast generation time with hatching after ∼3 days and maturity after 90 days. Furthermore, they are easy to modify genetically. The zebrafish is a convenient model system to study the brain and spinal cord since the smaller size of their brain compared to other vertebrate model organisms allows to study simpler circuits and to image more of a given circuit at once [51].

In this study, the focus is on the zebrafish spinal cord. This is a convenient place to test new tools for connectivity mapping and measuring E/I balance as well as studying motor behavior since neural activity in the spinal cord is almost exclusively linked to swimming, with some cells displaying rhythmic firing patterns due to the left-right alteration of muscle contractions during swimming.

The *vglut2a* promoter [52] as well as the *HuC* promoter [53] were used in the research presented here. In wild-type fish, the *vlgut* promoter drives expression of a vesicular glutamate transporter that is necessary to transfer glutamate into synaptic vesicles. The *vglut2* promoter can thus be used to label glutamatergic cells [52]. The *HuC* promoter on the other hand is panneuronal and drives

expression for a protein that is important in neuronal differentiation [53]; thus it can be used to drive expression in all neurons.

The following will give a brief overview of aspects of the spinal motor circuits relevant to this study as well as explain how expression of constructs and transgenesis can be achieved in the zebrafish.

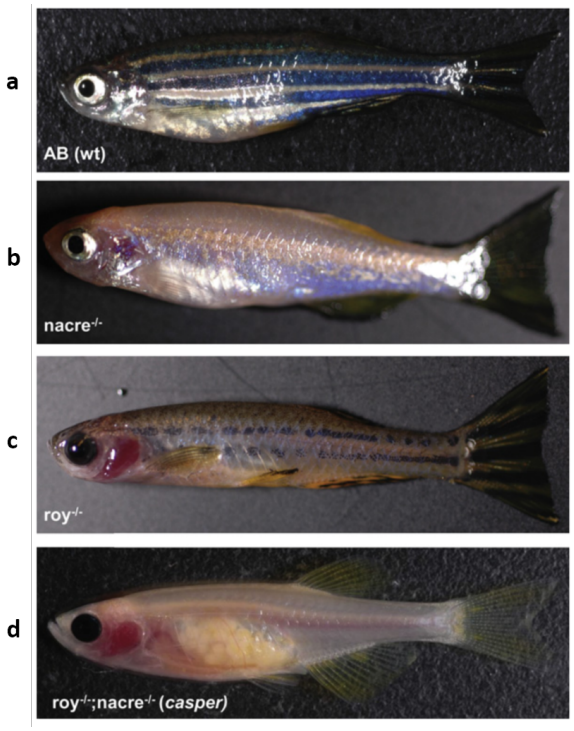

Figure 8: Zebrafish pigmentation. **(a)** Wild-type zebrafish contain three types of pigments in their skin: melanophores (responsible for the black stripes), xanthophores (responsible for the yellow color) and iridophores (which lead to the reflective pigment) [50]. **(b)** Nacre fish lack melanophores due to a mutation in the *mitfa* gene [49]. Nacre larvae, which were used in this study, are almost transparent even though adults are opaque. **(c)** Roy fish lack the reflective iridophores. **(d)** Casper fish (named after the ghost Casper) lack melanophores and iridophores, making them almost completely transparent. The eggs of the female are visible from the outside as a whitish material in the belly area [50]. Figure adapted from [50].

1.5.1 Zebrafish Motor Control

The zebrafish spinal motor circuits are only briefly discussed here and the key aspects relevant to this study are highlighted. A more comprehensive overview of so called central pattern generators (CPGs) implicated in locomotion and of spinal motor circuits in general can be found in refs. [54] and [55].

Five main components are needed to produce swimming in zebrafish. Motoneurons innervate the muscle and cause it to contract, which is the last step leading to the generation of movement. Ipsilateral and commissural (crossing midline) excitatory interneurons provide excitatory drive to motoneurons while inhibitory commissural interneurons are responsible for the left-right alternation that is needed to propel the fish forward. Finally, ipsilateral inhibitory interneurons are possibly involved in the termination of a swim bout [54] (Fig. 9). Motoneurons come in two main flavors; primary motoneurons which develop earlier and are active mainly at fast swimming speeds, and secondary motoneurons, which develop later and are recruited sequentially as the speed of swimming increases. Distinct interneurons innervate these motoneurons and are also recruited sequentially [56]. Among these excitatory interneurons are the circumferential ipsilateral descending (CiD) neurons and the multipolar commissural descending (MCoD) neurons which are both rhythmically active. Fluorescence voltage traces that are likely derived from these two cell types are shown in section 3.1 in this study.

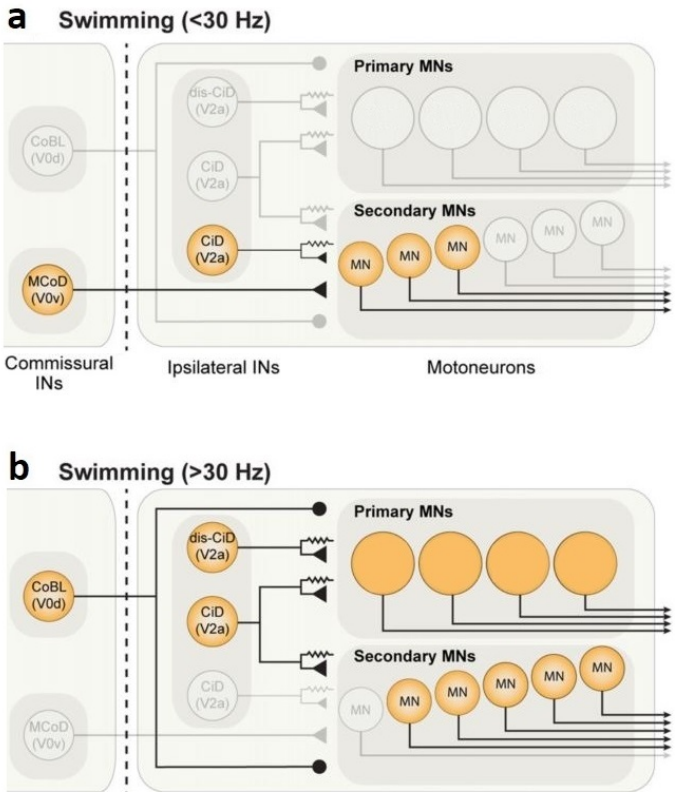

Figure 9: Simplified larval zebrafish spinal motor circuit involved in swimming. Distinct populations of motoneurons and interneurons are active at slow swimming speeds compared to fast speeds. **(a)** At slow speeds, excitatory drive is provided by ventral circumferential descending (CiD) interneurons to the secondary motoneurons active at slower speeds. Multipolar commissural descending (MCoD) neurons are also contributing to excitatory drive. **(b)** At faster speeds, primary motoneurons are active in addition to the fast subset of secondary motoneurons and more dorsal CiD interneurons are responsible for excitatory drive. Glycinergic inhibitory commissural longitudinal bifurcating (CoBL) neurons are likely contributing to left-right alternation. Figure adapted from [54].

1.5.2 Neuron Types Examined in This Study

In this study, an important part of the research was performed in zebrafish that expressed constructs necessary to perform optical electrophysiology in glutamatergic spinal interneurons. The above mentioned rhythmically active CiD and MCoD interneurons can be observed with voltage imaging and the proof of concept voltage traces for voltage imaging in zebrafish presented in this study could stem from these cell types (see section 3.1). Furthermore, part of this study focuses on a cell type that was previously identified in this lab to exhibit an interesting non-rhythmic firing pattern. These cells are likely to be ventral medial VeMe cells that were first mentioned and characterized by Hale et al. in 2001 [57] and later identified to be glutamatergic by Higashijima et al. [58]. VeMe cells are the most ventral glutamatergic interneurons, located below the central canal, and are multipolar interneurons with long axonal projections [58] (Fig. 10).

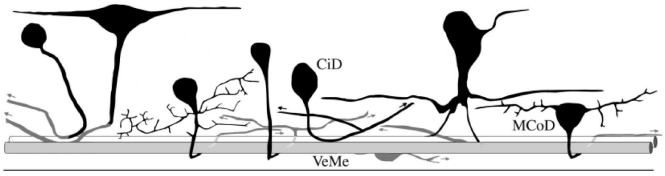

Figure 10: Subset of glutamatergic zebrafish spinal interneurons Ventral medial (VeMe) cells are below the central canal and have long axonal projections. Circumferential descending (CiD) interneurons and multipolar commissural descending (MCoD) interneurons provide excitatory drive to motoneurons. The former are ipsilateral while the latter have axons that cross the midline. Figure adapted from [57].

1.5.3 Expression and Transgenesis in Zebrafish

The two-component expression system Gal4-UAS [59] was used to drive expression of constructs needed for optical electrophysiology along with the direct use of the *HuC* panneuronal promoter. The Gal4-UAS system was used for the transgenic line which was established with the Tol2 system [60], [61]. Both systems are detailed in the methods section.

1.6 Mapping Connectivity

The aim of connectivity mapping is to determine which neurons or brain regions are connected to each other. Knowledge of this connectivity can provide fundamental insights into the function of neural circuits during behavior or their malfunction during disease. Two types of connectivity need to be distinguished: structural connectivity, which defines whether two neurons or brain regions are physically connected (for example through a synapse on the single neuron level); and functional connectivity, which can establish that the activation of one neuron or brain region has measurable consequences in another (e.g. a postsynaptic potential on a single neuron level). The focus within this study is on functional connectivity mapping; however a quick overview of structural connectivity is given first for context and better understanding.

1.6.1 Structural Connectivity

There are several ways to map structural connectivity and each comes with different advantages and limitations. An important aspect to consider is scale - connectivity can be determined at the micro-scale (nm - μm resolution to map individual synapses), the meso-scale (local circuits) or the macro-scale for entire brains (mm resolution).

Electron Microscopy (EM) has an advantage over conventional light microscopy (LM) in terms of resolution. The former can resolve structures down to 50 pm while the latter is diffraction-limited to about 200 nm [62]. So far, EM-efforts have been bottle-necked by the excessive amounts of time and labor required to acquire and analyze the resulting data. Thus a lot of effort has gone into speeding up the process. An example of a tentative solution to this problem is serial-section electron microscopy (ssEM). Using this technique, Hildebrand et al. acquired EM data from the whole zebrafish brain using an automated tape-collecting ultramicrotome to create sections that were then taped to silicon wafers for subsequent scanning electron microscopy [63], (Fig. 11). The data can be used, for example, to reconstruct neural projections to create a 'projectome'.

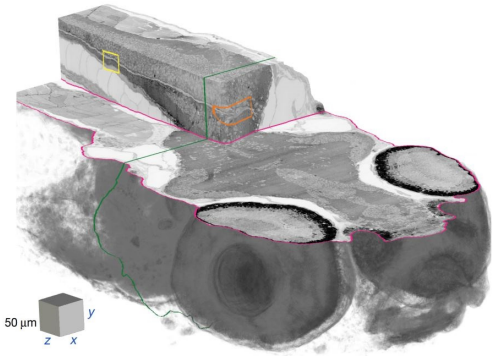

Figure 11: Serial-section electron microscopy (ssEM) of the larval zebrafish brain. Using ssEM, Hildebrand et al. captured the whole zebrafish brain. Portrayed here is a part of a reconstruction of the anterior quarter of a larval zebrafish based on 16 000 sections with a resolution of 56.4nm x 56.4nm x 60nm [63]. Figure adapted from [63].

There are also a multitude of creative light microscopy (LM)-based approaches to map connectivity, only a few of which will be briefly mentioned in the following. A palette of new super-resolution

LM approaches have also been recently developed and help to overcome the diffraction limit of resolution [62], however these will not be covered here.

The Brainbow [64] is an innovative approach to labeling thousands of neurons by expressing a random combination of fluorescent proteins in each neuron, which results in a large variety of different possible colors. Due to the random and combinatorial expression, nearby neurons are unlikely to be labeled with the same color. Thus this technique can be used to study very dense tissues at the single neuron level, since labeling in each individual fluorescent channel is sparse.

Another interesting technique is GRASP (GFP reconstitution across synaptic partners) [65] or the mammal compatible version mGRASP [66]. The basic concept is that GFP is split into two non-fluorescent fragments which are expressed on different cells and only emit fluorescent when they fuse, meaning that the two moieties are in close proximity, which indicates a potential synaptic contact.

Viral tracing is yet another very helpful method to establish synaptic contacts between neurons [67]. A popular example is trans-synaptic tracing with the Rabies virus that has been engineered to jump exactly one synapse in the retrograde direction where the starting cell population can be genetically defined [68].

Finally, many tools have been developed in parallel that facilitate structural connectivity mapping and can be used in combination with some of the techniques listed above. Examples of helpful tools include CLARITY [69] - a technique to render intact tissues optically transparent using a hydrogel system - and expansion microscopy [70], that allows to expand tissue several-fold by using a swelling polymer.

Collective efforts to map connectivity include the Human Connectome Project [71], the Allen Brain Atlas [72] and the Brain Initiative [73]. Hope and motivation is provided by *C. elegans*, whose 302 neurons have been entirely mapped [74].

1.6.2 Functional Connectivity

Functional magnetic resonance imaging (fMRI) is a popular tool to map functional connectivity in the human brain, thanks to its non-invasiveness [75]. However, results are merely correlative and spatial resolution typically remains in the mm-range while temporal resolution is on the scale of seconds, thus making this tool unsuitable to study brain circuits on a single neuron mechanistic level.

Historically, most approaches to map functional connectivity on the neuron level involved almost exclusively patch-clamp, which has a great temporal resolution and allows for good control over many experimental parameters as well as permitting the identification of cell type under study [67]. Patch-clamp experiments can, for example, prove functional connectivity by showing that an AP generated in one cell elicits a post-synaptic potential in another. The main drawback of this method is the fact that it is very low-throughput and a laborious process.

Nowadays, patch-clamp approaches to map functional connectivity remain very valuable but are complemented by optical techniques that have been made possible by the advent of optogenetics. An approach proposed by Petreanu et al. combines optogenetics and whole-cell patch clamp recordings in a technique which they called 'CRACM' (channelrhodopsin-2-assisted circuit mapping) [76]. CRACM can be used to determine functional connectivity between pre-synaptic neurons expressing channelrhodopsin and post-synaptic neurons that are recorded using patch clamp whole-cell recordings. The only drawback is again the fact that patch-clamp is laborious and thus this remains a low-throughput technique.

All-optical electrophysiology could be an interesting approach to improve throughput. Recently, Fan et al. demonstrated that it can be used to show lateral inhibition in Layer1 of the mouse barrel cortex [6]. Fan et al. showed, using a combination of voltage imaging and optogenetics, that a response can be observed in a target neuron when surrounding neurons are optogenetically stimulated. However, Fan et al. used bulk stimulation of many cells to show a response in another cell, while the aim of this study is to explore the possibility of using all-optical electrophysiology to establish one-

to-one functional connectivity in live zebrafish larvae. The approach combines voltage imaging with a red-excited GEVI and a blue-excited channelrhodopsin to excite a single neuron while recording from a multitude of potential postsynaptic cells in parallel. A causally linked postsynaptic potential in one of the imaged cells would indicate functional connectivity. The zebrafish has around 100 000 neurons [77], so establishing a full functional connectome is not the first goal. However, the work presented in this study is a first step toward making all-optical electrophysiology a common technique to map functional connectivity. In the future, it could be used to map functional connectivity of local microcircuits, which would be hard using patch-clamp electrophysiology.

1.7 E/I Balance

Measuring membrane potential is a first step towards a more in-depth comprehension of neural circuits. However, membrane voltage alone does not provide insights regarding the composition of the inputs to a cell. Multiple patterns of excitation (E) and inhibition (I) could explain a single voltage trace (Fig. 12). It would be useful to resolve the excitatory and inhibitory synaptic contributions that lead to a certain voltage time-trace. Various efforts have previously been made in the direction of describing conductance dynamics. In the following, a selection of different techniques will be presented in chronological order of their discovery; from multi-trial approaches that give an insight into the average relationship of excitatory and inhibitory conductances to single-trial approaches that can quantify E and I simultaneously.

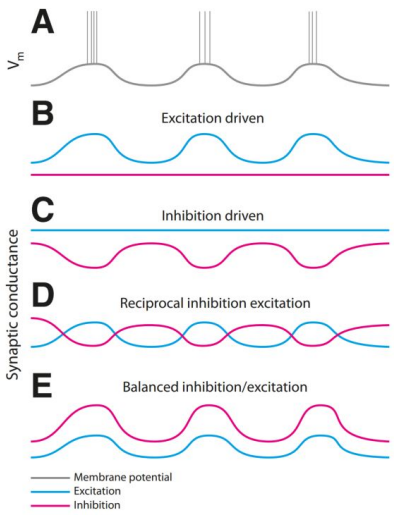

Figure 12: Various combinations of excitatory and inhibitory synaptic inputs can lead to the same membrane voltage trace in (A). The pattern could be excitation driven (B), inhibition driven (C), the result of out-of-phase oscillation of both (D) or the in-phase oscillation of both ("balanced E/I") (E). Figure adapted from [78].

1.7.1 Multi-Trial Ohmic Method

Synaptic conductance can be quantified using patch-clamp electrophysiology with several alternative approaches, which are summarized by Monier et al. [79]. The following example illustrates how to extract the excitatory and inhibitory conductances (G_e and G_i) in current-clamp. Equation 1 describes the membrane voltage dynamics assuming that the neuron can be considered to be a single electrical compartment [79], [80]. C_m describes the membrane capacitance, V_m is the membrane voltage, G_{leak} is the leak conductance that establishes the resting membrane potential, E_{leak} is the resting membrane potential, E_i is the inhibitory reversal potential, E_e is the excitatory reversal potential and I_{inj} is the injected current.

$$C_m \frac{dV_m(t)}{dt} = -G_{leak}(V_m(t) - E_{leak}) - G_e(t)(V_m(t) - E_e) - G_i(t)(V_m(t) - E_i) + I_{inj} \quad (1)$$

The aim is to calculate the excitatory and inhibitory conductances G_e and G_i based on this equation. Usually, the steady state condition is assumed and the cell capacitance is ignored. This means that the time dependence in the equation disappears and the membrane voltage V_m is assumed to be the steady state membrane potential which is induced in the cell after injection of current I_{inj}. This assumption is a reasonable approximation if the expected changes of synaptic conductances are on a time scale which is much larger than the membrane time constant associated with the capacitance C_m. Under these assumptions, equation 1 simplifies to equation 2.

$$0 = -G_{leak}(V_m - E_{leak}) - G_e(V_m - E_e) - G_i(V_m - E_i) + I_{inj} \tag{2}$$

G_{leak}, E_{leak}, E_e and E_i are assumed constant and can be estimated beforehand, while I_{inj} is set by the experimenter and V_m is measured. Therefore, there are two unknowns in equation 1: G_e and G_i. Two equations are needed to find two unknowns and the way this is achieved in practice is by using (at least) two different levels of current I_{inj} and measuring the membrane voltage V_m that this current injection induces in the cell. These results can then be used to solve the system of equations (3) for the unknowns G_e and G_i.

$$\begin{cases} -G_{leak}(V_m^1 - E_{leak}) - G_e(V_m^1 - E_e) - G_i(V_m^1 - E_i) + I_{inj}^1 = 0 & \text{(3a)} \\ -G_{leak}(V_m^2 - E_{leak}) - G_e(V_m^2 - E_e) - G_i(V_m^2 - E_i) + I_{inj}^2 = 0 & \text{(3b)} \end{cases}$$

E_{leak} is usually assumed to correspond to the resting membrane potential when no activity of interest is observed in the cell. G_{leak} can be estimated during the same resting condition by injecting current, measuring the steady state membrane potential it induces and using Ohm's Law to solve for for the conductance. E_i can be determined by using different current injection levels and observing where the inhibitory postsynaptic potentials (IPSPs) reverse. The excitatory reversal potential is harder to measure since a lot of current would have to be injected to reverse the excitatory post-synaptic potentials (EPSPs), which might harm the cell. It is often simply assumed to be around $\sim$0 mV [81].

One should keep in mind that the simple model in equation 1 does not take any time-varying intrinsic conductances, such as voltage-gated sodium, potassium or calcium channels, into account. The former are mainly needed to fire action potentials and only induce brief current transients that can usually be neglected. The calcium conductance could be added as a variable to the model to be more accurate [81].

The multi-trial approaches described here require the recording of multiple current or voltage traces at different holding potentials or current levels respectively, and thus statements can only be made about the average relationship between excitatory and inhibitory conductances.

1.7.2 Single-Trial Approaches to Measure E/I

Okun and Lampl came up with a method to record both excitatory and inhibitory currents at once, by exploiting the fact that nearby neurons in the cortex receive highly correlated synaptic inputs [82]. They first demonstrated that excitatory and inhibitory inputs to neighboring cells were highly correlated. They then hyperpolarized one cell to show excitatory currents while they simultaneously depolarized a neighboring cell to reveal inhibitory currents (Fig. 13). The cell was prevented from spiking. Like this they were able to visualize the instantaneous relationship of both E and I at once.

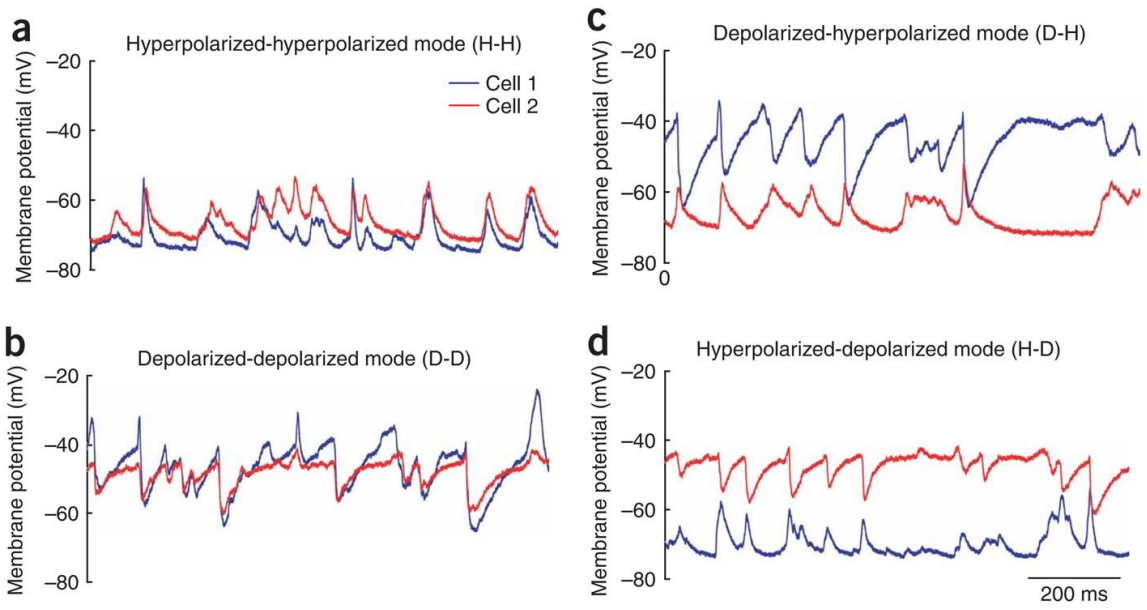

Figure 13: Okun and Lampl showed that neighboring cells in the cortex received similar excitatory (a) and inhibitory (b) inputs. They exploited this synchrony to simultaneously display excitatory and inhibitory currents by hyperpolarizing one cell and depolarizing another (c and d). Figure adapted from [82].

A disadvantage of this method is that a change in the apparent relation of E and I might be due to an actual change in synaptic inputs to the cells, or it might be due to a change in synchrony between the two cells. Efforts have therefore been made toward engineering single-trial approaches that do not require prior assumptions concerning the correlation of synaptic inputs to neighboring cells.

Berg. et al have recently come up with a method to extract the excitatory and inhibitory conductances based on a single trial from one cell [81]. They extract the membrane time constant τ from the decay of the autocorrelation of the membrane potential fluctuations and calculate the total conductance G_{tot} based on τ (Eq. 4). This allows them to combine equations 2 and 5 to extract G_e and G_i from a single voltage trace. Berg et al. extract the time constant from windows of 300 ms for which they assume that the membrane voltage signal is stationary and calculate the inhibitory and excitatory conductances for these windows.

$$\tau = RC = \frac{C}{G_{tot}} \tag{4}$$

$$G_{tot} = G_e + G_i + G_{leak} \tag{5}$$

Spikes can bias the estimates of excitatory and inhibitory conductances, therefore traces with low numbers of spikes should be used. Spikes can, for example, be prevented during measurement by injecting a negative current or they can be removed in a post-processing step. Gap junctions are also a source of error that should be considered. If they are ubiquitously present, this can bias results and therefore Berg et al. suggest to asses their presence with histological techniques if this is a concern [81].

Even more recently, a new method for extracting excitatory and inhibitory conductances with a single-trial approach was proposed [83]. This method relies on extracting the total conductance by injecting a high-frequency sinusoidal current and using AC circuit analysis. The remaining steps are similar as for the method proposed by Berg et al; the methods mainly differ in the technique that is used to calculate the total conductance.

1.7.3 How All-Optical Electrophysiology Can Contribute To E/I Measurement

This study explores the potential of applying all-optical electrophysiology all to quantify E/I-Balance. Essentially, an approach similar to the one used by Berg et al. [81] could be employed. While Berg et al. used the auto-correlation of the voltage signal decay to estimate the time constant of the membrane τ, the approach proposed here uses optical methods to estimate τ. Equation 2 becomes equation 6 in this case, where the current term I_{inj} from equation 2 was replaced by the channelrhodopsin induced current and G_{ChR} is the channelrhodopsin conductance while E_{ChR} is the channelrhodopsin reversal potential.

$$0 = -G_{leak}(V_m - E_{leak}) - G_e(V_m - E_e) - G_i(V_m - E_i) - G_{ChR}(V_m - E_{ChR}) \tag{6}$$

The idea is to use weak blue light pulses at 5- 10 Hz that actuate the excitatory channelrhodopsin and cause transient depolarization in the neuron to be probed. When the blue light switches off after the short pulse, the membrane potential decays back to baseline with a time-constant τ. Thus τ could be extracted from a monoexponential fit to the decaying membrane potential after the blue light switches off. Since we are only considering decay dynamics after the blue light has switched off and are assuming steady state at the point when the membrane potential has decayed back to its resting value, the conductance of the channelrhodopsin G_{ChR} is zero and equation 6 simplifies to equation 7 where V_m is membrane potential after decay from the channelrhodopsin induced depolarization back to resting membrane potential. After obtaining τ from the exponential fit to the membrane potential decay following the blue light pulse, equation 4 can be used to extract the total conductance G_{tot}. The membrane capacitance C_m in equation 4 can be estimated based on the total area of the membrane, its thickness as well as the dielectric constant [81]. Subsequently, equations 5 and 7 represent two equations with two unknowns that can be solved for G_e and G_i.

$$0 = -G_{leak}(V_m - E_{leak}) - G_e(V_m - E_e) - G_i(V_m - E_i) \tag{7}$$

At 10 Hz, the blue light cycles have a duration of 100 ms and therefore the membrane time constant could be extracted every 100 ms. This defines the time resolution with which E/I-balance can be determined since the excitatory and inhibitory conductances are approximated to be constant within this interval.

2 Methods

All procedures were performed according to the National Institutes of Health (NIH) guide for care and use of laboratory animals and the Harvard Institutional Animal Care and Use Committee (IACUC) protocols. The analyses for this study were performed in Matlab (Mathworks). Hardware components on the optical setup were controlled with LabVIEW (National Instruments).

2.1 Constructs for All-Optical Electrophysiology

To achieve cross-talk free optical electrophysiology, the red-shifted voltage indicator zArchon [4], which is the zebrafish codon-optimized version of Archon1, was combined with the blue-light excited channelrhodopsin CoChR [12]. In all constructs employed in this study, the spectrally orthogonal fluorescent proteins GFP and mOrange were used to label zArchon and CoChR respectively. In order to establish all-optical electrophysiology, the voltage indicator and the channelrhodopsin were co-expressed in the same cells. In one case, two separate constructs were used to achieve this, while in most cases, bicistronic constructs were created with help of the T2A linker sequence [84]. The T2A sequence encodes a small self-cleaving peptide which ensures the separation of the two constructs after translation. The channelrhodopsin CoChR was soma-localized in all constructs, using the soma-targeting sequence of the potassium channel Kv2.1 [85]. The channelrhodopsin was soma-localized to enable a more precise stimulation of specific cells without exciting nearby axons. Most constructs contained the *UAS* promoter to make use of the Gal4-UAS two-component expression system [59], which is explained below. One construct, which was used for most of the experiments, contains the panneuronal *HuC* promoter [53]. One construct contains the *cmlc2* promoter which drives expression in the heart and can serve to label transgenic zebrafish to simplify the screening process. The plasmid containing the construct *UAS:zArchon-GFP* was obtained from the Cohen Lab while the constructs listed below were cloned specifically for this study.

1. *UAS:CoChR-mOrange-Kv2.1*
2. *UAS:zArchon-GFP-T2A-CoChR-mOrange-Kv2.1*
3. ***HuC:****zArchon-GFP-T2A-CoChR-mOrange-Kv2.1*
4. *UAS:zArchon-GFP-T2A-CoChR-mOrange-Kv2.1, cmlc2:GFP*

2.1.1 Gal4-UAS System

The Gal4-UAS system involves the activator protein Gal4 - originally derived from yeast - which binds to the upstream activating sequence (UAS), thus activating transcription of the genes downstream of the UAS [59] (Fig. 14). The Gal4-UAS system allows for the separation of the activator and effector elements. This means that an activator strain can express Gal4 under a cell-specific promoter and the effector strain can express a gene of interest downstream of the UAS sequence in all cells. When the two strains are crossed, the offspring will express the gene of interest only in cells where both Gal4 and UAS are present. We opted for the Gal4-UAS system since it enables transcriptional amplification and offers flexibility - the same Gal4 actuator line can be crossed to many different UAS reporter lines to express different target genes. Conversely, the same UAS reporter line can be crossed to multiple different actuating lines expressing Gal4 under different promoters.

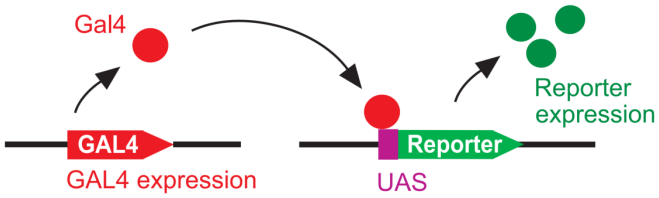

Figure 14: Gal4-UAS System. The Gal4 protein can bind to the upstream activating sequence (UAS) to initiate transcription of genes downstream of the UAS. This system allows for the separation of activator and effector strains, which leads to transcriptional amplification. With the help of the Tol2 transposase, DNA between two Tol2 sequences can be excised and integrated into the genome, which enables the creation of transgenic fish lines. Figure adapted from [59].

2.2 Cloning

Plasmids were designed using *Geneious 11.1.5*. The Gibson method was selected for cloning [86] and the NEBuilder tool [87] was used to design Gibson-compatible primers. The primers were ordered from IDT [88]. The backbone was linearized with suitable restriction enzymes and then treated with FastAP (ThermoFisher Scientific) to prevent backbone self-ligation. PCR amplification of inserts was performed using the *Phusion High-Fidelity PCR Master Mix with HF Buffer* (New England Biolabs) and PCR products were treated with Dpn1 (New England Biolabs) to digest template plasmid. Gibson ligation of backbone and inserts was performed using the *Gibson Assembly Master Mix* (New England Biolabs). *Stable competent E. coli (high efficiency)* cells (New England Biolabs) were used for transformation. Carbenicillin was used to select for colonies that expressed the plasmid which contained a carbenicillin resistance gene. Isolated plasmids were sequenced using Genewiz [89].

2.3 Construct Expression in Zebrafish

Zebrafish (*Danio rerio*) adults were kept at 28°C on a light cycle that comprised 14h of light and 10h of dark. Adult zebrafish were used for breeding purposes. Construct expression in zebrafish was achieved by the means of transient expression using zebrafish embryo micro-injections (detailed below). For constructs using the two-component Gal4-UAS expression system, a glutamatergic and a panneuronal driver line were used. The gluatamatergic driver line was a transgenic line of genotype *vglut2a:Gal4;UAS:zArchon-GFP* which was obtained from the Boyden Lab at MIT. The original *vglut2a:Gal4* driver line was established by Satou et al. [90]. The panneuronal driver line was of genotype *HuC:Gal4* and was generated by Mensch et al. [91].

2.3.1 Transient Expression

Transient expression in zebrafish was achieved by the means of zebrafish embryo injections into the 1-2 cell stage. To obtain embryos, adult zebrafish were set up in crossing tanks the night before, with a divider separating the male and female fish. The divider was removed the next morning, allowing the fish to mate. Eggs in the 1-2 cell stage were collected 20 minutes after mating initialized. Adult zebrafish were either from one of the transgenic driver lines mentioned above, or if no driver was used, of genotype *nacre(mitfa-/-)* [49]. In some cases, crosses between a driver line and *nacre(mitfa-/-)* were used.

Approximately 1 nL of injection solution was injected per embryo. The injection procedure is described in [60]. The injection solution contained 20-30 ng/μL of plasmid DNA containing the desired construct (0.02 - 0.03 ng per embryo), 100 mM KCl, 0.05% Phenol Red, 25 ng/μL Tol2 transposase mRNA ($\sim$0.025 ng per embryo) and nanopure filtered water. Tol2 transposase mRNA was added to boost transient expression levels by enabling construct insertion into the zebrafish genome. The Tol2 system is explained below in section 2.9.1 and was also used for the creation of a transgenic line within this study.

2.4 Preparation of Zebrafish Larvae for Imaging

Zebrafish larvae were imaged at 4-6 days post fertilization. To ensure immobilization during imaging, the larvae were paralyzed using the neuro-muscular junction blocker alpha-bungarotoxin (Invitrogen). The fish were immerged in 50 μL of 1 mg/mL alpha-bungarotoxin for 2 min. Following paralysis, the fish were mounted in 1.5% low melting point agarose (Sigma) on a custom-built pedestal for subsequent imaging. The pedestal with the larva was immersed in zebrafish facility system water inside a custom-built chamber.

2.5 Optical Setup and Imaging

A custom-built optical setup that was equipped with a 488 nm (blue), a 532 nm (green) and a 637 nm (red) laser line (Obis, Coherent), as well as a CMOS camera (Hamamatsu CMOS C11440), a tunable infrared laser (InSight DeepSee, Spectra Physics) and a photomultiplier tube was used for imaging experiments. The optical setup enabled the use of three light paths: 1P light sheet, 1P widefield and 2P scanning (Fig. 15). The red, green and blue laser lines were combined onto the same path using dichroic mirrors and directed towards an acousto-optic tunable filter (Gooch and Housego) in order to modify the intensity of the different wavelengths in time. Subsequently, the beams were expanded and focused onto the back-focal plane of the objective (light sheet objective: Olympus, 4x, NA 0.28; Olympus, imaging objective: Olympus, 25x, NA 1.05, water-immersion). The red, green and blue laser lines were directed either onto the light sheet path or onto the widefield path. The infrared tunable laser was set to 930 nm and used on the 2P scanning path only.

The green laser was used at 2.3 $\frac{mW}{mm^2}$ to stimulate mOrange to identify CoChR expressing cells. The blue laser was used to excite the GFP-tag on zArchon (0.2 $\frac{mW}{mm^2}$) and, more importantly, to stimulate CoChR. CoChR was stimulated at 0.22 - 9.2 $\frac{mW}{mm^2}$ using 1P blue light sheet excitation, 0.2 - 0.8 $\frac{mW}{mm^2}$ using blue 1P widefield excitation and 5-18 mW using 2P scanning excitation.

Light sheet excitation was used to stimulate the voltage indicator zArchon at 66, 70 or 130 $\frac{W}{mm^2}$ at 637 nm for the first intensity and 639 nm for the last two. A 664 nm long-pass filter was placed before the camera. The image acquisition rate was 500 Hz (exposure time 2 ms) or 1 kHz (exposure time 1 ms). The maximum field of view that was imaged was 468 x 68 μm. In some cases, the imaged field of view was decreased to 91 x 91 μm.

To perform 2P scanning excitation, an image was first acquired using 2P excitation and a photomultiplier tube (PMT). A LabVIEW (National Instruments) software was used to draw a scanning pattern onto the acquired image. The pattern (cell contour circle or spiral) was scanned at 500 Hz, meaning that it was completed every 2 ms.

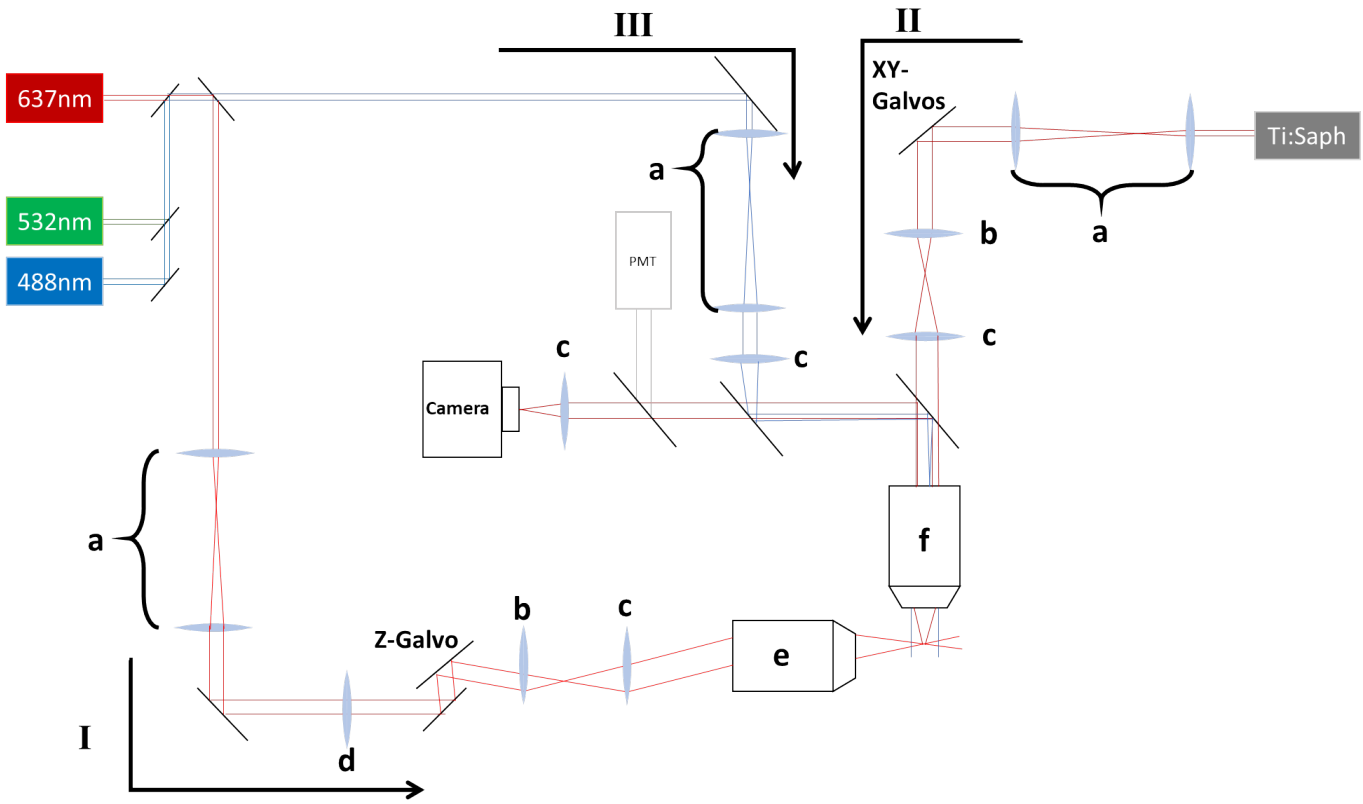

Figure 15: Optical System. Custom built setup with three different illumination paths. Schematic is simplified to contain the most important optics only. **Path I - Light sheet:** Laser beams are added to the same optical path using dichroic mirrors and then pass through a beam expander before going through a cylindrical lens which focuses light in the z-axis only, thus generating homogeneous excitation light for one optical plane in the z-axis. A galvo mirror is used to adjust the position of the light sheet in the z direction to select a specific optical plane. **Path II - 2-Photon Path:** The 2P path uses a Ti:Sapphire laser to generate an infrared light beam that can be scanned into a precise location using using X-Y galvo mirrors. A photomultiplier tube (PMT) can be used to acquire images with 2P excitation light. **Path III - Widefield Path:** Laser beams are expanded and pass through a tube lens before passing through the imaging objective and hitting the sample. **Components: a:** beam expander, **b:** scan lens, **c:** tube lens, **d:** cylindrical lens to generate light-sheet, **e:** light sheet objective, **f:** imaging objective. **Camera:** Hamamatsu CMOS C11440. **PMT:** photomultiplier tube.

2.6 Data Analysis

Data Analysis was performed using Matlab (Mathworks). Raw movies were loaded into Matlab and a custom-written program was used to select cell regions of interest (ROIs) and extract average fluorescence traces from them. In cases where $\Delta F/F$ was calculated, the following formula was used: $\Delta F/F = \frac{F(t)-F_0(t)}{F_0(t)-F_{bg}}$, where $F(t)$ represents the pixel intensity at each time point and F_{bg} is the background pixel intensity that did not include any cells. $F_0(t)$ was a low-pass filtered version of $F(t)$ which enabled the removal of photo-bleaching in the same step. For the E/I-balance analysis, high-pass filtered raw traces were used.

2.6.1 Spike-Triggered Averages

Spikes were identified by using a simple threshold where values within the trace that exceeded the threshold were classified as spikes. The threshold was determined by calculating a histogram of the triggering cell trace, fitting a Gaussian function to the histogram and extracting the standard deviation of the Gaussian fit. The threshold was set to be n times the standard deviation, where n varied between 3.5 and 4 and was adapted to the specific cell trace to optimize spike detection.

Spike-triggered average waveforms were calculated by extracting a window of 100 ms from all cells around each time point that corresponded to a spike in the triggering cell. The windows were

then averaged.

2.6.2 Blue Light-Triggered Averages

Blue light-triggered averages were calculated by extracting a window of 100 ms around each time point that corresponded to the switching on of blue light from all cells. The windows were then averaged to yield blue light-triggered average traces.

2.7 Mapping Functional Connectivity

A single CoChR-expressing cell in a *vglut2a:Gal4;UAS:zArchon-GFP* larva that was injected with *HuC:zArchon-GFP-T2A-CoChR-mOrange-Kv2.1* was stimulated with widefield blue light at 0.8 $\frac{mW}{mm^2}$, 10 Hz and 50% DC. Simultaneously, many surrounding cells were imaged that contained zArchon only. The aim was to identify a potential synaptic connection between the stimulated cell and the surrounding postsynaptic candidate cells. For this purpose, spike-triggered average waveforms were calculated where spikes from the stimulated CoChR containing cell were used as triggers. Spike-triggered average waveforms were checked for signs of postsynaptic potentials.

2.8 E/I Balance

Ventral medial (VeMe) cells were identified in the spinal cord of a *vglut2a:Gal4;UAS:zArchon-GFP* larva that was injected with a *UAS:zArchon-GFP-T2A-CoChR-mOrange-Kv2.1* construct and targeted with 1P widefield illumination at 10 Hz, 50% DC at 0.38 $\frac{mW}{mm^2}$. The larva was induced to start fictive swimming (motoneuron activity corresponding to swimming without muscle contraction due to paralysis) by a virtual water flow in the form of a moving grating that was projected beneath the fish. To prevent the fish from adapting to the stimulus and stopping to swim, a closed-loop system was used that translated the fish's fictive swimming attempts into movement of the grating. The closed-loop system to induce zebrafish swimming is explained by Ahrens et al. [92]. Briefly, a ventral nerve root (VNR) electrode was attached to the side of the fish, targeting the border between two spinal cord segments. The VNR electrode recorded motoneuron activity associated with swimming. Electrode output was amplified using an Axopatch 200B amplifier and then line noise (50-60 Hz) was removed using a noise eliminator (HumBug). The de-noised VNR signal was high-pass filtered and then the standard deviation was calculated in 10 ms windows using a Teensy microcontroller. The standard deviation was considered to be a swimming acceleration signal and was integrated to yield a speed signal which was used to control the speed of the grating below the fish. Like this, the fish was able to compensate for the virtual flow by its swimming action.

Four 20 s trials were acquired from the same two cells with 10 Hz blue light stimulation while the zebrafish larva was swimming as described above. Based on the ventral nerve root recording, we determined during which time periods the larva was effectively swimming in all four trials. Data was then pooled and blue light stimulus-triggered average waveforms (methods section 2.6.2) and spike-triggered average waveforms (methods section 2.6.1) were calculated. The decay phase of the blue-light triggered average waveform was normalized to an interval of zero to one in order to extract the time constant of the exponential decay as the slope at zero.

2.9 Transgenic Zebrafish Line for All-Optical Electrophysiology

A transgenic zebrafish line with the genotype *UAS:zArchon-GFP-T2A-CoChR-mOrange-Kv2.1* was created following the protocol in [60] using the the Tol2-system (see section 2.9.1). This was achieved by injecting a *UAS:zArchon-GFP-T2A-CoChR-mOrange-Kv2.1* construct into *nacre(mitfa-/-)* zebrafish embryos together with Tol2 mRNA. The injected plasmid contained a *cmlc2:GFP* heart-marker for screening purposes. The content of the injection solution was the same as for transient

expression (section 2.3.1). Tol2 mRNA was synthesized using the *mMessage mMACHINE SP6 Transcription Kit* (ThermoFisher Scientific) and Tol2 cDNA [61]. Initially, problems with mRNA degradation were encountered. Therefore, a recombinant RNase inhibitor (Takara Bio) was added to the injection solution (20 U/μL). Ten hours after injection, an excision assay following the protocol in [60] was performed to assess whether the target construct was successfully excised from the injected donor plasmid. In a first step, the assay checked for whole plasmids from which the target sequence had not been excised (as a control and to check for plasmid presence) and, in a second step, checked for plasmids from which the target sequence had been excised and therefore potentially introduced into the zebrafish genome. The primer sequences that were used in the non-excision case were: FWD-ACTGAGGAATTTAATGTGAC and REV-GAGTTAGCTCACTCATTAGG. The primers that were used for the excision case were FWD-TTATAGGAATGGAGACTACC and REV-ACAGCTATGACCATGATTAC.

Batches of injected embryos for which the excision assay suggested successful integration into the zebrafish genome were raised to the adult stage. After 2.5 months, potential transgenics were in-crossed and offspring was screened for heart marker expression that indicated presence of the construct. Adults that gave rise to transgenic off-spring (founder fish) were identified and moved to separate tanks. A founder fish was re-crossed and its transgenic off-spring was imaged using a Zeiss LSM-710 confocal microscope (40x objective, NA 1). A confocal stack was obtained with a z-step of 0.98 μm. The microscope was programmed using ZEN (Zeiss) to optimize illumination for the visualization of both mOrange expression and GFP expression which tagged CoChR and zArchon respectively.

2.9.1 Tol2 System

The Tol2 system offers an efficient method to create transgenic lines as well as to boost transient expression in zebrafish by enabling construct insertion into the zebrafish genome. The Tol2 transposon, discovered in medaka fish, enables the transposition of a construct up to 11 kb, flanked by the Tol2 recognition sequence, into the fish genome. Some transpositions occur in germline cells, which can give rise to transgenic fish [61]. Fig. 16 explains how to establish a transgenic line using the Tol2 transposase system.

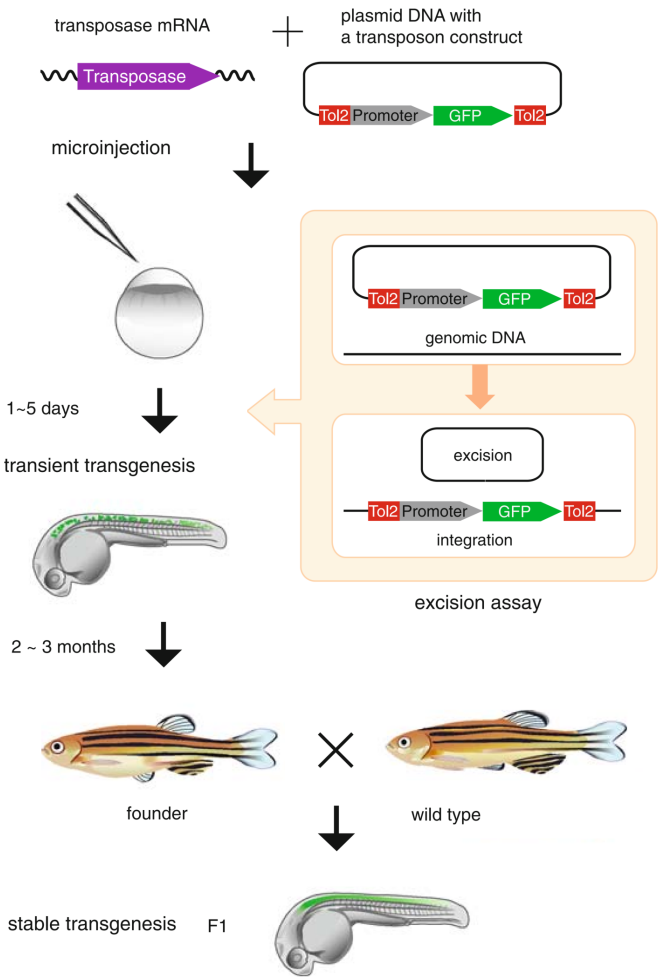

Figure 16: Transgenesis with the Tol2 system. To obtain zebrafish transgenics, a plasmid containing the target construct flanked by Tol2 recognition sequences is injected into zebrafish embroys together with transposase mRNA. After injection, the mRNA is translated into transposase within the embryo and mediates the excision of the Tol2 flanked target construct as well as its integration into the fish genome. The founder fish will exhibit mosaic expression since excision does not work equally well in all cells. The founder can be crossed to a wild type fish to yield stable transgenic offspring. The Tol2 system can also be used to boost transient expression. Figure adapted from [93].

3 Results

This work establishes all-optical electrophysiology in zebrafish and demonstrates its potential uses for functional connectivity mapping as well as for studying E/I-balance. Furthermore, a transgenic zebrafish line expressing the constructs necessary for all-optical electrophysiology was generated during this study.

3.1 Voltage Imaging in Zebrafish

Voltage imaging in zebrafish has been demonstrated in previous studies [4], [30]. *In vivo* voltage imaging during spontaneous zebrafish swimming is shown here to demonstrate that our imaging set-up is capable of reproducing the state of the art. A *vglut2a:Gal4;UAS-zArchon-GFP* transgenic zebrafish larva was paralyzed, embedded in agarose and imaged during fictive swimming. Fictive swimming relates to the fact that the larva cannot move since neuromuscular junctions have been blocked; however motoneuron output and other neuronal activity related to swimming can still be observed. Fig. 17a shows the average zArchon fluorescence during a recording trial. zArchon was excited at 639 nm and 130 $\frac{W}{mm^2}$ via light sheet excitation. Imaging was performed at 1 kHz, meaning that exposure time was 1 ms. Fig. 17b shows the cell ROIs (regions of interest) that were analyzed. $\frac{\Delta F}{F}$ is displayed for selected cells in Fig. 17c. Neuronal activity that can be observed in the fluorescence traces corresponds to swimming activity. A swim bout is labeled in Fig. 17c. The glutamatergic neurons that were imaged in this experiment likely correspond to CiD or MCoD interneurons that exhibit rhythmic activity. They provide excitatory input to motoneurons that then cause muscle contractions in non-paralyzed fish. During zebrafish swimming, muscle contractions happen in a left-right alternating manner to propel the fish forward. Thus neuronal activity is also left-right alternating. One can observe that cells which are located on the same side of the spinal cord show in phase activity (Fig. 18b) while cells located on opposite sides of the spinal cord show antiphase activity (Fig. 18c).

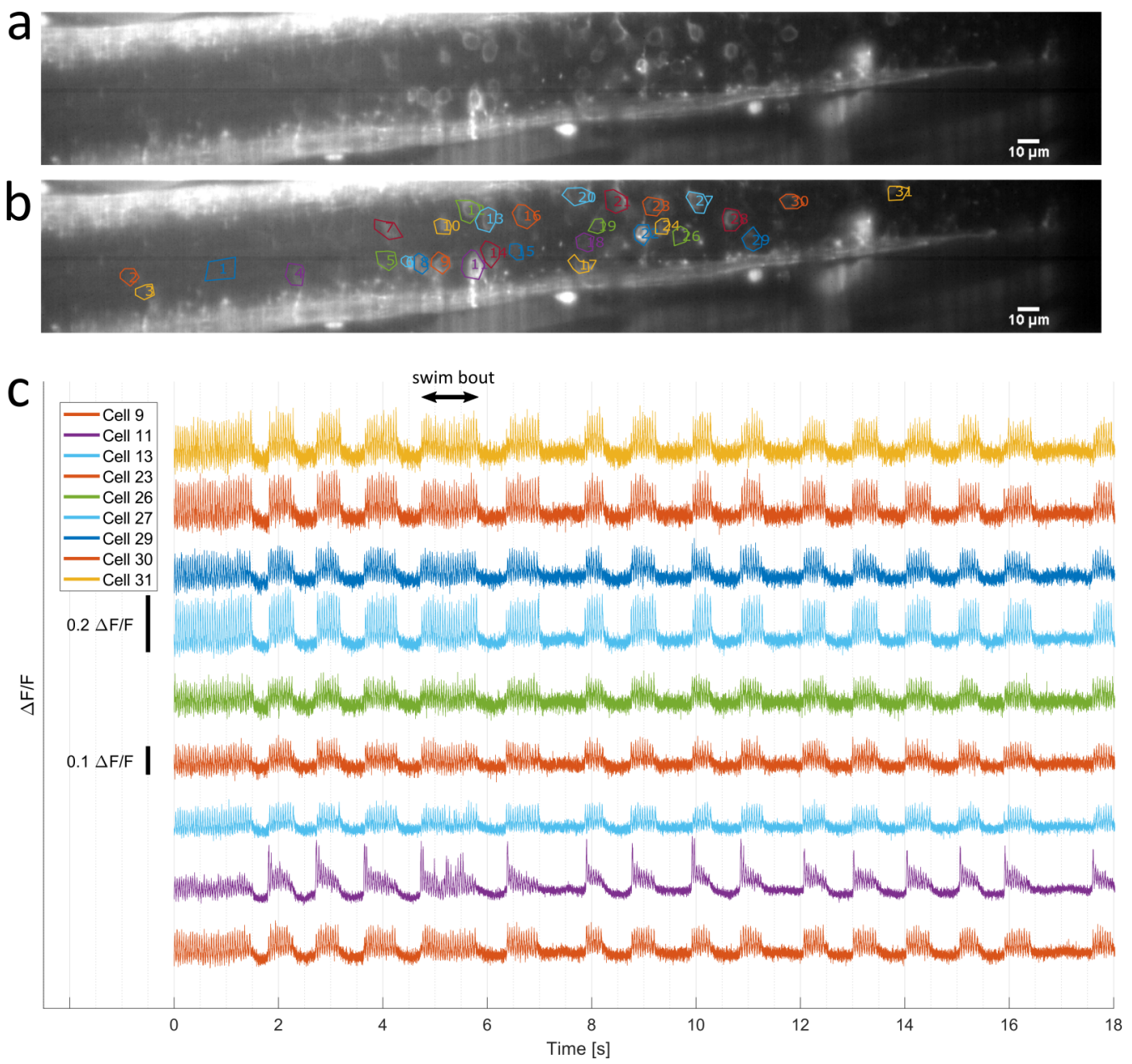

Figure 17: Voltage imaging *in vivo* in zebrafish during swimming. Voltage imaging was performed in a *vglut2a:Gal4;UAS:zArchon-GFP* transgenic larva that expressed the voltage indicator zArchon in glutamatergic cells. Spontaneous neuronal activity was observed in the spinal cord during so-called fictive swimming. It is called fictive swimming since the fish is paralyzed for imaging purposes, but neuronal activity related to swimming can still be observed. **(a)** Average fluorescence intensity in the zArchon channel of glutamatergic cells expressing the voltage indicator in the zebrafish spinal cord. **(b)** Cell ROIs from which fluorescence traces were extracted are marked. **(c)** $\frac{\Delta F}{F}$ of fluorescence traces for selected cells are shown. The colors and numbering correspond to the ROIs in **b**. While mainly subthreshold oscillations are visible in most of the traces, spiking activity can be observed in cell 11 (second from bottom).

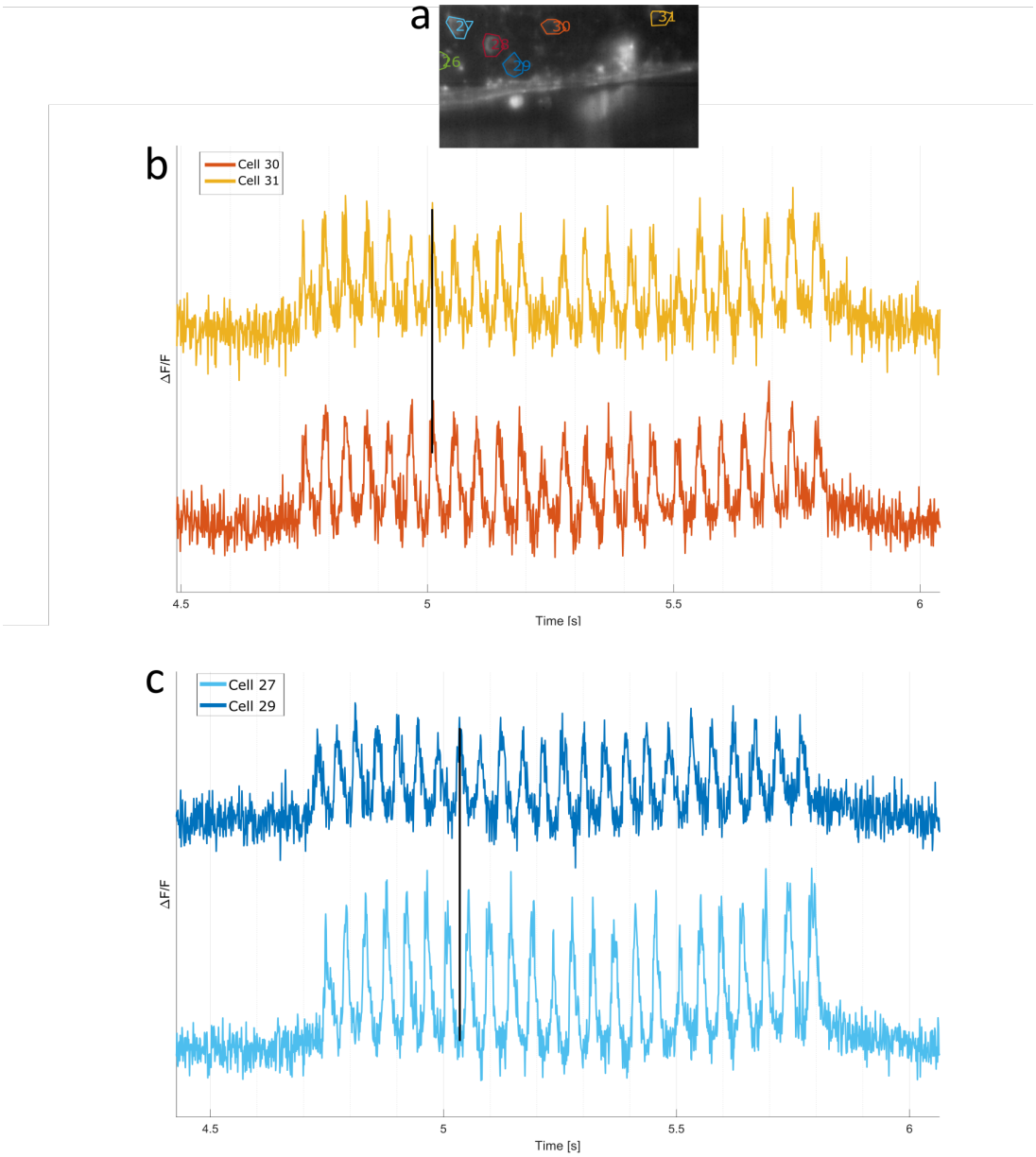

Figure 18: In phase and antiphase rhythmic oscillations in the zebrafish spinal cord. With the help of voltage imaging, the relationship between the phases of membrane potential oscillations in glutamatergic interneurons in different positions along the zebrafish spinal cord can be visualized. **(a)** Selected cells from Fig. 17b that illustrate the fact that cells on the same side of the spinal cord are in phase, while cells on opposite sides of the spinal cord are antiphase, meaning phase-shifted by 180°. **(b)** Cells 30 and 31 are on the same side of the spinal cord and thus in phase. **(c)** Cells 27 and 29 are on opposite sides of the spinal cord and thus phase-shifted by 180°.

3.2 Establishing All-Optical Electrophysiology in Zebrafish

Voltage imaging in zebrafish has not been combined with optogenetics as of yet. This study aims to combine optogenetics with voltage imaging in zebrafish to establish all-optical electrophysiology. The experiments that combine voltage imaging with optogenetics in this report are performed with zebrafish larvae that have been injected with constructs for transient expression in the embryonic stage, unless stated otherwise. Different constructs have been tested and are summarized in Fig. 19a.

3.2.1 Initial Injections

The first series of tested injections all made use of the UAS-Gal4 system, where a parent fish carries the Gal4 driver and the offspring is injected with a plasmid that contains the Gal4-activated UAS

promoter to drive expression of target constructs. Four different types of injections were tested. In all constructs, the channelrhodopsin CoChR was soma-localized using the Kv2.1 potassium channel soma-targeting sequence. The first set of tested injections consisted of injecting only the channelrhodopsin CoChR into a transgenic zebrafish line that already expressed the voltage indicator zArchon under a glutamatergic promoter. Co-localization of construct expression was bad with these injections meaning that cells which expressed both the channelrhodopsin and the voltage indicator were rare. Furthermore, expression was weak. During the second round of tested injections, two separate plasmids carrying CoChR and zArchon respectively were injected into embryos of a zebrafish line that expressed Gal4 panneuronally under the *HuC* promoter. Co-localization was better in this case since plasmids often seem to get taken up simultaneously into cells; however expression was still sparse and cells with sufficient expression for all-optical electrophysiology experiments were hard to find. To further improve co-localization, the third round of injections involved a plasmid using the Gal4-activated *UAS* promoter to drive both the expression of zArchon and CoChR. The two proteins were coupled via a T2A linker sequence that degrades upon translation. Expression remained weak. It was initially hypothesized that the *UAS* promoter is not strong enough to drive sufficient expression after injections for transient expression. Therefore, in a fourth set of tested injections, the panneuronal *HuC* promoter was used to drive expression of the double construct with the linker sequence. This construct (*HuC:zArchon-GFP-T2A-CoChR-mOrange-Kv2.1*) exhibited better expression levels (Fig. 19b-e) and was used in most of the all-optical electrophysiology experiments presented in this study. Later on, however, injection of a *UAS*-driven construct yielded good expression levels (see section 3.6.1). Thus it could be that there was a problem with the specific version of the *UAS* promoter that was employed in the plasmids during the first three injection types. The constructs were all cloned using the same template.

The fourth construct employing the *HuC* promoter had the best expression levels; however despite using a 'panneuronal' promoter, not all neurons expressed the desired constructs after injections for transient expression. In effect, a random subset of all neurons expressed the desired proteins using this construct.

a

	Parent Fish	Injection	Co-localization	Expression
1	vglut2a:Gal4; UAS:zArchon-GFP in-cross	UAS:**CoChR**-mOrange-Kv2.1	bad	sparse & weak
2	HuC:Gal4 x Nac	UAS:**CoChR**-mOrange-Kv2.1 **&** UAS:**zArchon**-GFP	good	sparse & weak
3	HuC:Gal4 x Nac	UAS:**zArchon**-GFP-T2A-**CoChR**-mOrange-Kv2.1	good	sparse & weak
4	Nac in-cross *OR* vglut2a:Gal4; UAS:zArchon-GFP in-cross	HuC:**zArchon**-GFP-T2A-**CoChR**-mOrange-Kv2.1	good	good

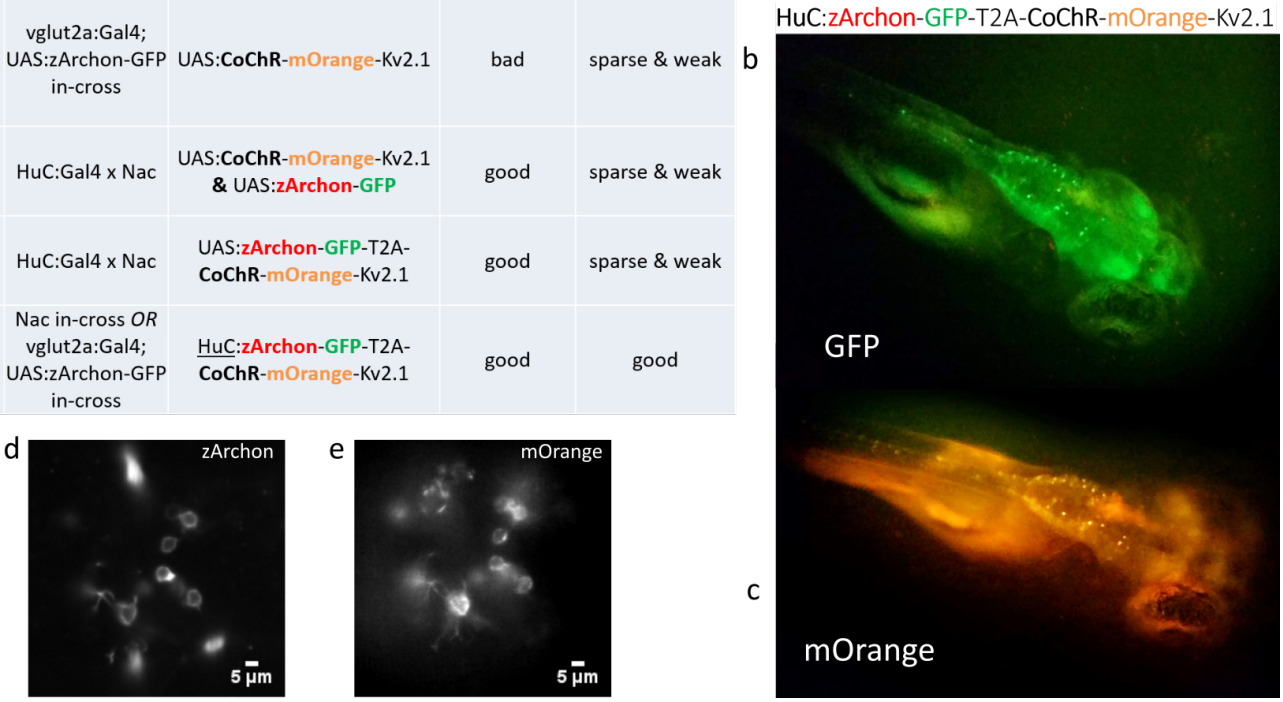

Figure 19: Establishing all-optical electrophysiology in zebrafish (a) 1-3: Summary of the first tested injections that suffered from sparse and weak expression as well as bad co-localization. Good co-localization means that the same subset of cells express both CoChR and zArchon so that the cell can be stimulated and imaged. See text for more details regarding the initial constructs. **4:** Improved construct using panneuronal promoter *HuC* with good co-localization as well as expression. **(b)** Expression of GFP marking zArchon in a zebrafish homozygous *nacre* larva that was injected with construct 4 (excitation of GFP at 488 nm) **(c)** Expression of mOrange marking CoChR in the same larva (excitation of mOrange at 532 nm). **(d)** A subset of cells in the larval zebrafish hindbrain (larva of same genotype as in b and c) expressing zArchon (excitation of zArchon at 637 nm). **(e)** The same subset of cells as in d also expression mOrange marking CoChR.

3.3 1P vs 2P Stimulation of Channelrhodopsin

Construct 4 in Fig. 19a was injected into *nacre* zebrafish embryos for the experiments presented in this section. The aim was to test different excitation techniques to achieve reliable stimulation of the channelrhodopsin CoChR. The tested excitation methods included one photon (1P) light sheet excitation, two-photon (2P) scanning excitation and 1P widefield excitation. In this section, excitation using 1P light sheet and 2P scanning are compared. All experiments in this section used red light at 637 nm and 66 $\frac{W}{mm^2}$ to excite the voltage indicator zArchon.

In Fig. 20, the same cell was excited using light sheet 1P blue light excitation (Fig. 20b) and then 2P scanning excitation (Fig. 20c). In the 2P excitation case, a circle was scanned around the cell membrane. The completion of one circle took 2 ms, so full circles were scanned at 500 Hz. In both stimulation cases, the light intensity or power was increased with 10 Hz steps and 50 % duty cycle (DC). 1P excitation elicited APs in the cell. The maximum number of APs per stimulation interval is reached for powers between 2.5 - 5 $\frac{mW}{mm^2}$. After that, one spike less is elicited per stimulation interval. This can likely be attributed to the channelrhodopsin inactivation dynamics. Some of the channelrhodopsin population falls into an inactive non-conducting state after a while so that the conductance decreases after the initial conductance burst, reaching a steady state, slightly lower conductance. 2P scanning excitation was less efficient at elicitng APs (Fig. 20c). Only one spike was triggered per stimulation interval towards the end of the trial, while 3 were triggered using blue light excitation. This is unlikely due to a lack of power in the 2P scanning case since the power used was in the range of 12-18 mW, and thus not very low.

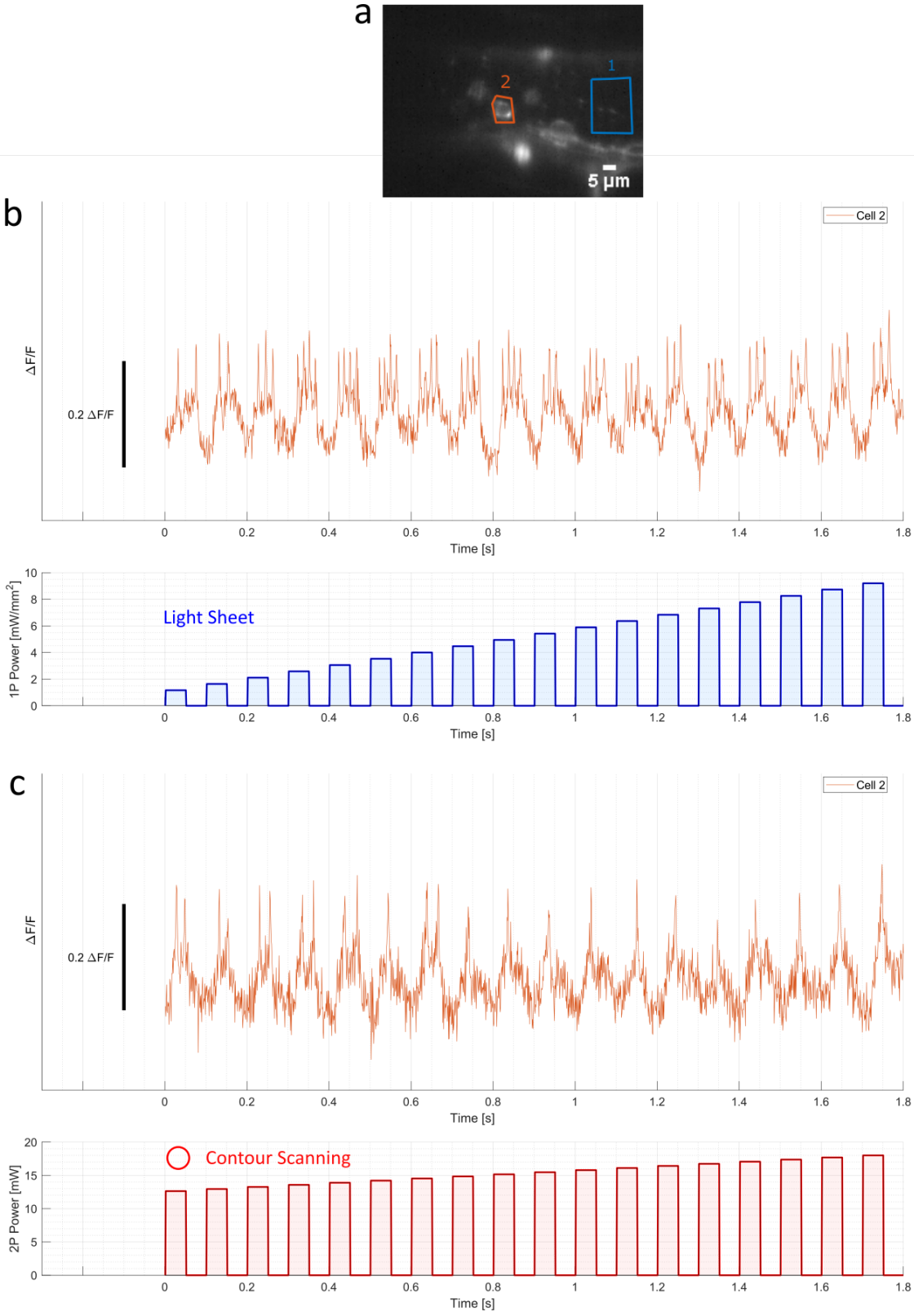

Figure 20: Comparison of channelrhodopsin stimulation using 1P and 2P excitation. This experiment was conducted in a *nacre* larva that was injected with construct 4. **(a)** Mean zArchon fluorescence during trial shown in **b**; '2' marks the cell of interest and '1' marks the region that was used for background correction. **(b)** Top: $\frac{\Delta F}{F}$ trace representing membrane voltage dynamics during 10 Hz stimulation (50% duty cycle) of the cell using 1P light-sheet excitation at 488 nm. Bottom: The blue light intensity was stepped from 0.22 to 9.2 $\frac{mW}{mm^2}$. **(c)** The same cell as in **b** is excited with 2P light by scanning a circle around the cell membrane. The 2P power was stepped from 12 to 18 mW; the stimulation was also at 10 Hz and 50% duty cycle. More APs can be observed during 1P stimulation.

As a next step, single-cell excitation using 2P excitation was tested (Fig. 21). A single cell was

activated using 2P contour scanning of the target cell membrane. Fig. 21b shows that single-cell targeting was successful since only the targeted cell shows a modulation of membrane potential dynamics linked to the stimulation waveform. However, only sub-threshold depolarization was achieved in this case and 2P stimulation was not able to elicit APs.

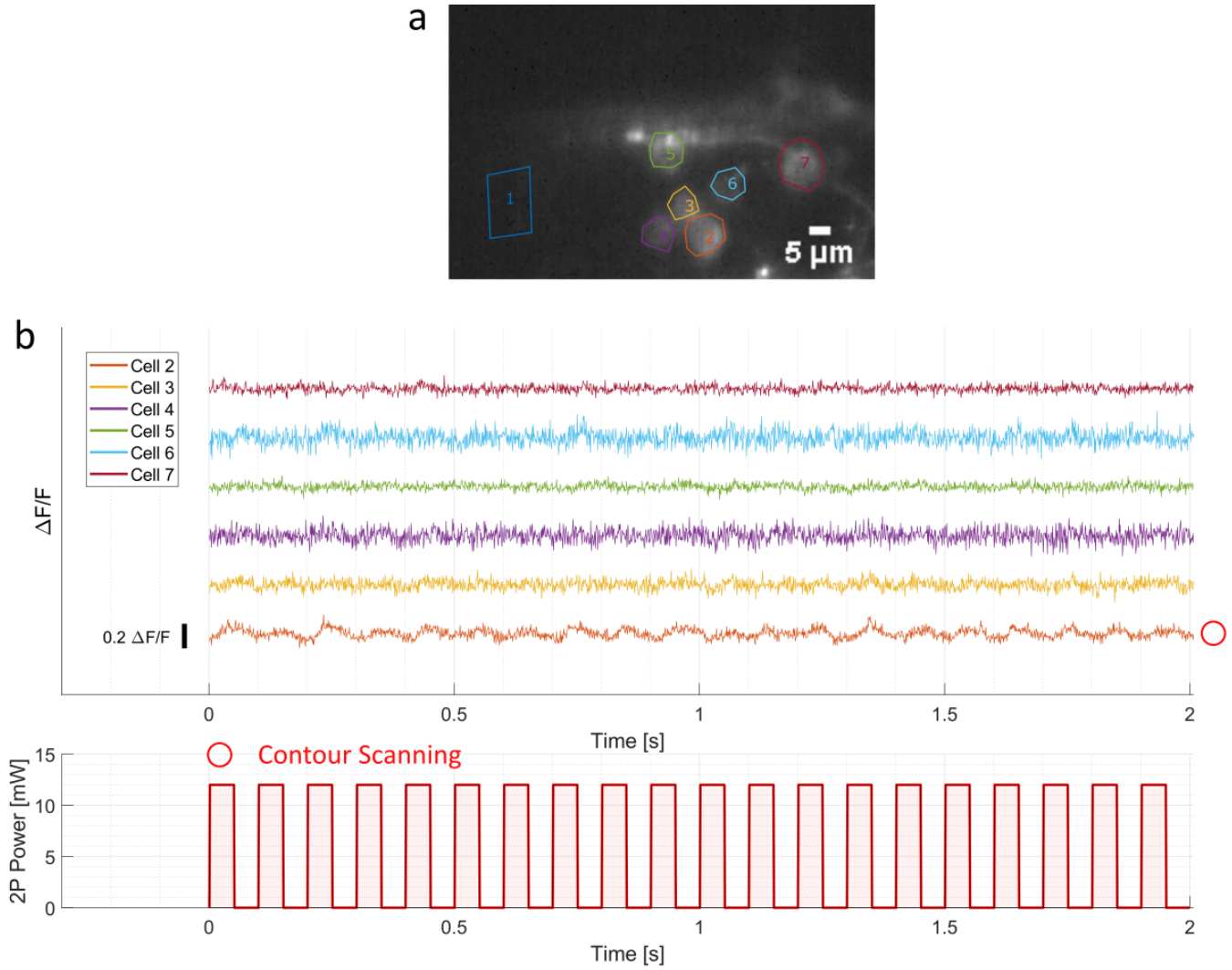

Figure 21: Single cell targeting using 2P excitation. This data was obtained in a *nacre* larva injected with construct 4. **(a)** Average zArchon channel fluorescence image. Only cell 2 (bottom) is excited using 2P cell contour scanning. **(b)** Fluorescence traces showing that only cell 2 exhibits membrane potential potential dynamics that are modulated by the 2P excitation light, thus indicating that single-cell targeting was successful. The cell was stimulated at 10 Hz, 50% DC at a constant power of 12 mW.

2P scanning excitation was not producing the desired stimulation efficiency. It was hypothesized that changing the scanning pattern could improve stimulation efficiency. A spiral pattern was tested instead of scanning the cell contour. The idea was that the 2P point spread function has a certain extent in the axial direction and thus a spiral scanning pattern could potentially hit more parts of the cell membrane in the focal volume compared to contour scanning. Spiral scanning was tested and compared to 1P light sheet excitation (Fig. 22). No spikes were elicited during 2P stimulation when it succeeded 1P stimulation (Fig. 22b). The stimulation intensity was stepped up throughout the trial for both the 1P and 2P stimulation case. No substantial difference was observed in the membrane potential depolarization during the last six 2P power levels in Fig. 22b. This indicates that more power is not increasing stimulation efficiency in this case. After a 5 minute recovery period, the trial was repeated with 2P stimulation preceding 1P stimulation (Fig. 22c). This time, an AP was elicited at the sixth power step (12 mW) during the 2P stimulation phase. This suggests that the cell is more susceptible to 'tiring out' and becoming non-responsive to excitation in the

2P stimulation case which seems to be less efficient overall at activating the cell. This 'tiring out' seems to be reversible, however, since an AP was elicited during 2P stimulation after a short recovery phase when it preceded 1P stimulation. The new spiral scanning pattern did not seem to improve 2P stimulation efficiency.

A final attempt was made to improve 2P stimulation efficiency using an axicon [94], [95] and an additional lens. The aim was to extend the 2P point spread function in the axial direction to form a line of excitation within the sample. The extent of the line of excitation was roughly 10 μm, corresponding approximately to the diameter of a neuron. Together with the spiral scanning pattern, the hope was that more channelrhodopsins on the cell membrane would be excited. However, using the axicon did not lead to observably better stimulation efficiency (results not shown).

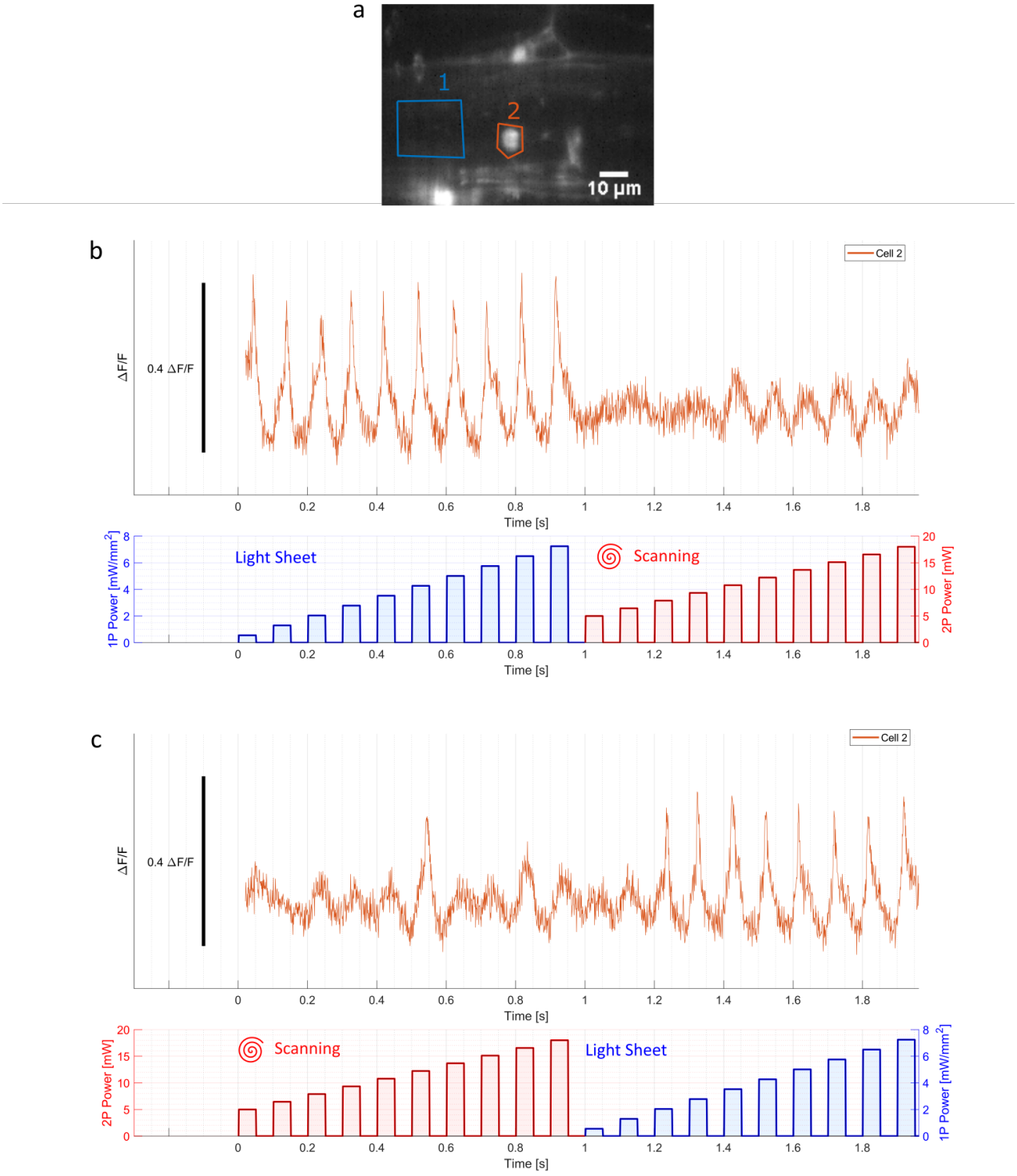

Figure 22: Single-trial comparison of 1P and 2P stimulation efficiency. Data was obtained in a *nacre* larva that was injected with construct 4. **(a)** Average zArchon channel fluorescence image of trial shown in **b**. The cell of interest ('2') that was stimulated in **b** and **c** is indicated. '1' indicates the background region that was used to calculate $\frac{\Delta F}{F}$ in the following panels. **(b)** The cell was first activated using 1P light sheet blue light excitation at 488 nm to stimulate CoChR at 10 Hz, 50% DC. Then the excitation was switched mid-trial to 2P stimulation at the same frequency using a spiral scanning pattern to target the cell. The blue light intensity was stepped from 0.55 to 7.24 $\frac{mW}{mm^2}$. The 2P power was stepped from 5 to 18 mW. $\frac{\Delta F}{F}$ fluorescence traces are shown. APs are only elicited during the 1P stimulation period in this case. **(c)** Another trial was acquired following the one in **b** after a short recovery period of 5 minutes. This time, the order of excitation was reversed. First, the cell was stimulated using 2P spiral scanning excitation, then the cell was activated with blue light sheet excitation. In this case, an AP was elicited during the 2P stimulation period. The intensity and power values are the same as in **b**. The APs that are elicited in these trials are unusually broad. This could either be a property of the cell type that was imaged or an indication that the cell was unhealthy, which could be a result of construct over-expression.

3.4 Widefield 1P Stimulation of Channelrhodopsin

A third way of stimulating the channelrhodopsin CoChR was tested using 1P widefield excitation. Widefield excitation was better compatible with a new, more powerful red laser that enabled voltage imaging with larger fields of view via light sheet excitation of the voltage indicator. For this technical reason, 1P widefield blue light excitation was the method of choice for CoChR stimulation in the following experiments (sections 3.5 and 3.6). Here, 1P widefield blue light stimulation is shown to be an efficient way of stimulating CoChR. In these experiments zArchon was imaged at 639 nm, 130 $\frac{W}{mm^2}$ with an exposure time of 1 ms.

Fig. 23b uses 1P widefield excitation to demonstrate that CoChR activation can have very different effects in different cells. In this trial, both cells of interest in the field of view were stimulated simultaneously at 1 Hz, 50% DC in the second half of the trial, while spontaneous activity was observed in the first half of the trial. Both cells are continuously active in the first half of the trial. A step ramp of blue light power (0.20 to 0.39 $\frac{mW}{mm^2}$) is used to activate the cells in the second half of the trial. The stimulation causes cell 3 (yellow) to increase its firing rate during the stimulation interval while it causes cell 2 (red) to stop firing. This potentially unexpected effect in cell 2 can be explained by a phenomenon called depolarization block [96]. During this phenomenon, the cell membrane remains constantly depolarized and is unable to repolarize and re-active voltage gated sodium channels which would be necessary to elicit further action potentials.

Fig. 23c demonstrates that single-cell targeting can be achieved using 1P widefield excitation. An iris is used on the widefield blue light path to target a single cell. Only cell 2 (red) is stimulated with blue light and exhibits the same depolarization block pattern as in the second half of the trial in Fig. 23b. Meanwhile, cell 3 (yellow) is spontaneously active with a firing pattern similar to the one it was displaying in the first half of Fig. 23b. This demonstrates that single-cell targeting can be achieved with widefield 1P excitation. However, this form of single-cell targeting works well only if CoChR expressing cells are sparse enough since the size of the smallest excitation spot that can be achieved in this way is much larger than the 2P point spread function.

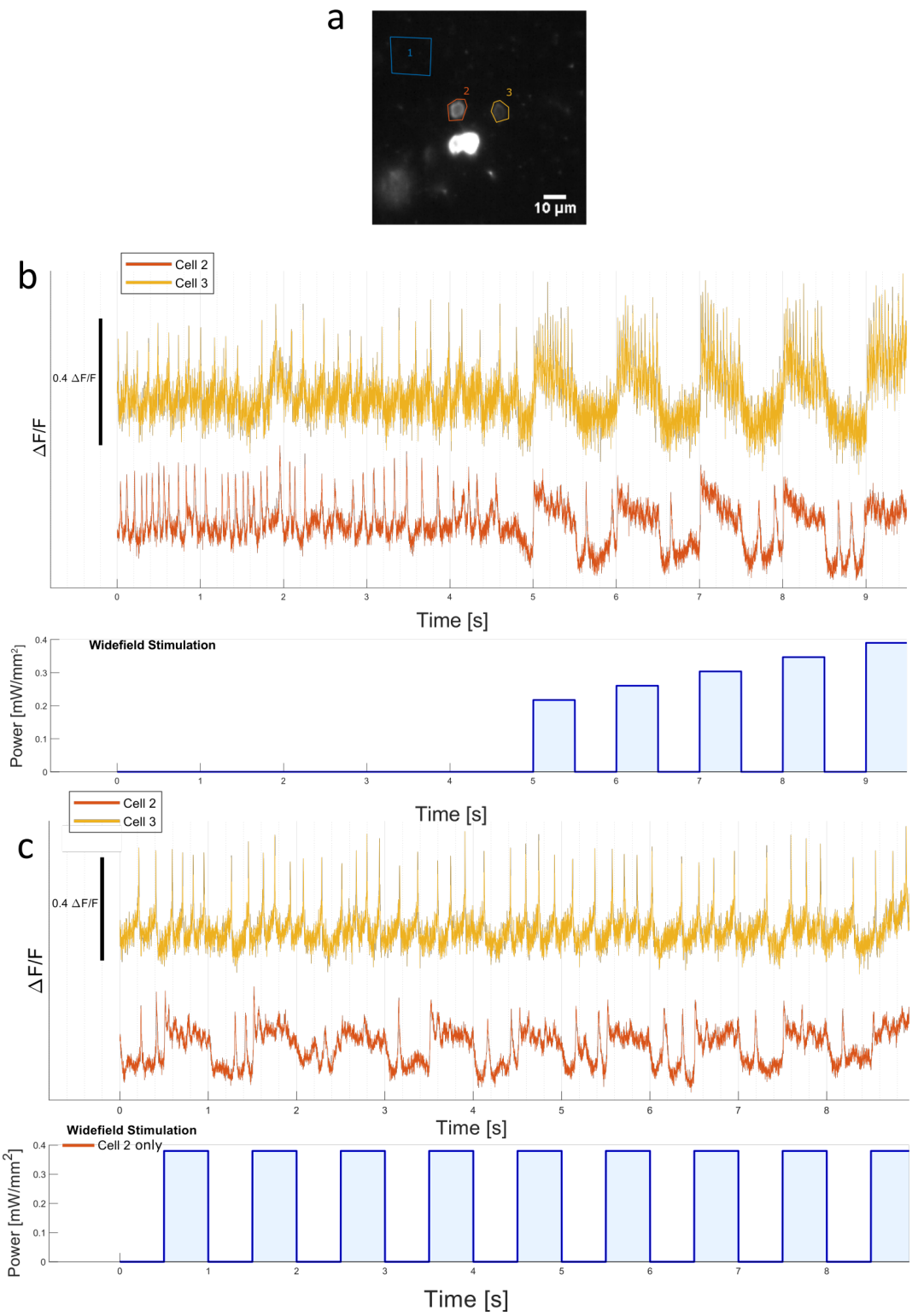

Figure 23: Widefield 1P blue light excitation of CoChR. This experiment was performed in a *nacre* larva that was injected with construct 4. Widefield blue light stimulation was used in this trial rather than light sheet excitation as in previous trials. **(a)** Average zArchon channel fluorescence of trial recorded in **b**. The two cells that were stimulated are indicated. The two very bright spots are cells that expressed the constructs in very large quantities and did not react to blue light stimulation. Potentially they were unhealthy as a result of these high expression levels. **(b)** In this trial, cells were spontaneously active for the first half of the trial and then stimulated with a 1 Hz, 50% DC blue light ramp for the second half. The intensity was stepped from 0.20 to 0.39 $\frac{mW}{mm^2}$. This trial illustrates that cells can react very differently to blue light stimulation. Cell 3 (yellow) increases its firing rate during blue light stimulation while cell 2 (red) stops firing. **(c)** In this trial, widefield blue light stimulation was delivered to cell 2 only. The cell was stimulated at a constant intensity of 0.39 $\frac{mW}{mm^2}$ at 1 Hz, 50% DC. Only the stimulated cell reacts to the stimulus, while the other cell exhibits the same spontaneous firing pattern as in the first half of the trial in **a**. This indicates that single cell targeting can be achieved with 1P widefield stimulation.

3.5 Mapping Functional Connectivity

This section aims to show that all-optical electrophysiology could be a very useful tool for functional connectivity mapping. While the results presented here cannot reveal a specific functional neuronal connection, they illustrate how functional connectivity mapping could potentially be achieved in future experiments. Some improvements could be made to the experimental protocol and are discussed in section 4.4.

The aim of this experiment was to reveal a functional connection by stimulating a single CoChR expressing cell while simultaneously imaging many potential postsynaptic candidates that express the voltage indicator zArchon only. The idea was to elicit spikes in the targeted cell and then calculate spike-triggered average traces in the postsynaptic candidate cells to reveal a potential excitatory or inhibitory postsynaptic response which would suggest a functional connection between the targeted cell and the responsive postsynaptic cell.

The experiment was performed in a *vglut2a:Gal4;UAS:zArchon-GFP* zebrafish larva that was injected with construct 4, meaning that a random subset of neurons expressed both the voltage indicator and the channelrhodopsin and many glutamatergic cells expressed only the voltage indicator zArchon. The stimulated cell could be excitatory or inhibitory, since it expressed CoChR which comes from the injection using a panneuronal promoter. Therefore, both excitatory or inhibitory postsynaptic potentials could be observed. Observing an inhibitory postsynaptic potential is less likely due to the fact that the inhibitory reversal potential is closer to the resting membrane potential. The imaged postsynaptic candidates are glutamatergic only and thus excitatory. Fig. 24b shows the target cell (number 9) that was receiving 1P wide-field blue light stimulation at 0.8 $\frac{mW}{mm^2}$, 10 Hz and 50% DC as well as the area that was targeted with blue light. The voltage indicator zArchon was stimulated at 639 nm and 130 $\frac{W}{mm^2}$ with light sheet excitation. The exposure time was 1 ms. Fig. 24c shows an extract of the $\frac{\Delta F}{F}$ fluorescence traces that were acquired. One can observe that only the stimulated cell 9 exhibits spiking activity. An interesting phenomenon which does not seem to be related to stimulation of cell 9 can be observed in cells 6 and 7: cell 6 seems to depolarize while cell 7 seems to simultaneously hyperpolarize. Since both cell are glutamatergic, cell 6 cannot be inhibiting cell 7. Thus they are likely receiving simultaneous inhibitory and excitatory input which may have a common cause further upstream in the circuit.

To identify possible postsynaptic excitatory or inhibitory potentials, spike-triggered averages were calculated (Fig. 25a). For every time point when a spike occurred in the triggered cell 9, a window of 100 ms was extracted from the $\frac{\Delta F}{F}$ fluorescence traces in all cells. These windows were then averaged. No obvious excitatory or inhibitory postsynaptic potential could be identified. Cells 10 - 13 exhibit an increase in fluorescence around the triggering time point. Theoretically, electrical connectivity in the form of gap junctions between cell 9 and cells 10 - 13 could lead to traces similar to the ones observed. However, since cells 10 - 13 were within the blue light stimulation area, it is more likely that the increase in fluorescence signal is due to the GFP-tag on zArchon in these cells which causes fluorescence that bleeds into the zArchon imaging channel. The ROI of cell 12, which is right next to cell 9, could additionally be capturing some photons from cell 9 fluorescence since the cell 12 trace looks like a noisy and scaled version of the spike in cell 9. Unfortunately, no bleed-through measurement was acquired during this experiment. Blue-light triggered averages were calculated to gain more insights concerning the potential bleed-through in cells 10, 11 and 13 (Fig. 25c). Cells 10, 11 and 13 exhibit a sharp rise in signal when the blue light turns on in the middle of the trace and display a continuously increased signal for the period of the blue light stimulation. This would be in line with the hypothesis that the signal increase in these cells is due to bleed-through. For future experiments, it would be better to target the blue light to a single cell, even if CoChR expression is sparse like in this case.

Fig. 25b shows a spike-triggered activity map that was obtained by calculating a spike-triggered movie of the whole field of view. The absolute value of the spike triggered movie was averaged to yield the activity map. Bright spots could mark activity that is temporally locked to the spike in

cell 9. Cell 9 is the bright spot in the middle of the image and is marked by a white arrow. Some of the other bright spots (yellow arrows) correspond to blood flow. No clear activity locked to the spike in cell 9 is detected in other cells.

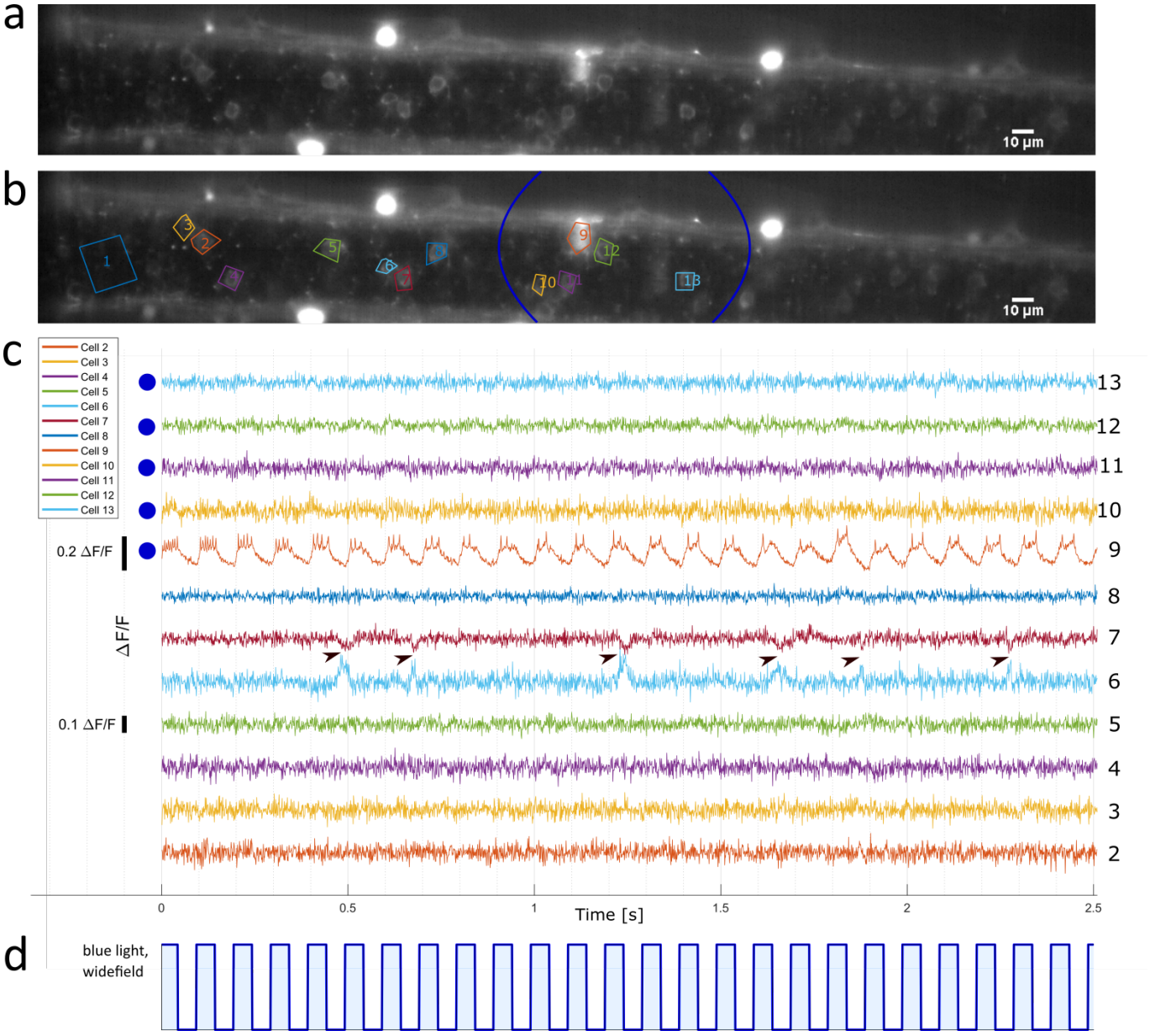

Figure 24: Functional connectivity mapping using all-optical electrophysiology. This experiment was performed in a *vglut2a:Gal4;UAS:zArchon-GFP* larva that was injected with construct 4. The aim was to find cells that were functionally connected by stimulating a single cell (containing channelrhodopsin) and checking for postsynaptic responses in the surrounding cells. **(a)** Image of average zArchon fluorescence over trial. **(b)** Average zArchon fluorescence including cell ROIs that were analyzed in subsequent panels. Only cell 9 (middle top) expressed both the channelrhodopsin and the voltage indicator. The other cells expressed only the voltage indicator zArchon. The blue circle indicates the area that was stimulated with blue light. **(c)** Cell 9 was stimulated with widefield blue light at 0.8 $\frac{mW}{mm^2}$, 10 Hz and 50% DC. APs are elicited during blue light stimulation. Cells 10-13 were also within the stimulation area, but did not express the channelrhodopsin. Black arrows mark an interesting relationship between the voltage dynamics in cells 6 and 7 that seems to be unrelated to the stimulation. Cell 6 depolarizes while cell 7 hyperpolarizes. This seems to indicate that cell 6 receives excitatory input while cell 7 simultaneously receives inhibitory input. **(d)** Widefield blue light stimulation waveform.

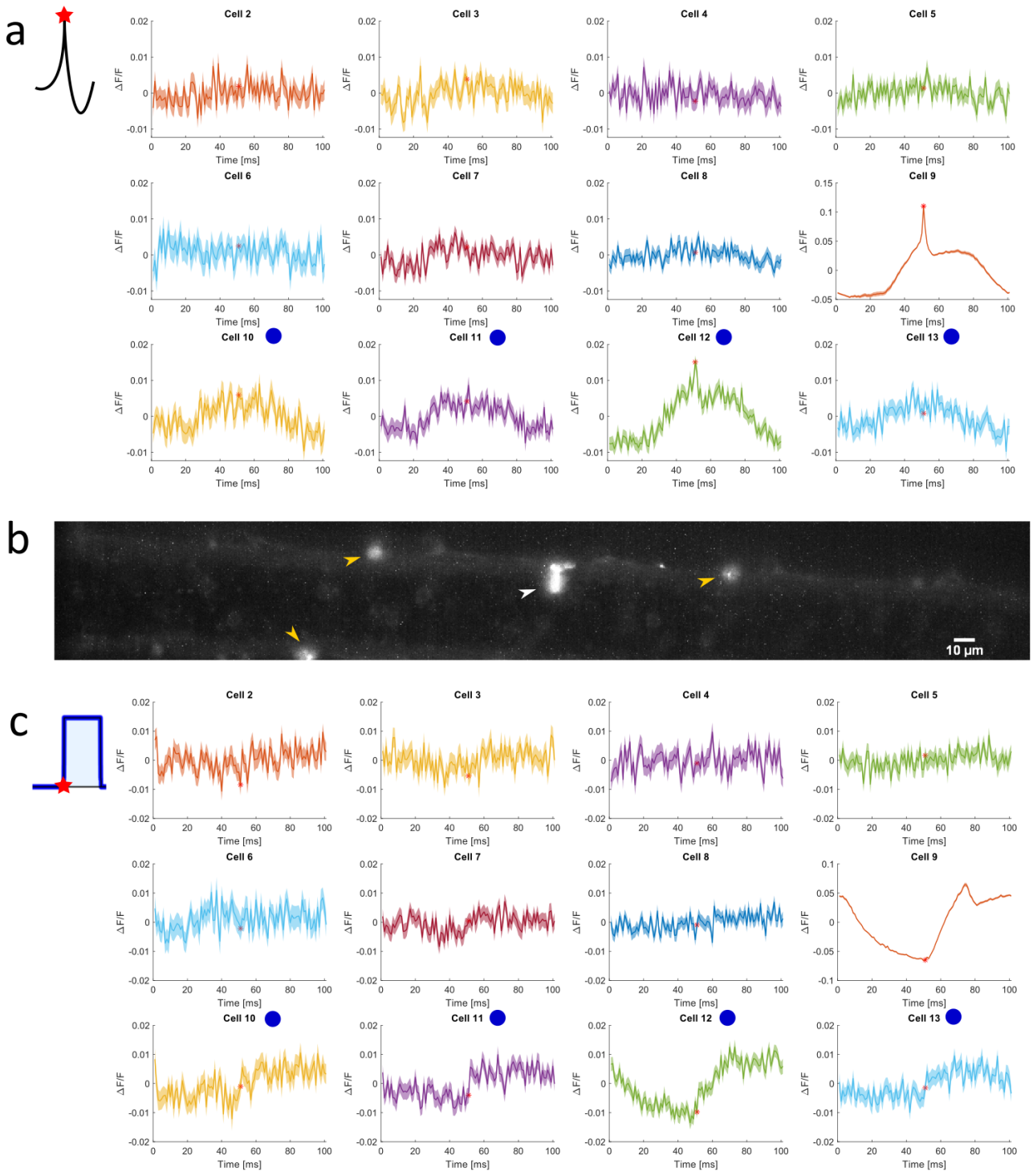

Figure 25: Spike-triggered and blue light stimulus-triggered averages. This analysis is based on the data that is visualized in Fig. 24 where cell 9 is stimulated and possible postsynaptic cells are imaged. **(a)** In order to identify potential functional connectivity between the stimulated cell 9 and postsynaptic candidates, spike-triggered averages were calculated. A window was extracted in all cells for each time point where a spike occurred in cell 9 and the windows were then averaged for each cell to yield spike-triggered averages. The triggering point is marked by a red star. The AP waveform can be seen in the triggering cell 9. Cells 10-13 exhibit a seeming increase in fluorescence around the triggering point. However, this is likely an artifact linked to the fact that these cells were within the blue light stimulation area. **(b)** A spike-triggered movie was extracted where the whole field of view was averaged in a window of 100 ms around the spikes in cell 9. The absolute value of all frames was averaged to yield an activity map that could reveal neuronal activity locked to the spike in cell 9. Cell 9 is visible as a bright spot in the middle of the image (white arrow). No obvious neuronal activity linked to the spike in cell 9 was detected. Some other bright spots on the image are related to blood flow (yellow arrows). **(c)** Blue light stimulus triggered averages. The red star in the middle of the trace marks the turning on of blue light. Cells 10 - 13 show a sharp blue light stimulus triggered increase in signal. This would be in line with the hypothesis that this signal could be due to bleed-through of the GFP tag on zArchon in these cells into the imaging channel.

3.6 E/I Balance

An all-optical approach to quantify excitatory and inhibitory synaptic inputs to a neuron is proposed here. It was suggested in section 1.7.3 that a simultaneous measurement of the membrane potential time course and the neuronal membrane time constant can be used to quantify the excitatory and inhibitory conductances to a cell. The following shows how this could be achieved using all-optical electrophysiology in larval zebrafish. The aim was to reveal differences in the ratio of excitatory and inhibitory synaptic inputs to glutamatergic ventral medial (VeMe) interneurons in the case where the larva was swimming compared to the case where it was not swimming. VeMe cells display spiking activity mainly during swimming. We hypothesized that this could be due to an increase of excitation to the cell during swimming, or a decrease of inhibition. While the former would lead to an increased total cell conductance during swimming, the latter would lead to a decrease of cell conductance. Using the fact that the cell conductance is inversely proportional to the membrane time constant, we would expect a decreased membrane time constant in the case of increased excitation during swimming, and an increased membrane time constant during the case of decreased inhibition during swimming. We assumed that an increase of excitation to VeMe cells during swimming would be more likely and thus expected to see decreased time constants during swimming compared to rest. The present work is not able to reveal a difference in the membrane time constant during swimming versus no swimming, or the total conductance and ratio of excitatory to inhibitory conductances which can be derived from it. There are several possible explanations which are discussed in 4.5.1; however the basic approach remains valid and with some optimization it could be used to reveal differences in conductance dynamics in similar cases in the future.

3.6.1 Optogenetic Stimulation During Zebrafish Swimming

In order to measure the membrane time constant τ, optogenetic blue light stimuli (488 nm) were delivered at 10 Hz, 50% DC and 0.38 $\frac{mW}{mm^2}$ using widefield excitation. Optogenetic stimulation at 10 Hz and 50% DC causes a 50 ms membrane voltage depolarization phase, followed by a 50 ms decay phase during which the membrane potential falls back to the level it was at before optogenetic stimulation. The idea was to extract the membrane time constant τ from the decay phase, since τ dictates the decay dynamics which depend on the capacitance and total conductance of the cell. The membrane time constant is not the only influence on decay dynamics since the channelrhodopsin off-time constant also influences decay; this limitation is discussed in section 4.5.1.

This experiment was performed in a *vglut2a:Gal4;UAS:zArchon-GFP* larva that was injected with a *UAS:zArchon-GFP-T2A-CoChR-mOrange-Kv2.1* construct. This driver line was chosen since it expresses Gal4 in glutamatergic cells, so that construct expression is only driven in those cells. Two ventral medial (VeMe) cells were identified (Fig. 26a) and targeted with blue light simultaneously. The voltage indicator zArchon was excited with 639 nm red light at 70 $\frac{W}{mm^2}$ and exposure time was 2 ms. This is twice the exposure time and half of the red light intensity as compared to the experiment in Fig. 24 and Fig. 25 with the aim of being able to record for longer periods of time. Fig. 26b shows the fluorescence traces that were obtained from both cells. The raw fluorescence signal was high-pass filtered to remove photobleaching. The green indicator in Fig. 26b is the optomotor response (OMR) signal that induces the larva to swim. The OMR signal is a moving grating below the fish. The fish wants to keep up with the movement and thus starts swimming. The blue signal marks when the fish was swimming. One can observe that the fish starts swimming shortly after the OMR signal starts. Most APs in cells 1 and 2 occur during swimming. The fish's swimming activity was measured via a ventral nerve root (VNR) electrode that was inserted into the side of the fish. Swimming involves muscle contractions in alternating sides of the spinal cord. The VNR electrode records motoneuron activity related to the fish's swimming activity from one side of the spinal cord. Fig. 26c shows the raw VNR voltage signal, which is very noisy. The standard deviation was calculated (Fig. 26d), which is a more robust measure of motoneuron activity. A swim 'burst'

occurs when the standard deviation of the VNR voltage signal exceeds a certain threshold, which corresponds to motoneuron activity and a muscle contraction on one side of the spinal cord. Bursts are marked with black dots in Fig. 26d; the first burst in a swim bout is marked in green and the last one is red. The frequency of swimming can be calculated by counting how many times muscles on the same side of the spinal cord contract per unit of time. The swimming frequency is shown in Fig. 26e and is between 20 - 30 Hz, which is in the expected range of larval swimming frequencies of 20 - 60 Hz [54].

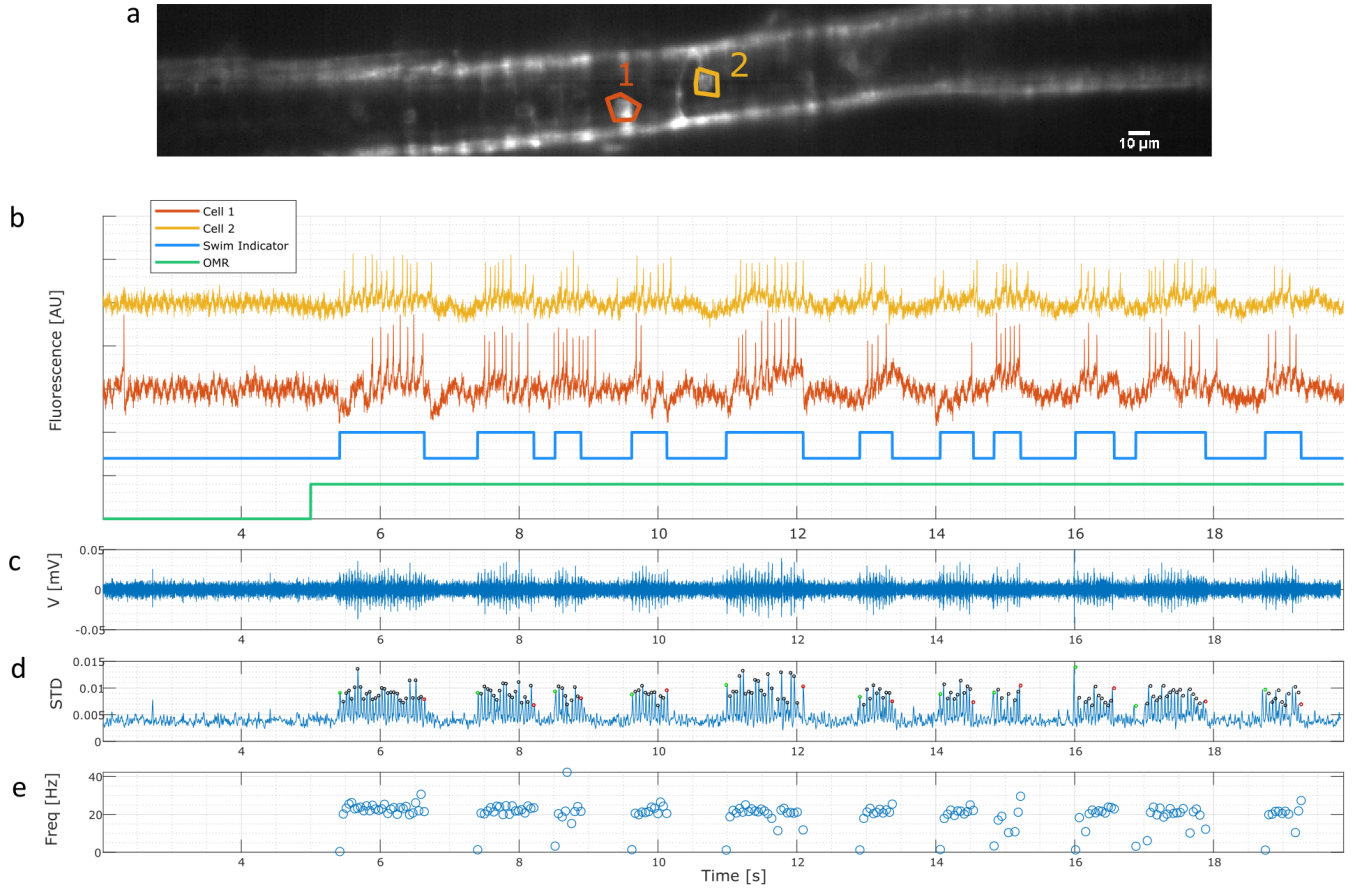

Figure 26: Ventral nerve root (VNR) recording and voltage imaging reveal neuronal activity related to swimming in the zebrafish spinal cord. This experiment was conducted in a *vglut2a:Gal4;UAS:zArchon-GFP* larva that was injected with a *UAS:zArchon-GFP-T2A-CoChR-mOrange-Kv2.1* construct. Thus only glutamatergic cells expressed the voltage indicator and the channelrhodopsin. **(a)** Average fluorescence image of zArchon in the zebrafish spinal cord and cells of interest for the subsequent analysis. **(b)** Cells were stimulated at 10 Hz, 50% DC and 0.38 $\frac{mW}{mm^2}$; stimulation waveform not shown. Fluorescence traces from two cells during swimming in the zebrafish spinal cord are shown. Traces were high-pass filtered to remove photobleaching. The blue indicator marks when the fish is swimming based on the standard deviation of the ventral nerve root (VNR) recording in **d** that measures motoneuron activity and thus muscle contractions on one side of the spinal cord. The green indicator marks when the optomotor response (OMR) signal turns on. The OMR signal is a moving grating below the fish that can trigger swimming behavior in the zebrafish larva. One can observe that the onset of swimming activity described by the blue indicator is right after the begin of the OMR stimulation. **(c)** Raw voltage recording measured by the VNR electrode. **(d)** Standard deviation of the VNR voltage signal in **c**. **(e)** Swimming frequency, corresponding to the frequency of muscle contractions on the same side of the spinal cord which is calculated based on the signal in **d**.

3.6.2 Extracting the Membrane Time Constant

Four trials like the one represented in Fig. 26 were recorded from the same two cells with short breaks (max. 5 minutes) in between trials to save data. The same imaging conditions and 10 Hz blue light stimulation as described above were used in all four trials. The aim was to extract the membrane time constant based on membrane potential decay dynamics after optogenetic stimulation. To achieve this, blue light stimulus-triggered averages were calcualted based on trials where no spikes

occurred. Spike trials were excluded since spikes bias the decay dynamics of the membrane. Out of 708 recorded blue light cycles pooled across all trials, 511 had no spikes for cell 1 and 525 had no spikes for cell 2. Out of the no-spike trials, 140 occurred while the fish was swimming and 371 during rest for cell 1, while there were 149 during swimming and 376 during rest for cell 2. The larger proportion of no-spike trials during rest can be explained by the fact that cells are more likely to spike during swimming. The smaller amount of no-spike trials during swimming makes the time constant estimate during swimming less precise in comparison.

No-spike blue light cycles were extracted and demeaned for each cell and then averaged separately for swimming versus no-swimming to yield blue light stimulus-triggered averages (Fig. 27). The blue light cycles were extracted around each blue light trigger, meaning that the blue light turns on in the middle of the trial (black dot in Fig. 27). During the decay phase while the blue light is off, the blue light triggered average is lower during swimming compared to no-swimming. This could be due to the fact that spikes occur in some trials preceding no-spike trials while the fish is swimming. The afterhyperpolarization of spikes from preceding trials could explain this. In section 4.5.1, an improved analysis technique is proposed that could avoid this potential bias.

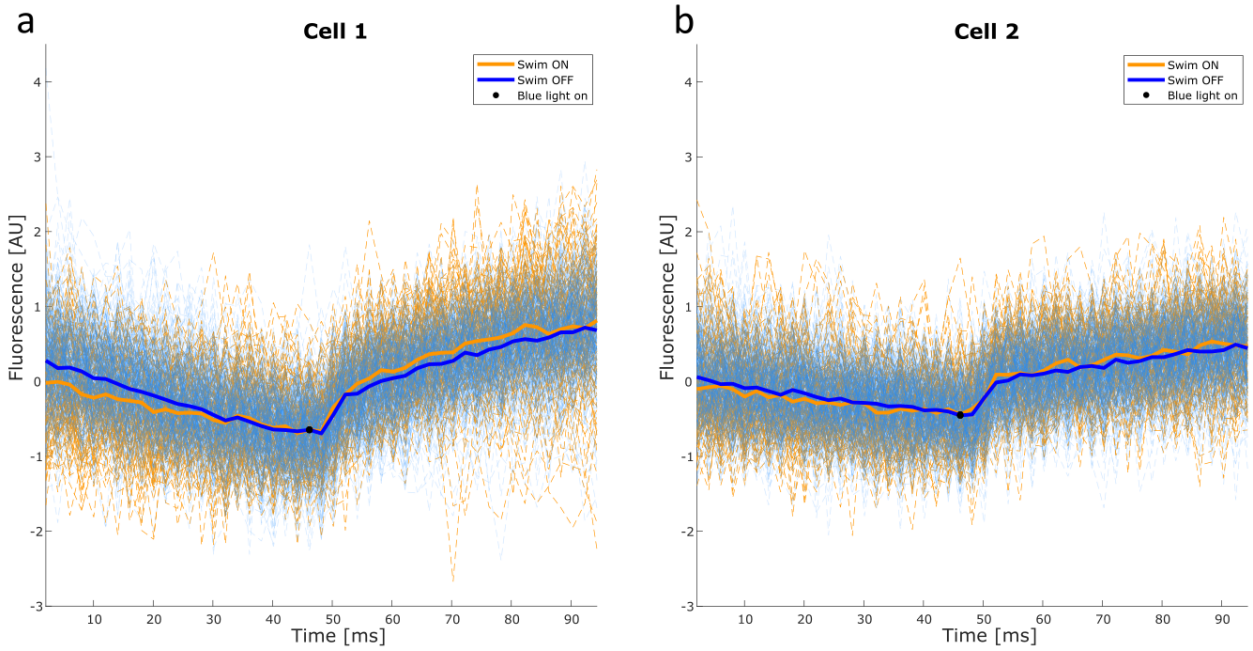

Figure 27: Blue light stimulus-triggered average traces. Blue light cycles during which no spikes occurred were selected, demeaned and averaged separately for cycles that occurred while the fish was swimming (orange) and while it was not swimming (blue). Blue light stimulus triggered averages are represented in **(a)** for cell 1 and **(b)** for cell 2. The blue light turns on in the middle of the window and is marked by a black dot.

The membrane time constant τ was extracted by assuming exponential decay dynamics in the first half of the blue light triggered cycle while the blue light is off. Blue-light-triggered traces were normalized to an interval between zero and one. The membrane time constant was estimated via the slope at zero of the normalized blue-light-triggered trace (Fig. 28). The estimated time constants for cell 1 during swimming on versus swimming off were $\tau_{on} = 34.6$ ms and $\tau_{off} = 36.2$ ms while they were $\tau_{on} = 36.0$ ms and $\tau_{off} = 37.0$ ms for cell 2 respectively. These results do not reveal an evident difference between the time constants in the swimming on versus off cases. Possible reasons are discussed in section 4.5.1.

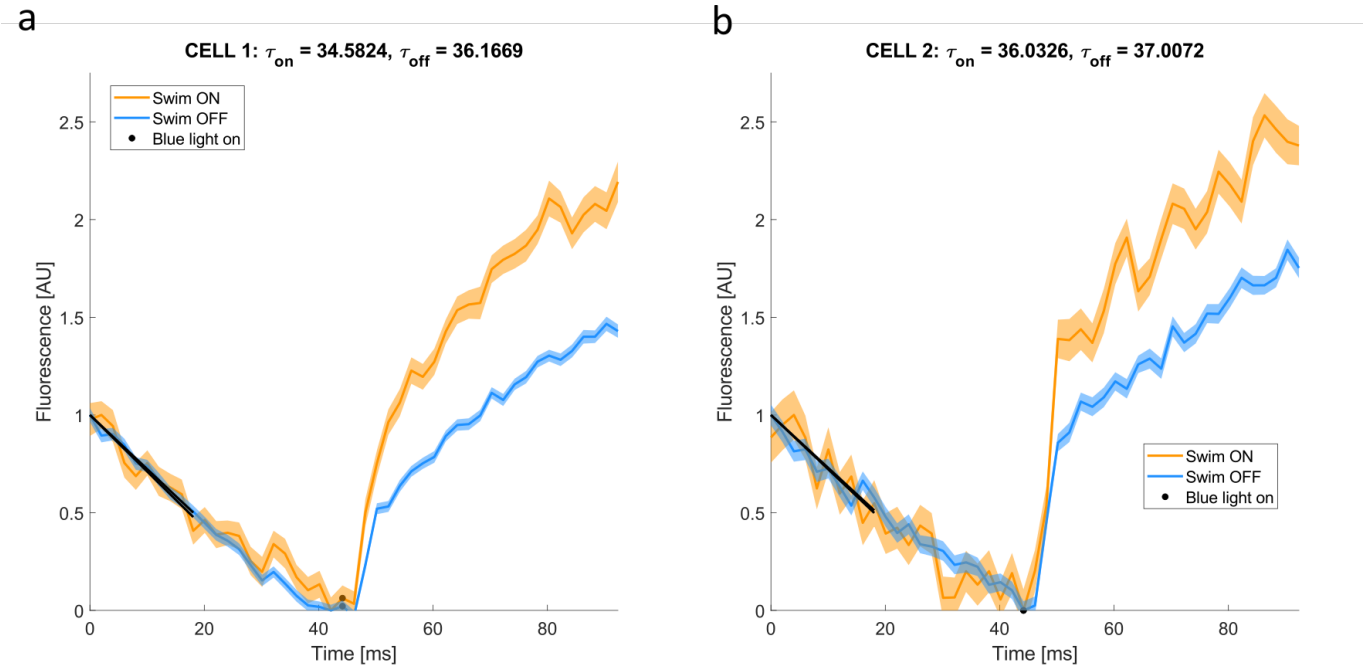

Figure 28: Estimation of membrane time constant. The membrane time constant is estimated via the slope at zero of the normalized blue light triggered average trace. The slope is extracted by fitting a linear model with offset 1 to the first 20 ms of the decay phase. Shaded areas represent the standard error of the mean (SEM). The time constants indicated on top of the graphs are in ms. No evident difference can be observed between the time constants for the swimming on versus the swimming off case.

3.6.3 Influence of Optogenetic Stimulation on Spiking Dynamics During Zebrafish Swimming

To examine the effect of blue light stimulation on VeMe cell spiking dynamics, spike histograms were calculated to show when spikes occur within the blue light cycle (Fig. 29). The spike histograms show that the blue light has an influence on the spiking dynamics. Spikes occur preferentially while the blue light is on in the second half of the blue light cycle. The U-shaped spike distribution in the blue light cycle that can be observed in the histogram comes from spikes that were triggered during the end of the blue light cycle when the cell was most depolarized. Some depolarization induced spikes can carry over into the beginning of the next blue light cycle. The effect of blue light is especially visible in Fig. 29d where a spike is triggered at the onset of blue light. Spiking activity of VeMe cells usually occurs during swimming, therefore it may seem odd that the histogram indicates the firing of some spikes during blue light OFF and swimming OFF. This could be explained by the fact that spikes occurring toward the beginning or end of a swim bout could be misclassified by our analysis pipeline as belonging to a swimming OFF trial.

Most spikes occur while the fish is swimming. Spike-triggered average waveforms were calculated for spikes elicited during swimming while blue light was on compared to while it was off (Fig. 30). This was achieved by extracting 100 ms windows around spikes, demeaning the trace in each window and averaging windows. The spike-triggered average waveform reveals that the baseline membrane potential is higher while the blue light is on. This is as expected since channelrhodopsin activation depolarizes the membrane. The effect of the voltage-gated potassium channels during the falling phase of the AP and during the afterhyperpolarization is more clearly visible in the blue light ON spike-triggered average waveforms. This is because the more depolarized membrane potential in the blue light ON case is further away from the potassium reversal potential than the resting membrane potential in the blue light OFF case.

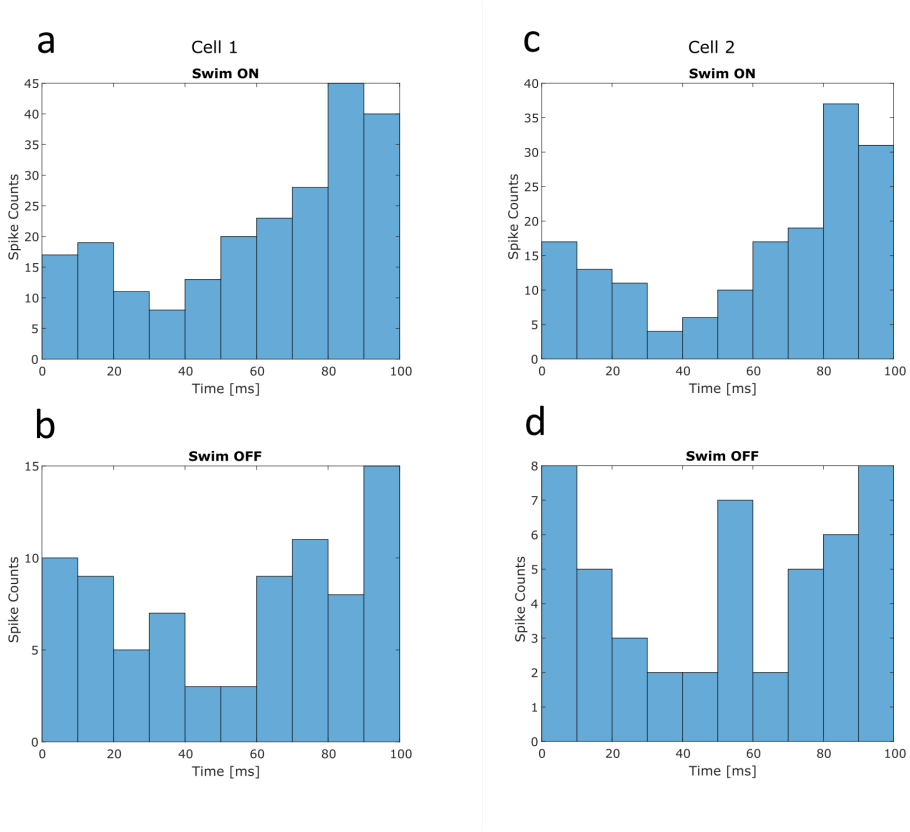

Figure 29: Histogram of spike distribution within blue light cycle. Spikes occur preferentially while the blue light is on in the second half of the blue light cycle (50 - 100 ms). The U-shaped distribution in the histogram likely comes from the fact that spikes are elicited towards the end of the blue light cycle when the cell is most depolarized. Spikes can also carry over into the beginning of the next blue light cycle, which is why many spikes occur right in the beginning of the cycle.

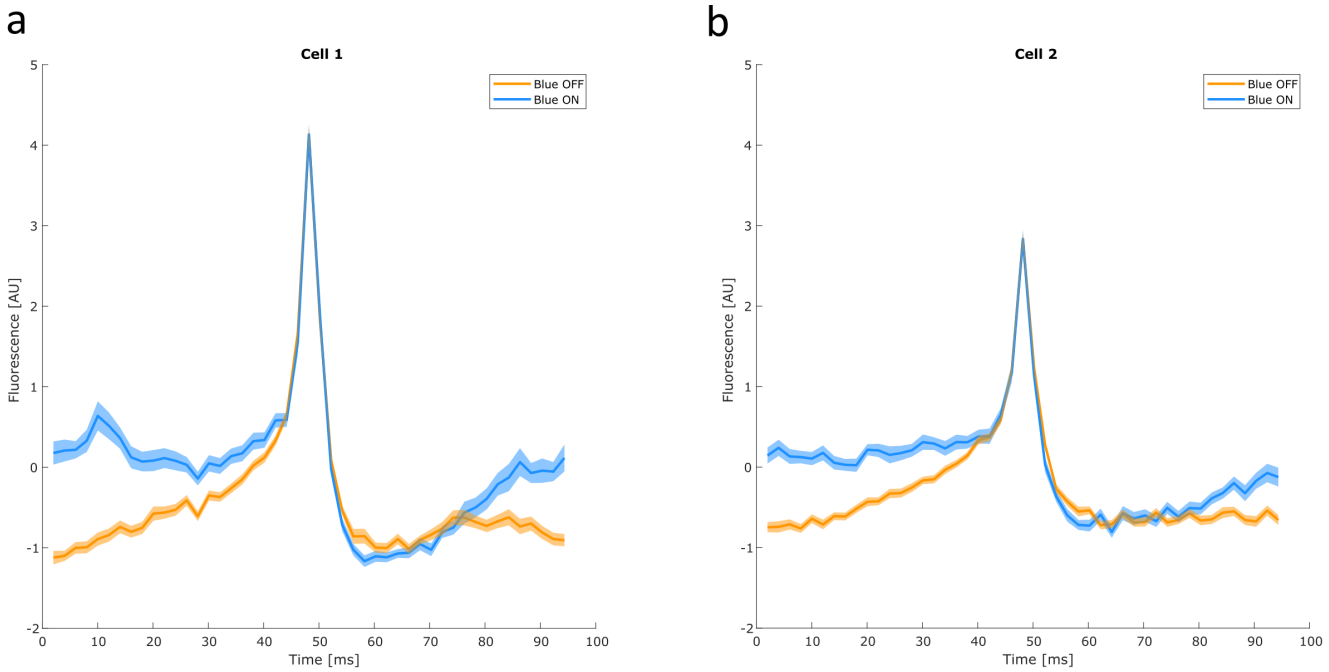

Figure 30: Spike-triggered average waveforms of spikes occurring during swimming for blue light OFF versus blue light ON. The resting membrane potential is higher in the case where the blue light is on since channelrhodopsin activation is depolarizing the membrane. The depolarized resting potential is further away from the potassium reversal potential, thus the effect of voltage-gated potassium channels during the falling phase of the AP as well as during the afterhyperpolarization is more visible. Cell 1 **(a)** seems to have a larger spike amplitude than cell 2 **(b)**. Spike-triggered average waveforms were calculated based on demeaned windows that were extracted around spikes from the high-pass filtered raw fluorescence trace. Since $\frac{\Delta F}{F}$ was not calculated in this case, it is harder to compare spike amplitudes. The difference could be a real effect or it could be due to lower expression of voltage indicator in cell 2.

3.7 Transgenic Zebrafish Line for All-Optical Electrophysiology

A transgenic zebrafish line with the necessary constructs for all-optical electrophysiology was established by injecting a *UAS:zArchon-GFP-T2A-CoChR-mOrange-Kv2.1* construct into *nacre* zebrafish embryos. The construct also contained a *cmlc2:GFP* marker that labels the heart. The heart marker was important since the transgenic line was established with a *UAS* promoter and without a Gal4 driver. Therefore only the heart marker will express in the transgenic line before it is out-crossed to a driver line and is useful to identify transgenics. Not including the driver is convenient since it offers flexibility with the possibility to cross to many different potential driver lines and thus drive expression in different cell types depending on the driver line.

To establish the transgenic line, a plasmid was created where the target construct was flanked by recognition sequences for the Tol2 transposase. Transposase mRNA was included in the injection solution. This led to the excision of the target construct from the injected plasmid and its integration into the zebrafish embryo genome. Initially, RNase contamination in the DNA plasmid solution - which was part of the injection solution - caused problems. The transposase mRNA was initially degraded before it was translated into transposase within the zebrafish embryo. Re-purification of the plasmid DNA solution and addition of a recombinant RNase inhibitor to the injection solution were able to solve the problem. To ensure that transgenesis was successful, an excision assay was performed (Fig. 31). The assay shows that transgenesis was successful for the examined embryos.

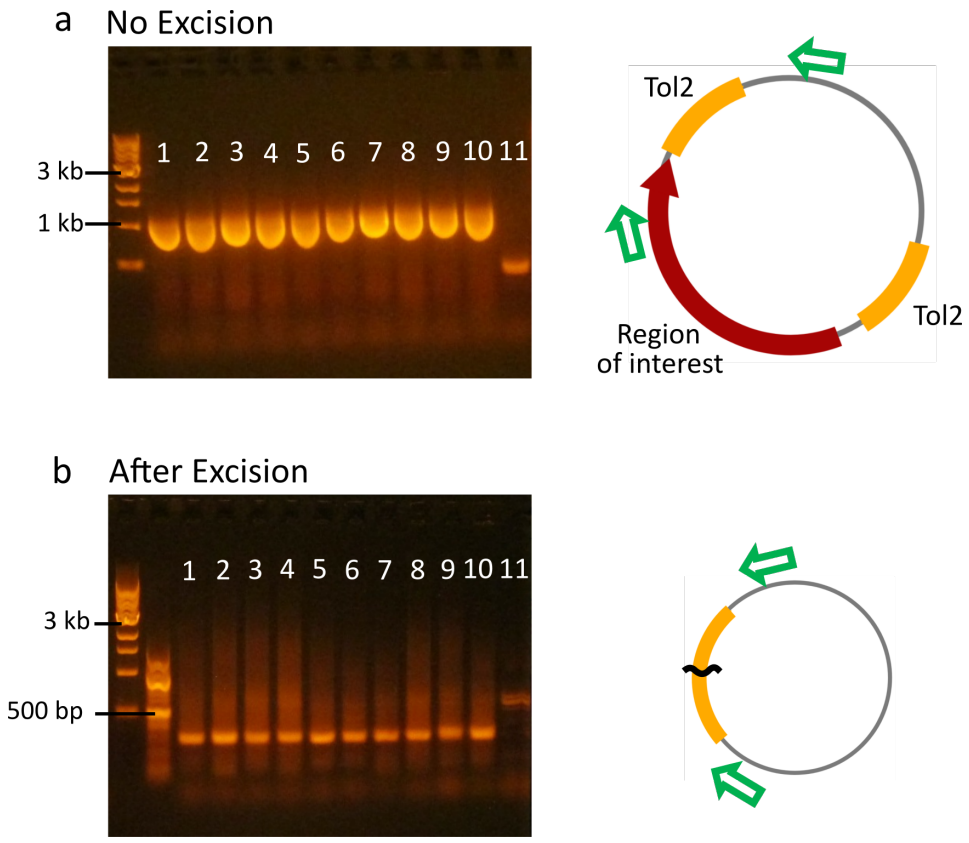

Figure 31: Excision assay to assess whether transgenesis was successful. The aim of the excision assay is to check whether the target construct was successfully excised from the donor plasmid. The assay is based on PCR amplification and is described in detail in [60]. The assay has two stages; the first stage checks for whole plasmids from which no region was excised and also serves as a control. The second stage checks for plasmids from which the target construct between the Tol2 flanking sequences has been removed. In both cases, primers are designed such that a PCR amplicon can only be detected in the situation which the assay tests for (no excision and excision respectively). **(a) No excision case.** This aims to check that the plasmid has been successfully injected into the embryo and also serves as a control for the excision assay in the second stage. PCR primers are designed such that one primer binds within the region of interest which would be excised in case of transgenesis and the other primer binds outside of this region on the other side of the Tol2 sequence. This is illustrated in the schematic on the right where primers are depicted as green arrows. Like this, the amplicon will only be generated if the region of interest is not excised and the plasmid is present. The expected band was 1153 bp. The gel on the left side shows the result for 10 tested embryos (lanes 1-10) and a control embryo that was not injected (lane 11). The expected band is visible for lanes 1-10. The band is very thick due to the large amount of template that was present. **(b) Excision case.** This assay tests for the presence of plasmids from which the target sequence was excised. The primers are located outside of the region of interest (see schematic). An amplicon is only created in case the excision was successful since the region to amplify would be too large if the region of interest is not excised and the PCR extension time was adapted to the shorter amplicon. A band between 321 - 671 bp is expected. The exact location of excision is unknown. The amplicon generated for the embryos in lanes 1-10 is around 350 bp and thus within the expected range. The control embryo in lane 11 only shows a single band which is in the same location as for the non-excision case. We concluded from these results that excision was successful in a subset of plasmids in all tested embryos.

Zebrafish embryos from injected batches for which this assay was successful were raised to the adult stage. The adult zebrafish were then screened for green hearts that mark the presence of the injected construct. Identified founder fish were crossed to a *vglut2a:Gal4;UAS:zArchon-GFP* driver line that would drive expression of the target construct in glutamatergic cells. Confocal images of construct expression in a transgenic larva were taken. The larva was the offspring of a founder fish that was out-crossed to the driver line mentioned above. Fig. 32 shows expression of the target constructs in the spinal cord while Fig. 33 shows expression in the hindbrain. Images of GFP expression marking zArchon as well as mOrange expression marking CoChR were taken. The mOrange expression stems from the target construct while GFP-expression marking zArchon is a combination of expression of the target construct and expression from the Gal4 driver line. This is

one explanation for the fact that some cells express GFP only and not mOrange. Another explanation would be related to the T2A linker sequence that joins the two target proteins. Expression of the second protein after the linker sequence is usually less efficient. Plasma membrane localization of the constructs can be clearly observed for both zArchon-GFP (Fig. 32a) and CoChR-mOrange (Fig. 32b). Fig. 33b shows that CoChR-mOrange can form clusters on the plasma membrane in some cases. This is likely due to the soma-targeting sequence of the potassium channel Kv2.1 that was used to tag CoChR-mOrange. The Kv2.1 channel can form clusters on the plasma membrane which has to do with its natural function [97].

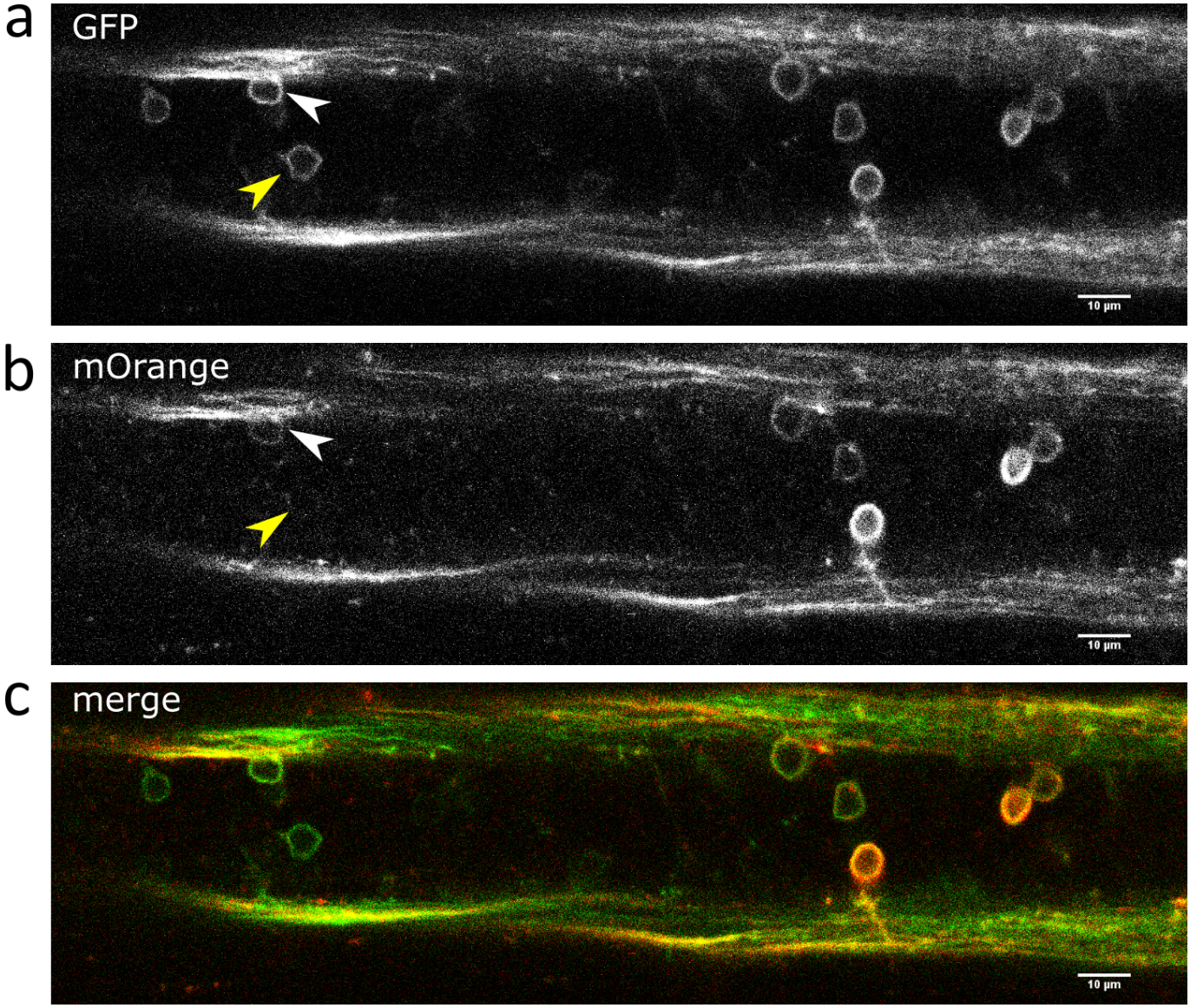

Figure 32: Confocal image of construct expression in the spinal cord of a transgenic zebrafish larva. A confocal image was taken of transgenic zebrafish larva with the genotype *vglut2a:Gal4;UAS-zArchon-GFP;UAS-zArchon-GFP-T2A-CoChR-mOrange-Kv2.1*. The larva was the offspring of a transgenic founder fish of the zebrafish line established in this study and a glutamatergic Gal4 driver line. **(a)** Expression of GFP marking zArchon in the spinal cord. **(b)** Expression of mOrange marking CoChR in the spinal cord. **(c)** Merge of the first two images with GFP expression in green and mOrange expression in red. The white arrows in **a** and **b** mark a cell which expresses GFP but seems to only weakly express mOrange. This could be due to the T2A linker sequence since constructs after the linker sequence tend to express less efficiently. The yellow arrows in **a** and **b** mark a cell that expresses GFP only and cannot be detected in the mOrange channel. This is likely a cell that only received *vglut2a:Gal4;UAS:zArchon-GFP* from the Gal4 driver line, but not the *UAS-zArchon-GFP-T2A-CoChR-mOrange-Kv2.1* sequence from the founder of the line established in this work.

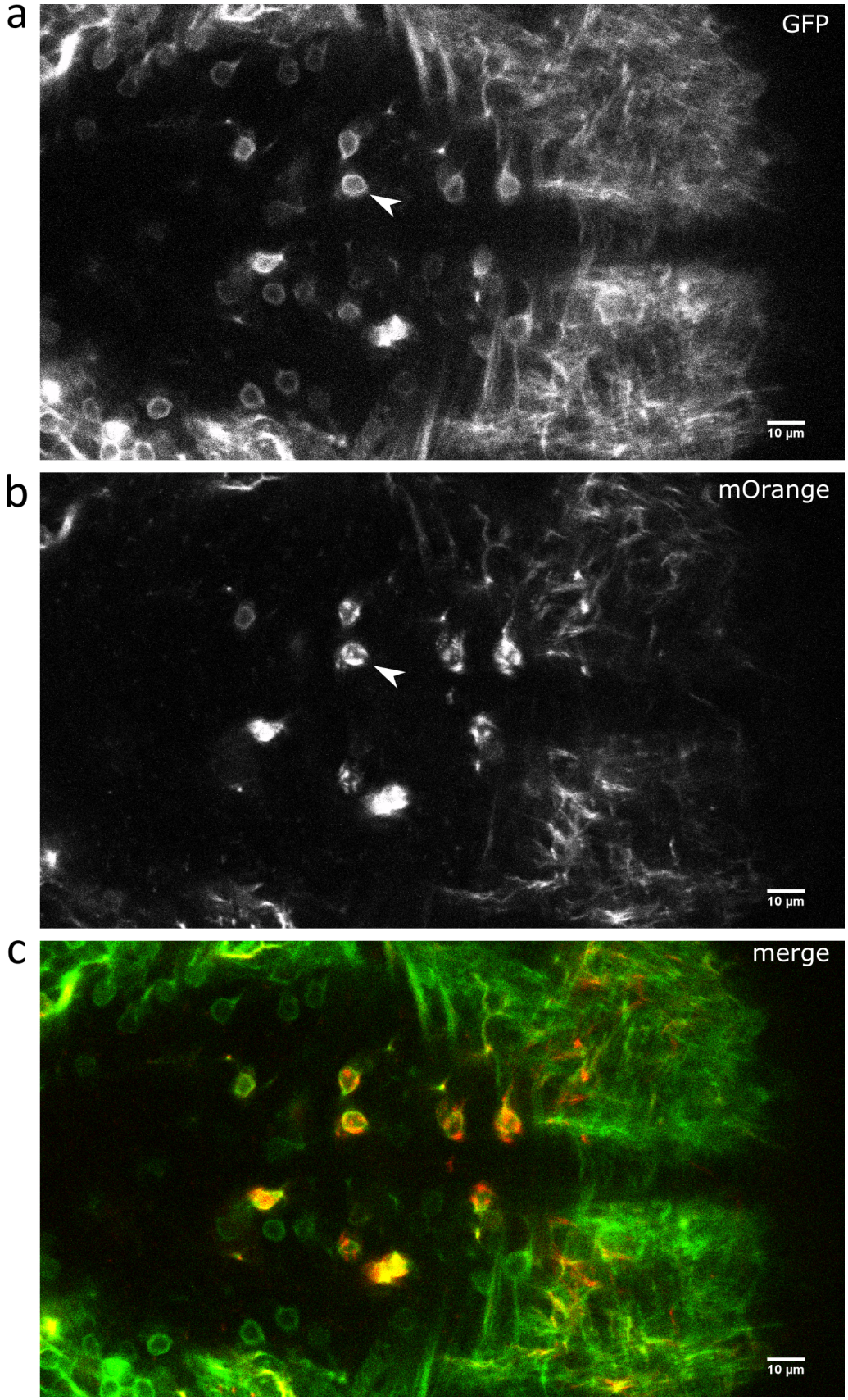

Figure 33: Confocal image of construct expression in the hindbrain of a transgenic zebrafish larva. Confocal images are from the same larva as described in Fig. 32 but taken in the hindbrain instead of the spinal cord. **(a)** GFP expression marking zArchon. **(b)** mOrange expression marking CoChR. **(c)** Overlay of both expression profiles with GFP expression in green and mOrange expression in red. The white arrows in **a** and **b** mark a cell that has uniform GFP expression at the plasma membrane but shows clustered expression of mOrange in **b**. The clusters are likely due to the Kv2.1 soma-localization tag that was used to target CoChR-mOrange to the soma. This explanation is probable since the Kv2.1 channel naturally forms clusters on the plasma membrane [97].

4 Discussion

Simultaneously perturbing and imaging many neurons *in vivo* with spike-time resolution has the potential to unveil fundamental concepts that underlie information processing in the central nervous system. This is possible with all-optical electrophysiology, which combines voltage imaging with optogenetics, and offers the advantage of enabling perturbation and recording of many neurons in parallel compared to conventional electrophysiology methods. Voltage imaging has previously been performed in zebrafish [4], [30]; however, this work describes the first instance in which voltage imaging and optogenetics were successfully combined to establish all-optical electrophysiology in this model system. This represents a powerful new tool that could be used to address many questions in the neuroscience field that remain unanswered to date.

Different excitation techniques including 1P light sheet, 1P widefield and 2P scanning excitation were explored to actuate the channelrhodopsin. 2P excitation offers the advantages of eliminating out of focus excitation, which is especially useful to achieve single-cell excitation, and increasing penetration depths owing to the longer wavelengths used. All three tested methods were successfully able to excite the channelrhodopsin; however 2P excitation is currently less efficient at stimulating channelrhodopsin and further research efforts in this direction are needed to make it an equally effective means of stimulation as 1P excitation.

With all-optical electrophysiology established in zebrafish and shown to be amenable to a wide range of experiments, we sought to explore two research directions. Firstly, we wanted to address the question of functional connectivity in the zebrafish spinal cord by using all-optical electrophysiology to stimulate a single cell and image from many postsynaptic candidates in parallel to search for a postsynaptic response that would imply synaptic connectivity. Secondly, we wanted to investigate the potential of all-optical electrophysiology as a tool to determine E/I-balance.

Finally, as a complement to the transient expression system using injections, for ease of manipulation and to achieve higher construct expression levels, we created a transgenic zebrafish line expressing a channelrhodopsin and a voltage indicator. The work presented here thus represents a promising step toward making all-optical electrophysiology a common tool in the zebrafish model system.

4.1 Constructs for All-Optical Electrophysiology

Several constructs were tested as potential candidates to establish all-optical electrophysiology in zebrafish using embryo injections to achieve transient expression. The first series of constructs made use of the *UAS* promoter and exhibited very sparse and weak expression, making it difficult to find cells that were suitable to test all-optical electrophysiology. The final construct of choice, which was used in most of the experiments presented in this work, made use of the panneuronal *HuC* promoter and exhibited much stronger expression levels. It was first believed that the *UAS* promoter is less efficient for transient expression via injections and works well only in transgenics. However, the E/I-balance experiment in section 3.6 used injections with a *UAS* construct which used a different version of the *UAS* promoter than the initial constructs. This construct was also used to establish the transgenic line. Therefore, there could have been a problem with the particular version of the *UAS* promoter that was used in the first series of constructs that were cloned using the same template. These constructs could technically be tested again using a different version of the promoter. Consequently, the UAS-Gal4 system remains a valuable tool and can also work in transient expression experiments. It offers flexibility since the same constructs can be injected into different driver lines to achieve expression in different subsets of cells without the need for further cloning.

4.2 Voltage Imaging in Zebrafish

State of the art *in vivo* voltage imaging of zebrafish during swimming was successfully replicated in this study. The $\frac{\Delta F}{F}$ values per AP that were achieved with the voltage indicator zArchon in this study ranged from 15% to 40% and were in good agreement with values previously reported by Piatkevich et al. (who developed the voltage sensor zArchon) for voltage imaging in zebrafish [4], which was very encouraging.

Voltage imaging, in principle, offers a non-invasive method to capture neuronal activity in behaving animals. However, many physiological processes, including signaling in the nervous system, are sensitive to heat. For instance, heating of brain tissue has been shown to cause both increase and suppression of spiking behavior in neurons [98], [99]. Since relatively high laser power has to be used to achieve a sufficient signal-to-noise ratio in imaging experiments, it is important to examine the extent to which such illumination can perturb the behavior or affect the viability of the study animal.

Piatkevich et al. used 2.2 $\frac{W}{mm^2}$ at 637 nm to image zArchon in zebrafish using widefield excitation [4]. In this study, red light illumination intensities used for light sheet excitation of zArchon were between 66 and 130 $\frac{W}{mm^2}$ (at 637 nm or 639 nm) and thus were thus 30 - 60 times greater than the ones used by Piatkevich et al. Since the illumination strategy is not the same, it is hard to compare or determine what is responsible for this discrepancy.

However, it is important to note that while the light intensities used in this study appear to be very high, they represent an overestimation of the illumination absorbed by the tissue since most of the light actually traverses the transparent zebrafish without being absorbed. Therefore, damage to the tissue due to high laser powers is of lesser concern in the case of zebrafish than when an opaque tissue is imaged, for example a mouse brain. Additionally, checking the animals for signs of thermal damage revealed no adverse heat effects in this study. In the future, we would like to quantify more rigorously how much of the excitation light is absorbed by the tissue and thus how much energy entering the tissue is converted to heat. This would help to distinguish between true alterations in behavior and artifacts due to heat-induced damage.

4.3 1P and 2P Stimulation of Channelrhodopsin

Three different excitation strategies were tested to stimulate the channelrhodopsin CoChR: 1P light sheet excitation, 1P widefield excitation and 2P scanning excitation. 1P excitation proved to be a very simple and efficient way of stimulating channelrhodopsin. 2P excitation offers the advantage of enabling larger penetration depths, and, more importantly, eliminating out of focus excitation which is crucial for single-cell targeting. While we were able to elicit APs with 2P excitation, it was generally less efficient than 1P. There are two main possible explanations for this result.

Firstly, 2P excitation leads to a very small focal volume ($\sim 1\ \mu m^3$), since it relies on the coincidence of two photons (rather than a single one) with a likelihood that decays quadratically outside of the focal spot. This is a great advantage for single cell targeting; however the small focal volume might also make it harder for 2P light to actuate a sufficient number of channelrhodopsins. We attempted to resolve this issue by increasing the 2P light power and using an axicon to spread the focus in the axial direction. However, in the experiments carried out so far, neither increased power nor the axicon were able to clearly increase 2P stimulation efficiency. An alternative explanation is that 2P light is inherently less efficient at stimulating each individual channelrhodopsin due to intrinsic effects related to channelrhodopsin photophysics. We can speculate, for instance, that the infrared light used during 2P excitation could drive a fraction of the channelrhodopsins into a non-conducting state, decreasing overall efficiency of excitation.

Further experiments are necessary to clarify this issue and successfully implement 2P excitation which would be very beneficial for single-cell targeting.

4.4 Mapping Functional Connectivity

We demonstrate in this study that all-optical electrophysiology has the potential to be a valuable tool to map functional connectivity of neurons. Despite the fact that the results in this study cannot unambiguously assign a functional connection between individual pairs of neurons, it provides a helpful illustration of how a functional connectivity mapping experiment could be set up.

It is helpful to discuss the limitations that might need to be addressed in order to make this approach work better in the future. The approach that was employed to probe connections between neurons involved stimulating a single cell and simultaneously recording from many possible postsynaptic candidates to check for excitatory or inhibitory postsynaptic potentials. Inhibitory postsynaptic potentials are likely harder to detect since the inhibitory reversal potential is closer to the resting membrane potential. The success of such a connectivity mapping experiment relies on the sensitivity of zArchon fluorescence to voltage changes, i.e. on the magnitude of $\frac{\Delta F}{F}$ per mV. In cases, where a connection between two neurons exists, but involves a small number of synapses - maybe even a single one - voltage changes in the postsynaptic cell may fall below the limit of detection.

A simple calculation illustrates this point. Action potentials in zebrafish glutamatergic spinal interneurons have been found to have an amplitude of approximately 50 mV [56]. While the stimulated cell in this study might not have been glutamatergic, we can use this amplitude, as a reasonable approximation, to correspond to 0.16 units of $\frac{\Delta F}{F}$, which was the amplitude of the action potential in the spike-triggered average waveform of cell 9 in Fig. 25a. The unitary excitatory or inhibitory postsynaptic potential, which is the response in a postsynaptic cell to a single action potential fired by one presynaptic neuron, can vary greatly in amplitude from cell to cell. The amplitude depends on the number of synapses which are formed between the two neurons and could range from under 1 mV to around 2 mV. Ampatzis et al. measured monosynaptic excitatory postsynaptic potentials that an excitatory interneuron induced in a motoneuron in the zebrafish spinal cord and found the amplitude to be around 0.2 mV [56]. While in our case the postsynaptic candidates are not motoneurons, this number provides a reasonable estimate for the purposes of this calculation. If a 50 mV AP elicits a change of roughly 0.16 units of $\frac{\Delta F}{F}$ in cell 9, then a 0.2-2 mV postsynaptic potential would elicit a change of 0.00064 - 0.0064 $\frac{\Delta F}{F}$. While the lower value is well below the noise level measured in this experiment (around 0.005 $\frac{\Delta F}{F}$), the upper value is above the noise level and therefore possibly detectable.

These calculations suggest that the current implementation of all-optical electrophysiology may lack the sensitivity to detect cases of weaker interneuron connections, however, it appears to be a promising tool for the cases where the postsynaptic potential is more pronounced.

We propose several directions that should help advance this application and improve the quality of the measurement. Firstly, future experiments should strive to collect larger datasets, which would provide more spike-triggered windows to average over to decrease noise levels. Secondly, several improvements could be made to the experimental protocol that was employed in this study. Blue-light excitation could be targeted to single cells to avoid artifacts such as bleed-through of GFP fluorescence into the imaging channel. Furthermore, the experiment presented in this work was low-throughput since CoChR expression was very sparse and among the CoChR expressing cells, even less cells could be induced to fire APs regularly enough to calculate spike-triggered averages. Therefore, very few presynaptic cells could be tested. Sparse CoChR expression is an advantage for single-cell targeting. However, if 2P single-cell targeting could be made to work more efficiently, it would be helpful to perform such an experiment in a transgenic zebrafish line that expresses constructs for all-optical electrophysiology in many neurons. This would allow to screen more presynaptic cell candidates and check for postsynaptic responses in non-glutamatergic cells as well. With this setting, one could also envisage repeatedly imaging the same field of view containing postsynaptic cell candidates and stimulating different presynaptic cells during each trial to check for functional connectivity. In this case, the aim would be to map the presynaptic cell to the postsynaptic cell, rather than the other way around; however the principle remains the same.

4.5 E/I Balance

E/I-balance describes the ratio between excitatory and inhibitory synaptic inputs to a neuron. It is interesting to study the balance of inhibition and excitation during active behavior, such as zebrafish swimming, or perception of a stimulus, since understanding of synaptic input may reveal information about the implicated circuitry. This work explores the potential of all-optical electrophysiology as a tool for the quantification of E/I-balance. We hypothesize that a simultaneous measurement of the membrane time constant τ and the membrane voltage fluctuations could be used to measure the excitatory and inhibitory conductance changes in time. The experimental approach and its limitations are discussed in the following sections.

4.5.1 Extracting the Membrane Time Constant

The experiment presented in this work aimed to reveal a difference in synaptic inputs during the swimming ON state of larval zebrafish compared to the swimming OFF state in excitatory VeMe spinal interneurons. Zebrafish spinal motor circuits are known to receive descending excitatory input during swimming [100]. VeMe neurons were shown to fire APs mainly during swimming. Spiking activity during swimming could be caused either by an increase in excitation, or a decrease in inhibition during swimming compared to rest. Increased excitation would lead to a higher conductance state during swimming, while decreased inhibition would result in a lower total conductance. Using the fact that the membrane time constant and the total membrane conductance are inversely proportional ($\tau = \frac{C}{G}$, C: capacitance, G: conductance), we deduce that increased excitation could be observed as a decreased membrane time constant whereas decreased inhibition would lead to an increased time constant.

We assumed that increased excitation during swimming would be more likely and expected to find a decreased time constant for the swimming ON case compared to rest, which would reflect on voltage decay dynamics. The results obtained within this study did not reveal an obvious difference between the membrane time constants and thus the total conductance between the swimming ON and swimming OFF states. With more data, statistical significance tests could be performed to quantify significance of the difference between the time constants. Simply observing the decay dynamics in Figs. 27 and 28, however, was enough to determine, as a first step, that the time constant during swimming was not unambiguously smaller than the time constant during rest.

To assess plausibility of our results, we compared the obtained time constants to values found in literature. Data describing the membrane time constants of zebrafish neurons is not abundant, making it challenging to find an appropriate comparison for our study. Buss et al. quantified the membrane time constants of zebrafish spinal motoneurons and found them to have a fast component between $\tau_{fast} \sim$ 2.6 - 3.4 ms and a slow component between $\tau_{slow} \sim$ 36 - 47 ms. The time constants that were determined in this study were between 34 - 37 ms and thus lie within the range of the slow time constant determined by Buss et al. While this is very promising, the all-optical approach to quantify E/I-balance in its current implementation suffers from limitations which are discussed in the following.

A significant limitation has to do with the kinetics of the CoChR channelrhodopsin. We took the time constant of the membrane potential decay dynamics to represent an accurate measure of the membrane conductance, since we assumed that the observed voltage relaxation dynamics are largely governed by the inherent values of conductance and capacitance of the cell. However, membrane potential decay is also affected by the kinetics of the channelrhodopsin that closes when the blue light is turned off. In the limit where the off-time constant of channelrhodopsin is fast compared to the membrane time constant, the approximation that ignores this contribution holds. However, CoChR off-kinetics are slow, with an off-time constant of around 100 ms. If the expected range of the time constant were indeed 36 - 47 ms, the channelrhodopsin off-kinetics of 100 ms could mask detection of differences between time constants in that range. Chronos has a time constant below

10 ms [12] and thus would be a more suitable choice, kinetics-wise; however it could come with other limitations and the lower photocurrent compared to CoChR might make stimulation less efficient.

Another factor which needs to be considered is the fact that spikes elicited during blue light ON periods can have lasting afterhyperpolarizations that could bias the decay dynamics in the following no-spike trial. As no-spike trials during swimming ON are much more rare already, we cannot afford, at this point, to discard no-spike trials which are preceded by spike-trials, since this is almost always the case. However, the analysis pipeline could be adjusted to mitigate this problem and future experiments could collect bigger datasets which could eliminate it.

A general limitation of this technique is that it assumes that synaptic inhibition and excitation are the only time-varying conductances. Voltage-dependent conductances are ignored and the presence of gap junctions could bias the estimation of excitatory and inhibitory synaptic conductances based on membrane potential decay dynamics. It would be wise to asses the abundance of gap junctions in the cell type under study to determine if gap junctions could substantially bias the results.

Overall, the all-optical approach to quantify synaptic conductances as it was presented here has limitations. However, with improvements to the protocol as mentioned above, and importantly, a faster channelrhodopsin, all-optical electrophysiology has the potential to be a helpful tool in the quantification of E/I-balance. The VeMe cells that were studied here have been described in literature, however their exact function is still unknown. As a necessary next step we propose to test our tool on a well-characterized cell type, whose synaptic inputs are known, and validate results through a comparison with patch-clamp measurements of synaptic conductances.

4.6 Transgenic Zebrafish Line for All-Optical Electrophysiology

A transgenic zebrafish line that expresses constructs necessary for all-optical electrophysiology under the *UAS* promoter has been established within this study. The constructs are not directly expressed in the transgenic line. To achieve expression, the line needs to be crossed to a Gal4-driver line which expresses the actuating protein Gal4 that is necessary to drive expression of constructs under the *UAS* promoter. A *UAS* transgenic line offers flexibility since it can be crossed to a variety of different Gal4 driver lines, driving Gal4 expression and thus the actuation of construct expression under panneuronal or cell-specific promoters.

During the generation of this transgenic line, several problems involving transpose mRNA degradation were encountered. The importance of working in an RNase-free environment is thus underlined here.

The first transgenic adult zebrafish from this line reached maturity and were crossed just as this report was written. The confocal images in Figs. 32 and 33 of a transgenic zebrafish from the line that was established in this study, crossed to a *vglut2a:Gal4;UAS-zArchon-GFP* driver line, prove that transgenesis was successful. Less cells were found to express CoChR-mOrange compared to zArchon, which was attributed to additional zArchon expression from the Gal4 driver line and the fact that CoChR-mOrange was the second construct after the *T2A* sequence, which usually expresses less efficiently. No functional data was obtained from the new zebrafish line as of yet. Experiments with the new line will show whether zArchon expression levels are sufficient to obtain high quality functional data. It could be that heterozygous transgenics do not exhibit sufficient expression after the cross to the driver line. Therefore, one might have to cross the transgenic line to a driver line, raise the offspring and then perform in-crosses among them to achieve homozygous transgenics with a Gal4 driver.

5 Conclusion

Voltage imaging is a powerful technique that can visualize membrane potential with spike-time temporal precision and can reveal subthreshold oscillations. Other techniques to study neuronal activity such as calcium imaging do not have equally high temporal resolution and cannot visualize subthreshold oscillations. Voltage imaging also allows the recording of membrane potential dynamics of many neurons at once, which is an advantage compared to patch-clamp recordings. Voltage imaging cannot perturb neurons, which would be helpful in the process of determining the function of neural circuits. However, the combination of voltage imaging with optogenetics - all-optical electrophysiology - can be used to both perturb and record neuron membrane potential dynamics and is therefore a very valuable tool. While voltage imaging had previously been shown in zebrafish, it had not been combined with optogenetics. This study, for the first time, establishes all-optical electrophysiology in zebrafish by expressing both a voltage indicator and a channelrhodopsin in zebrafish neurons. We tested different excitation techniques including 1P light sheet, 1P widefield and 2P scanning to actuate the channelrhodopsin. 1P excitation proved to be more efficient at channelrhodopsin activation than 2P excitation. After having established all-optical electrophysiology in zebrafish and demonstrated its functionality, we aimed to explore two interesting applications of the technology. First, we addressed the problem of functional connectivity mapping in the zebrafish spinal cord. While not being able to unambiguously show the functional connection of two neurons, this study offers a helpful guide as to how a functional connectivity mapping experiment could be set up and which limitations need to be addressed. Secondly, we explored the potential of optical electrophysiology to quantify E/I-balance. We showed how such a measurement could in principle be implemented and found that a faster channelrhodopsin than the one used in this study would be helpful to accurately quantify E/I-balance. Finally, a transgenic zebrafish line expressing the necessary constructs for all-optical electrophysiology was established and has the potential to lower the barrier for others to harness all-optical electrophysiology to answer their research questions.

In the future, it would be helpful to find a way to efficiently stimulate CoChR using 2P excitation. This could enable single-cell targeting of excitation and would be useful to actuate cells in a transgenic line that has broad expression of both channelrhodospin and voltage indicator, such as the one established in this study. Regarding the zebrafish line that was established in this study, the next step would be to characterize it functionally. For the quantification of E/I-balance, a new transgenic zebrafish line with a faster channelrhodopsin may need to be created. However, the zebrafish line established in this study could be very helpful for mapping functional connectivity in a more high-throughput manner in the future.

References

[1] Daniel R. Hochbaum et al. "All-optical electrophysiology in mammalian neurons using engineered microbial rhodopsins". In: *Nature Methods* 11.8 (2014), pp. 825–833. ISSN: 15487105. DOI: 10.1038/NMETH.3000. URL: http://dx.doi.org/10.1038/nmeth.3000.

[2] Wenjing Wang, Christina K. Kim, and Alice Y. Ting. "Molecular tools for imaging and recording neuronal activity". In: *Nature Chemical Biology* 15.2 (Feb. 2019), pp. 101–110. ISSN: 1552-4450. DOI: 10.1038/s41589-018-0207-0. URL: http://www.nature.com/articles/s41589-018-0207-0.

[3] Michael Z. Lin and Mark J. Schnitzer. "Genetically encoded indicators of neuronal activity". In: *Nature Neuroscience* 19.9 (2016), pp. 1142–1153. ISSN: 15461726. DOI: 10.1038/nn.4359.

[4] Kiryl D. Piatkevich et al. "A robotic multidimensional directed evolution approach applied to fluorescent voltage reporters". In: *Nature Chemical Biology* 14.9 (2018), p. 901. ISSN: 15524469. DOI: 10.1038/s41589-018-0023-6. URL: http://dx.doi.org/10.1038/s41589-018-0004-9.

[5] Yoav Adam et al. "Voltage imaging and optogenetics reveal behaviour-dependent changes in hippocampal dynamics". In: *Nature* 569.7756 (May 2019), pp. 413–417. ISSN: 0028-0836. DOI: 10.1038/s41586-019-1166-7. URL: http://www.nature.com/articles/s41586-019-1166-7.

[6] Linlin Z. Fan et al. "All-optical electrophysiology reveals excitation, inhibition, and neuromodulation in cortical layer 1". In: *bioRxiv* (Apr. 2019), p. 614172. DOI: 10.1101/614172. URL: https://www.biorxiv.org/content/10.1101/614172v1.abstract.

[7] Adam E. Cohen and Samouil L. Farhi. "Sculpting light to reveal brain function". In: *Nature Neuroscience* 21.6 (June 2018), pp. 776–778. ISSN: 1097-6256. DOI: 10.1038/s41593-018-0158-5. URL: http://www.nature.com/articles/s41593-018-0158-5.

[8] Yongxian Xu, Peng Zou, and Adam E. Cohen. "Voltage imaging with genetically encoded indicators". In: *Current Opinion in Chemical Biology* 39 (2017), pp. 1–10. ISSN: 18790402. DOI: 10.1016/j.cbpa.2017.04.005. URL: http://dx.doi.org/10.1016/j.cbpa.2017.04.005.

[9] Edward S Boyden et al. "Millisecond-timescale, genetically targeted optical control of neural activity". In: *Nature Neuroscience* 8.9 (Sept. 2005), pp. 1263–1268. ISSN: 1097-6256. DOI: 10.1038/nn1525. URL: http://www.nature.com/articles/nn1525.

[10] Edward S Boyden. "A history of optogenetics: the development of tools for controlling brain circuits with light." In: *F1000 biology reports* 3 (2011), p. 11. ISSN: 1757-594X. DOI: 10.3410/B3-11. URL: http://www.ncbi.nlm.nih.gov/pubmed/21876722%20http://www.pubmedcentral.nih.gov/articlerender.fcgi?artid=PMC3155186.

[11] J Simon Wiegert et al. "Review Silencing Neurons: Tools, Applications, and Experimental Constraints". In: (2017). DOI: 10.1016/j.neuron.2017.06.050. URL: http://dx.doi.org/10.1016/j.neuron.2017.06.050.

[12] Nathan C. Klapoetke et al. "Independent optical excitation of distinct neural populations". In: *Nature Methods* 11.3 (2014), pp. 338–346. ISSN: 15487105. DOI: 10.1038/nmeth.2836.

[13] Elena G Govorunova et al. "Natural light-gated anion channels: A family of microbial rhodopsins for advanced optogenetics." In: *Science (New York, N.Y.)* 349.6248 (Aug. 2015), pp. 647–50. DOI: 10.1126/science.aaa7484. URL: https://science.sciencemag.org/content/349/6248/647.

[14] Ahmed Abdelfattah et al. "Bright and photostable chemigenetic indicators for extended in vivo voltage imaging". In: *Science* 6416.August (2019), p. 436840. DOI: DOI:10.1126/science.aav6416. URL: https://science.sciencemag.org/content/early/2019/07/31/science.aav6416.

[15] Massimo Scanziani and Michael Häusser. "Electrophysiology in the age of light". In: *Nature* 461.7266 (2009), pp. 930–939. ISSN: 00280836. DOI: 10.1038/nature08540.

[16] François St-Pierre, Mariya Chavarha, and Michael Z Lin. "Designs and sensing mechanisms of genetically encoded fluorescent voltage indicators". In: *Current Opinion in Chemical Biology* 27 (Aug. 2015), pp. 31–38. ISSN: 1367-5931. DOI: 10.1016/J.CBPA.2015.05.003. URL: https://www.sciencedirect.com/science/article/pii/S1367593115000459.

[17] Micah S Siegel and Ehud Y Isacoff. "A Genetically Encoded Optical Probe of Membrane Voltage". In: *Neuron* 19.4 (Oct. 1997), pp. 735–741. ISSN: 0896-6273. DOI: 10.1016/S0896-6273(00)80955-1. URL: https://www.sciencedirect.com/science/article/pii/S0896627300809551.

[18] Dimitar Dimitrov et al. "Engineering and Characterization of an Enhanced Fluorescent Protein Voltage Sensor". In: *PLoS ONE* 2.5 (May 2007). Ed. by Hiroaki Matsunami, e440. ISSN: 1932-6203. DOI: 10.1371/journal.pone.0000440. URL: https://dx.plos.org/10.1371/journal.pone.0000440.

[19] Lei Jin et al. "Single Action Potentials and Subthreshold Electrical Events Imaged in Neurons with a Fluorescent Protein Voltage Probe". In: *Neuron* 75.5 (Sept. 2012), pp. 779–785. ISSN: 0896-6273. DOI: 10.1016/J.NEURON.2012.06.040. URL: https://www.sciencedirect.com/science/article/pii/S0896627312007040.

[20] François St-Pierre et al. "High-fidelity optical reporting of neuronal electrical activity with an ultrafast fluorescent voltage sensor". In: *Nature Neuroscience* 17.6 (June 2014), pp. 884–889. ISSN: 1097-6256. DOI: 10.1038/nn.3709. URL: http://www.nature.com/articles/nn.3709.

[21] Helen H. Yang et al. "Subcellular Imaging of Voltage and Calcium Signals Reveals Neural Processing In Vivo". In: *Cell* 166.1 (June 2016), pp. 245–257. DOI: 10.1016/J.CELL.2016.05.031. URL: https://www.sciencedirect.com/science/article/pii/S0092867416305827#bib42.

[22] Simon Chamberland et al. "Fast two-photon imaging of subcellular voltage dynamics in neuronal tissue with genetically encoded indicators". In: *eLife* 6 (July 2017). DOI: 10.7554/eLife.25690. URL: https://elifesciences.org/articles/25690.

[23] Mariya Chavarha et al. "Fast two-photon volumetric imaging of an improved voltage indicator reveals electrical activity in deeply located neurons in the awake brain". In: *bioRxiv* (Oct. 2018), p. 445064. DOI: 10.1101/445064. URL: https://www.biorxiv.org/content/10.1101/445064v1.abstract.

[24] Ahmed S Abdelfattah et al. "A Bright and Fast Red Fluorescent Protein Voltage Indicator That Reports Neuronal Activity in Organotypic Brain Slices." In: *The Journal of neuroscience : the official journal of the Society for Neuroscience* 36.8 (Feb. 2016), pp. 2458–72. ISSN: 1529-2401. DOI: 10.1523/JNEUROSCI.3484-15.2016.

[25] Joel M Kralj et al. "Electrical spiking in Escherichia coli probed with a fluorescent voltage-indicating protein." In: *Science (New York, N.Y.)* 333.6040 (July 2011), pp. 345–8. ISSN: 1095-9203. DOI: 10.1126/science.1204763. URL: http://www.ncbi.nlm.nih.gov/pubmed/21764748.

[26] Brian Y. Chow et al. "High-performance genetically targetable optical neural silencing by light-driven proton pumps". In: *Nature* 463.7277 (Jan. 2010), pp. 98–102. DOI: 10.1038/nature08652. URL: http://www.nature.com/articles/nature08652.

[27] Joel M. Kralj et al. "Optical recording of action potentials in mammalian neurons using a microbial rhodopsin". In: *Nature Methods* 9.1 (2012), pp. 90–95. ISSN: 15487091. DOI: 10.1038/nmeth.1782. URL: https://www.nature.com/articles/nmeth.1782.

[28] Yiyang Gong et al. "High-speed recording of neural spikes in awake mice and flies with a fluorescent voltage sensor." In: *Science (New York, N.Y.)* 350.6266 (Dec. 2015), pp. 1361–6. ISSN: 1095-9203. DOI: 10.1126/science.aab0810. URL: https://science.sciencemag.org/content/350/6266/1361.

[29] Madhuvanthi Kannan et al. "Fast, in vivo voltage imaging using a red fluorescent indicator". In: *Nature Methods* 15.12 (Dec. 2018), pp. 1108–1116. ISSN: 1548-7091. DOI: 10.1038/s41592-018-0188-7. URL: http://www.nature.com/articles/s41592-018-0188-7.

[30] Ahmed S. Abdelfattah et al. "Bright and photostable chemigenetic indicators for extended in vivo voltage imaging". In: *Science* (Aug. 2019), eaav6416. ISSN: 0036-8075. DOI: 10.1126/science.aav6416. URL: http://www.sciencemag.org/lookup/doi/10.1126/science.aav6416.

[31] Boris V. Zemelman et al. "Selective Photostimulation of Genetically ChARGed Neurons". In: *Neuron* 33.1 (Jan. 2002), pp. 15–22. ISSN: 0896-6273. DOI: 10.1016/S0896-6273(01)00574-8. URL: https://www.sciencedirect.com/science/article/pii/S0896627301005748.

[32] B. V. Zemelman et al. "Photochemical gating of heterologous ion channels: Remote control over genetically designated populations of neurons". In: *Proceedings of the National Academy of Sciences* 100.3 (Feb. 2003), pp. 1352–1357. ISSN: 0027-8424. DOI: 10.1073/pnas.242738899.

[33] Susana Q. Lima and Gero Miesenböck. "Remote control of behavior through genetically targeted photostimulation of neurons". In: *Cell* 121.1 (Apr. 2005), pp. 141–152. ISSN: 00928674. DOI: 10.1016/j.cell.2005.02.004.

[34] Georg Nagel et al. "Channelrhodopsin-2, a directly light-gated cation-selective membrane channel." In: *Proceedings of the National Academy of Sciences of the United States of America* 100.24 (Nov. 2003), pp. 13940–5. ISSN: 0027-8424. DOI: 10.1073/pnas.1936192100. URL: https://www.pnas.org/content/100/24/13940.long.

[35] Karl Deisseroth and Peter Hegemann. "The form and function of channelrhodopsin." In: *Science (New York, N.Y.)* 357.6356 (Sept. 2017), eaan5544. ISSN: 1095-9203. DOI: 10.1126/science.aan5544. URL: https://science.sciencemag.org/content/357/6356/eaan5544.abstract.

[36] Karl Deisseroth et al. "Next-generation optical technologies for illuminating genetically targeted brain circuits." In: *The Journal of neuroscience : the official journal of the Society for Neuroscience* 26.41 (Oct. 2006), pp. 10380–6. ISSN: 1529-2401. DOI: 10.1523/JNEUROSCI.3863-06.2006.

[37] Sheena A Josselyn. "The past, present and future of light-gated ion channels and optogenetics". In: *eLife* 7 (Oct. 2018). ISSN: 2050-084X. DOI: 10.7554/eLife.42367. URL: https://elifesciences.org/articles/42367.

[38] Lief Fenno, Ofer Yizhar, and Karl Deisseroth. "The Development and Application of Optogenetics". In: *Annual Review of Neuroscience* 34.1 (July 2011), pp. 389–412. ISSN: 0147-006X. DOI: 10.1146/annurev-neuro-061010-113817. URL: http://www.annualreviews.org/doi/10.1146/annurev-neuro-061010-113817.

[39] Hideaki E. Kato et al. "Crystal structure of the channelrhodopsin light-gated cation channel". In: *Nature* 482.7385 (Feb. 2012), pp. 369–374. DOI: 10.1038/nature10870. URL: http://www.nature.com/articles/nature10870.

[40] Arash Kianianmomeni, ed. *Optogenetics*. Vol. 1408. Methods in Molecular Biology. New York, NY: Springer New York, 2016. ISBN: 978-1-4939-3510-9. DOI: 10.1007/978-1-4939-3512-3. URL: http://link.springer.com/10.1007/978-1-4939-3512-3.

[41] Andre Berndt et al. "Structural foundations of optogenetics: Determinants of channelrhodopsin ion selectivity." In: *Proceedings of the National Academy of Sciences of the United States of America* 113.4 (Jan. 2016), pp. 822–9. DOI: 10.1073/pnas.1523341113. URL: http://www.ncbi.nlm.nih.gov/pubmed/26699459%20http://www.ncbi.nlm.nih.gov/pubmed/26699459.

[42] Jonas Wietek et al. "An improved chloride-conducting channelrhodopsin for light-induced inhibition of neuronal activity in vivo". In: *Scientific Reports* 5.1 (Dec. 2015), p. 14807. DOI: 10.1038/srep14807. URL: http://www.nature.com/articles/srep14807.

[43] André Berndt et al. "Bi-stable neural state switches". In: *Nature Neuroscience* 12.2 (Feb. 2009), pp. 229–234. DOI: 10.1038/nn.2247. URL: http://www.nature.com/articles/nn.2247.

[44] Feng Zhang et al. "Red-shifted optogenetic excitation: a tool for fast neural control derived from Volvox carteri". In: *Nature Neuroscience* 11.6 (June 2008), pp. 631–633. ISSN: 1097-6256. DOI: 10.1038/nn.2120. URL: http://www.nature.com/articles/nn.2120.

[45] Karel Svoboda and Ryohei Yasuda. "Principles of Two-Photon Excitation Microscopy and Its Applications to Neuroscience". In: *Neuron* 50.6 (June 2006), pp. 823–839. DOI: 10.1016/J.NEURON.2006.05.019. URL: https://www.sciencedirect.com/science/article/pii/S0896627306004119.

[46] Jerome Mertz. "Optical sectioning microscopy with planar or structured illumination". In: *Nature Methods* 8.10 (2011), pp. 811–819. ISSN: 15487091. DOI: 10.1038/nmeth.1709. URL: http://dx.doi.org/10.1038/nmeth.1709.

[47] Misha B Ahrens et al. "Whole-brain functional imaging at cellular resolution using light-sheet microscopy". In: *Nature Methods* 10.5 (May 2013), pp. 413–420. ISSN: 1548-7091. DOI: 10.1038/nmeth.2434. URL: http://www.nature.com/articles/nmeth.2434.

[48] Thomas Panier et al. "Fast functional imaging of multiple brain regions in intact zebrafish larvae using Selective Plane Illumination Microscopy". In: *Frontiers in Neural Circuits* 7 (Apr. 2013), p. 65. ISSN: 1662-5110. DOI: 10.3389/fncir.2013.00065. URL: http://journal.frontiersin.org/article/10.3389/fncir.2013.00065/abstract.

[49] J A Lister et al. "Nacre Encodes a Zebrafish Microphthalmia-Related Protein That Regulates Neural-Crest-Derived Pigment Cell Fate." In: *Development (Cambridge, England)* 126.17 (1999), pp. 3757–67. ISSN: 0950-1991. URL: https://dev.biologists.org/content/126/17/3757.short.

[50] Richard Mark White et al. "Transparent Adult Zebrafish as a Tool for In Vivo Transplantation Analysis". In: *Cell Stem Cell* 2.2 (Feb. 2008), pp. 183–189. DOI: 10.1016/J.STEM.2007.11.002. URL: https://www.sciencedirect.com/science/article/pii/S1934590907002755.

[51] Adam Michael Stewart et al. "Zebrafish models for translational neuroscience research: from tank to bedside". In: *Trends in Neurosciences* 37.5 (May 2014), pp. 264–278. ISSN: 0166-2236. DOI: 10.1016/J.TINS.2014.02.011. URL: https://www.sciencedirect.com/science/article/pii/S0166223614000277.

[52] Shin-Ichi Higashijima, Gail Mandel, and Joseph R. Fetcho. "Distribution of prospective glutamatergic, glycinergic, and GABAergic neurons in embryonic and larval zebrafish". In: *The Journal of Comparative Neurology* 480.1 (Nov. 2004), pp. 1–18. DOI: 10.1002/cne.20278. URL: http://doi.wiley.com/10.1002/cne.20278.

[53] Hae-Chul Park et al. "Analysis of Upstream Elements in the HuC Promoter Leads to the Establishment of Transgenic Zebrafish with Fluorescent Neurons". In: *Developmental Biology* 227.2 (Nov. 2000), pp. 279–293. DOI: 10.1006/DBIO.2000.9898. URL: https://www.sciencedirect.com/science/article/pii/S0012160600998981.

[54] Eva M. Berg et al. "Principles Governing Locomotion in Vertebrates: Lessons From Zebrafish". In: *Frontiers in Neural Circuits* 12 (Sept. 2018), p. 73. DOI: 10.3389/fncir.2018.00073. URL: https://www.frontiersin.org/article/10.3389/fncir.2018.00073/full.

[55] Ole Kiehn. "Decoding the organization of spinal circuits that control locomotion". In: *Nature Reviews Neuroscience* 17.4 (Apr. 2016), pp. 224–238. ISSN: 1471-003X. DOI: 10.1038/nrn.2016.9. URL: http://www.nature.com/articles/nrn.2016.9.

[56] Konstantinos Ampatzis et al. "Separate Microcircuit Modules of Distinct V2a Interneurons and Motoneurons Control the Speed of Locomotion". In: *Neuron* 83.4 (Aug. 2014), pp. 934–943. ISSN: 0896-6273. DOI: 10.1016/J.NEURON.2014.07.018. URL: https://www.sciencedirect.com/science/article/pii/S0896627314006291.

[57] Melina E. Hale, Dale A. Ritter, and Joseph R. Fetcho. "A confocal study of spinal interneurons in living larval zebrafish". In: *The Journal of Comparative Neurology* 437.1 (Aug. 2001), pp. 1–16. ISSN: 0021-9967. DOI: 10.1002/cne.1266. URL: http://doi.wiley.com/10.1002/cne.1266.

[58] Shin-Ichi Higashijima, Michael Schaefer, and Joseph R. Fetcho. "Neurotransmitter properties of spinal interneurons in embryonic and larval zebrafish". In: *The Journal of Comparative Neurology* 480.1 (Nov. 2004), pp. 19–37. ISSN: 0021-9967. DOI: 10.1002/cne.20279. URL: http://doi.wiley.com/10.1002/cne.20279.

[59] Kazuhide Asakawa and Koichi Kawakami. "Targeted gene expression by the Gal4-UAS system in zebrafish". In: *Development, Growth & Differentiation* 50.6 (Aug. 2008), pp. 391–399. ISSN: 00121592. DOI: 10.1111/j.1440-169X.2008.01044.x. URL: http://doi.wiley.com/10.1111/j.1440-169X.2008.01044.x.

[60] K. Kawakami et al. "Tol2-mediated transgenesis, gene trapping, enhancer trapping, and Gal4-UAS system". In: *Methods in Cell Biology* 135 (Jan. 2016), pp. 19–37. DOI: 10.1016/BS.MCB.2016.01.011. URL: https://www.sciencedirect.com/science/article/pii/S0091679X16000121?via%3Dihub.

[61] Koichi Kawakami. "Tol2: a versatile gene transfer vector in vertebrates." In: *Genome biology* 8 Suppl 1.Suppl 1 (2007), S7. ISSN: 1474-760X. DOI: 10.1186/gb-2007-8-s1-s7. URL: http://www.ncbi.nlm.nih.gov/pubmed/18047699%20http://www.pubmedcentral.nih.gov/articlerender.fcgi?artid=PMC2106836.

[62] Chaehyun Yook, Shaul Druckmann, and Jinhyun Kim. "Mapping mammalian synaptic connectivity". In: *Cellular and Molecular Life Sciences* 70.24 (Dec. 2013), pp. 4747–4757. ISSN: 1420-682X. DOI: 10.1007/s00018-013-1417-y. URL: http://link.springer.com/10.1007/s00018-013-1417-y.

[63] David Grant Colburn Hildebrand et al. "Whole-brain serial-section electron microscopy in larval zebrafish". In: *Nature* 545.7654 (May 2017), pp. 345–349. ISSN: 0028-0836. DOI: 10.1038/nature22356. URL: http://www.nature.com/articles/nature22356.

[64] Jean Livet et al. "Transgenic strategies for combinatorial expression of fluorescent proteins in the nervous system". In: *Nature* 450.7166 (Nov. 2007), pp. 56–62. DOI: 10.1038/nature06293. URL: http://www.nature.com/articles/nature06293.

[65] Evan H. Feinberg et al. "GFP Reconstitution Across Synaptic Partners (GRASP) Defines Cell Contacts and Synapses in Living Nervous Systems". In: *Neuron* 57.3 (Feb. 2008), pp. 353–363. DOI: 10.1016/J.NEURON.2007.11.030. URL: https://www.sciencedirect.com/science/article/pii/S0896627307010203.

[66] Jinhyun Kim et al. "mGRASP enables mapping mammalian synaptic connectivity with light microscopy". In: *Nature Methods* 9.1 (Jan. 2012), pp. 96–102. DOI: 10.1038/nmeth.1784. URL: http://www.nature.com/articles/nmeth.1784.

[67] Talia N. Lerner, Li Ye, and Karl Deisseroth. "Communication in Neural Circuits: Tools, Opportunities, and Challenges". In: *Cell* 164.6 (Mar. 2016), pp. 1136–1150. ISSN: 0092-8674. DOI: 10.1016/J.CELL.2016.02.027. URL: https://www.sciencedirect.com/science/article/pii/S0092867416301295.

[68] Ian R. Wickersham et al. "Monosynaptic Restriction of Transsynaptic Tracing from Single, Genetically Targeted Neurons". In: *Neuron* 53.5 (Mar. 2007), pp. 639–647. DOI: 10.1016/J.NEURON.2007.01.033. URL: https://www.sciencedirect.com/science/article/pii/S0896627307000785.

[69] Kwanghun Chung et al. "Structural and molecular interrogation of intact biological systems". In: *Nature* 497.7449 (May 2013), pp. 332–337. DOI: 10.1038/nature12107. URL: http://www.nature.com/articles/nature12107.

[70] Fei Chen, Paul W Tillberg, and Edward S Boyden. "Expansion microscopy." In: *Science (New York, N.Y.)* 347.6221 (Jan. 2015), pp. 543–8. ISSN: 1095-9203. DOI: 10.1126/science.1260088. URL: https://science.sciencemag.org/content/347/6221/543.

[71] "Human Connectome Project — Mapping the human brain connectivity". In: (). URL: http://www.humanconnectomeproject.org/.

[72] Seung Wook Oh et al. "A mesoscale connectome of the mouse brain". In: *Nature* 508.7495 (Apr. 2014), pp. 207–214. DOI: 10.1038/nature13186. URL: http://www.nature.com/articles/nature13186.

[73] Lyric A. Jorgenson et al. "The BRAIN Initiative: developing technology to catalyse neuroscience discovery". In: *Philosophical Transactions of the Royal Society B: Biological Sciences* 370.1668 (May 2015), p. 20140164. DOI: 10.1098/rstb.2014.0164. URL: https://royalsocietypublishing.org/doi/10.1098/rstb.2014.0164.

[74] J. G. White et al. "The Structure of the Nervous System of the Nematode Caenorhabditis elegans". In: *Philosophical Transactions of the Royal Society B: Biological Sciences* 314.1165 (Nov. 1986), pp. 1–340. ISSN: 0962-8436. DOI: 10.1098/rstb.1986.0056. URL: http://rstb.royalsocietypublishing.org/cgi/doi/10.1098/rstb.1986.0056.

[75] Martin Gorges et al. "Functional Connectivity Mapping in the Animal Model: Principles and Applications of Resting-State fMRI". In: *Frontiers in Neurology* 8 (May 2017), p. 200. ISSN: 1664-2295. DOI: 10.3389/fneur.2017.00200. URL: http://journal.frontiersin.org/article/10.3389/fneur.2017.00200/full.

[76] Leopoldo Petreanu et al. "Channelrhodopsin-2–assisted circuit mapping of long-range callosal projections". In: *Nature Neuroscience* 10.5 (May 2007), pp. 663–668. ISSN: 1097-6256. DOI: 10.1038/nn1891. URL: http://www.nature.com/articles/nn1891.

[77] Kerri Smith. "How to map the circuits that define us". In: *Nature* 548.7666 (Aug. 2017), pp. 150–152. ISSN: 0028-0836. DOI: 10.1038/548150a. URL: http://www.nature.com/articles/548150a.

[78] P. C. Petersen et al. "Premotor Spinal Network with Balanced Excitation and Inhibition during Motor Patterns Has High Resilience to Structural Division". In: *Journal of Neuroscience* 34.8 (2014), pp. 2774–2784. ISSN: 0270-6474. DOI: 10.1523/jneurosci.3349-13.2014.

[79] C. Monier, J. Fournier, and Y. Frégnac. "In vitro and in vivo measures of evoked excitatory and inhibitory conductance dynamics in sensory cortices". In: *Journal of Neuroscience Methods* 169.2 (Apr. 2008), pp. 323–365. ISSN: 0165-0270. DOI: 10.1016/J.JNEUMETH.2007.11.008. URL: https://www.sciencedirect.com/science/article/pii/S0165027007005547.

[80] Shanglin Zhou and Yuguo Yu. "Synaptic E-I balance underlies efficient neural coding". In: *Frontiers in Neuroscience* 12.FEB (2018), pp. 1–11. ISSN: 1662453X. DOI: 10.3389/fnins.2018.00046.

[81] Rune W. Berg and Susanne Ditlevsen. "Synaptic inhibition and excitation estimated via the time constant of membrane potential fluctuations". In: *Journal of Neurophysiology* 110.4 (2013), pp. 1021–1034. ISSN: 0022-3077. DOI: 10.1152/jn.00006.2013.

[82] Michael Okun and Ilan Lampl. "Instantaneous correlation of excitation and inhibition during ongoing and sensory-evoked activities". In: *Nature Neuroscience* 11.5 (2008), pp. 535–537. ISSN: 10976256. DOI: 10.1038/nn.2105.

[83] Ilan Lampl. "Principles for simultaneous measurement of excitatory and inhibitory conductances of single cells in a single trial". In: *bioRxiv* (July 2019), p. 690719. DOI: 10.1101/690719. URL: https://www.biorxiv.org/content/10.1101/690719v1.

[84] Jin Hee Kim et al. "High Cleavage Efficiency of a 2A Peptide Derived from Porcine Teschovirus-1 in Human Cell Lines, Zebrafish and Mice". In: *PLoS ONE* 6.4 (Apr. 2011). Ed. by Volker Thiel, e18556. ISSN: 1932-6203. DOI: 10.1371/journal.pone.0018556. URL: https://dx.plos.org/10.1371/journal.pone.0018556.

[85] Seung T Lim et al. "A Novel Targeting Signal for Proximal Clustering of the Kv2.1 K+ Channel in Hippocampal Neurons". In: *Neuron* 25.2 (Feb. 2000), pp. 385–397. ISSN: 0896-6273. DOI: 10.1016/S0896-6273(00)80902-2. URL: https://www.sciencedirect.com/science/article/pii/S0896627300809022.

[86] Daniel G Gibson et al. "Enzymatic assembly of DNA molecules up to several hundred kilobases". In: *Nature Methods* 6.5 (May 2009), pp. 343–345. ISSN: 1548-7091. DOI: 10.1038/nmeth.1318. URL: http://www.nature.com/articles/nmeth.1318.

[87] New England BioLabs Inc. *NEBuilder*. URL: http://nebuilder.neb.com/.

[88] Integrated DNA Technologies (IDT). *Custom DNA Oligo Products*. URL: https://www.idtdna.com/pages/products/custom-dna-rna/dna-oligos/custom-dna-oligos.

[89] GeneWiz. *Sanger Sequencing*. URL: https://www.genewiz.com/.

[90] C. Satou et al. "Transgenic tools to characterize neuronal properties of discrete populations of zebrafish neurons". In: *Development* (2013). ISSN: 0950-1991. DOI: 10.1242/dev.099531.

[91] Sigrid Mensch et al. "Synaptic vesicle release regulates myelin sheath number of individual oligodendrocytes in vivo". In: *Nature Neuroscience* 18.5 (Apr. 2015), pp. 628–630. ISSN: 15461726. DOI: 10.1038/nn.3991.

[92] Misha B. Ahrens et al. "Brain-wide neuronal dynamics during motor adaptation in zebrafish". In: *Nature* 485.7399 (May 2012), pp. 471–477. ISSN: 00280836. DOI: 10.1038/nature11057.

[93] Maximiliano L. Suster et al. "Transgenesis in Zebrafish with the Tol2 Transposon System". In: Transgenesis Techniques, 2009, pp. 41–63. DOI: 10.1007/978-1-60327-019-9{_}3. URL: http://link.springer.com/10.1007/978-1-60327-019-9_3.

[94] John H. McLeod. "The Axicon: A New Type of Optical Element". In: *Journal of the Optical Society of America* 44.8 (Aug. 1954), p. 592. ISSN: 0030-3941. DOI: 10.1364/JOSA.44.000592. URL: https://www.osapublishing.org/abstract.cfm?URI=josa-44-8-592.

[95] Gabrielle Thériault, Yves De Koninck, and Nathalie McCarthy. "Extended depth of field microscopy for rapid volumetric two-photon imaging". In: *Optics Express* 21.8 (Apr. 2013), p. 10095. ISSN: 1094-4087. DOI: 10.1364/OE.21.010095. URL: https://www.osapublishing.org/oe/abstract.cfm?uri=oe-21-8-10095.

[96] Alexander M Herman et al. "Cell type-specific and time-dependent light exposure contribute to silencing in neurons expressing Channelrhodopsin-2". In: *eLife* 3 (Jan. 2014). ISSN: 2050-084X. DOI: 10.7554/eLife.01481. URL: https://elifesciences.org/articles/01481.

[97] E. Deutsch et al. "Kv2.1 cell surface clusters are insertion platforms for ion channel delivery to the plasma membrane". In: *Molecular Biology of the Cell* 23.15 (2012), pp. 2917–2929. ISSN: 1059-1524. DOI: 10.1091/mbc.e12-01-0047.

[98] Scott F. Owen, Max H. Liu, and Anatol C. Kreitzer. "Thermal constraints on in vivo optogenetic manipulations". In: *Nature Neuroscience* 22.7 (July 2019), pp. 1061–1065. ISSN: 1097-6256. DOI: 10.1038/s41593-019-0422-3. URL: http://www.nature.com/articles/s41593-019-0422-3.

[99] Kaspar Podgorski and Gayathri Ranganathan. "Brain heating induced by near-infrared lasers during multiphoton microscopy". In: *Journal of Neurophysiology* 116.3 (Sept. 2016), pp. 1012–1023. DOI: 10.1152/jn.00275.2016. URL: http://www.physiology.org/doi/10.1152/jn.00275.2016.

[100] Yukiko Kimura et al. "Hindbrain V2a Neurons in the Excitation of Spinal Locomotor Circuits during Zebrafish Swimming". In: *Current Biology* 23.10 (May 2013), pp. 843–849. DOI: 10.1016/J.CUB.2013.03.066. URL: https://www.sciencedirect.com/science/article/pii/S0960982213003680.